The University Of Sheffield.

Phase Separation in Aerospace Polymer Blends

Emma Louise Wood

A thesis submitted in partial fulfilment of the requirements for the degree of Doctor of Philosophy

The University of Sheffield

Faculty of Science

Department of Physics and Astronomy

September 2019

Declaration of Authorship

I, Emma Wood, hereby certify that the work presented in this thesis, except where otherwise stated, is based on my own research, guided by my Ph.D. supervisor Nigel Clarke, and has not been submitted previously for a degree in any university or institution.

This copy has been supplied on the understanding that it is copyright material and that no quotation from the thesis may be published without proper acknowledgement.

Acknowledgements

I would like to take this opportunity to thank my supervisor, Professor Nigel Clarke, for his support and guidance throughout my PhD.

I would also like to thank the team at Solvay, especially those based at the Wilton Centre: Dominic Wadkin-Snaith, Claude Billaud, Mark Harriman, Paul Cross and Peter Mills. In addition to contributing financially to the project, they have provided training, materials, equipment, and intellectual input into both the theoretical and experimental sides of the research.

I would like to thank the Institut Laue-Langevin for the use of their facilities, and Isabelle Grillo in particular for acting as our local contact during the SANS experiment.

I would like to acknowledge the Engineering and Physical Sciences Research Council for funding this work through the Polymers, Soft Matter and Colloids Centre for Doctoral Training (CDT). As well as providing a supportive community for producing excellent science, the CDT has offered several opportunities for personal and professional development beyond those generally encountered during the PhD experience.

I would like to thank my parents for their financial and motivational support through the earlier years of my education that allowed me reach PhD level.

Last but certainly not least, I would like to thank my partner Calum for taking the time to explain synthetic polymer chemistry to a chemical physicist, for proofreading reports and conference abstracts, and for motivating me during this project.

Abstract

Polymer composites are becoming increasingly attractive to the aerospace industry as a lighter alternative to metal. They allow better fuel efficiency, so reduce environmental impact and operating costs. To create strong and fracture-resistant composites, blends of branched epoxy resin thermosets and linear thermoplastics are used. As the mechanical properties of these materials are largely determined by their morphologies, it is important to understand the phase separation that takes place within the blends.

Unfortunately, the usual techniques for studying phase separation, such as the Flory-Huggins model, are not particularly applicable to branched polymers, so predictions of the behaviour of such blends are limited. Even the lattice cluster theory can only be used for polymers with simple, regular architectures, rather than the randomly branched thermosets relevant to the aerospace industry.

In this work, a computational approach was developed to calculate the entropy and free energy of branched polymers with arbitrary shapes and sizes. Although these calculations are currently only valid for polymers in infinitely dilute solution, they provide systematic corrections to the Flory-Huggins predictions.

Concentration fluctuations, which are the precursor for phase separation, have also been studied directly using Monte Carlo simulations based on the bond fluctuation model. Properties such as total interaction energies, radii of gyration, radial distribution functions and structure factors have been determined for blends containing molecules with various amounts of branching, and various combinations of interaction energies.

Finally, a model experimental system based on an industrially-relevant blend has been designed and characterised. This allowed measurements of concentration fluctuations to be carried out using small-angle neutron scattering, and for the competing influences of temperature and cure extent on miscibility behaviour to be studied separately. In the future, it is hoped that the results from these experiments could be compared with structure factors produced using the simulation method mentioned above.

Abbreviations

a	Lattice spacing or segment size in the Flory-Huggins model
BFM	Bond Fluctuation Model
BMI	Bis-maleimide
CFRP	Carbon fibre reinforced polymer
c_i	Number of nearest neighbour contacts to segments of polymer type i on the Flory-Huggins lattice
c_{ij}	Number of nearest neighbour contacts between segments of polymer types i and j on the Flory-Huggins lattice
COM	Centre of mass
CPC	Cloud-point curve
D	Diffusion coefficient
DCDPS	4,4'-Dichlorodiphenyl sulfone
DDS	Diaminodiphenylsulfone
D_{eff}	Effective diffusion coefficient during spinodal decomposition
DGEBA	Bisphenol A diglycidyl ether
DMA	Dynamic mechanical analysis
DSC	Differential scanning calorimetry
e	Mathematical constant 2.718..., base of the natural logarithm
E	Energy
E^A	Lower bound for the energy of a polymer calculated using the hypothetical scanning method
E^B	Upper bound for the energy of a polymer calculated using the hypothetical scanning method

E^M	Mean energy of a polymer calculated using the hypothetical scanning method
E_i	Interaction energy for a specific polymer conformation i
E_{mix}	Energy of mixing
f	Functionality, number of bonds that can be formed from a segment
f	Number of future polymer segments scanned during hypothetical scanning calculations
f_i	Probability that a site on the Flory-Huggins lattice is occupied after i polymers have already been placed
F	Helmholtz free energy
F^A	Lower bound for the free energy of a polymer calculated using the hypothetical scanning method
F^B	Upper bound for the free energy of a polymer calculated using the hypothetical scanning method
F^M	Mean free energy of a polymer calculated using the hypothetical scanning method
F_{mix}	Free energy of mixing
G	Gibb's free energy
G_{IC}	Energy per unit area of crack surface at fracture initiation
GPC	Gel permeation chromatography
$g(r)$	Radial distribution function
$g_{EE}(r)$	Epoxy-epoxy radial distribution function
$g_{ET}(r)$	Epoxy-thermoplastic radial distribution function
$g_{TT}(r)$	Thermoplastic-thermoplastic radial distribution function
H	Enthalpy
HMDA	Hexamethylenediamine
$h(r)$	Pair correlation function, equal to $g(r) - 1$

$I(q)$	Scattering intensity
I_0	Scattering intensity at $q = 0$
IPDA	Isophorone diamine
j	Position of a segment within a polymer
J	Flux of material
K	Ratio between rates of phase separation and polymerisation
k_B	The Boltzmann constant
K_{IC}	Critical strength intensity factor
L	Side-length of a computational or theoretical lattice
LCST	Lower critical solution temperature
LCT	Lattice cluster theory
MDEA	Methylene bis(2,6-diethylaniline)
$m(n, s)$	Distribution law for molecular weights during polymerisation
M_n	Number average molar weight
M_w	Weight average molar weight
M_z	Z or centrifugal average molar weight
n	Number of amine curative monomers in a cluster during polymerisation
n	Number of sites or segments on the Flory-Huggins lattice
n_i	Number of molecules of type i on the Flory-Huggins lattice
N	Number of bonds in a polymer
N_i	Number of segments in a single polymer of type i on the Flory-Huggins lattice
NMR	Nuclear magnetic resonance spectroscopy
p	Pressure
p	Conversion of thermoset, i.e. fraction of possible bonds formed
PBCs	Periodic boundary conditions

p_c	Percolation threshold, i.e. critical value of conversion at gelation
p_i	Probablity of microstate i occurring
P_i^B	True probability of finding a polymer in conformation i within a Boltzmann distributed ensemble
$P_i(f)$	Estimated probability of finding a polymer in conformation i within a simulated ensemble using the hypothetical scanning method
$P_j(f)$	Probability of placing a polymer segment in its correct position during a hypothetical scanning simulation
PAEK	(polyaryl ether ketone)
PES	Poly(ether sulfone)
PEES	Poly(ether ether sulfone)
PMMA	poly(methyl methacrylate)
$\boldsymbol{q}$	Wavevector of radiation used for scattering
q	Wavenumber of radiation used for scattering, magnitude of wavevector
r	Stoichiometric ratio of reactive groups in an epoxy resin system
r	Radius or distance from a specified point
r_c	Critical droplet radius in nucleation and growth
RDF	Radial distribution function
R_g	Radius of gyration
RIPS	Reaction-induced phase separation
RPA	Random phase approximation
s	Number of epoxy monomers in a cluster during polymerisation
S	Entropy
S^A	Upper bound for the entropy of a polymer calculated using the hypothetical scanning method
S^B	Lower bound for the entropy of a polymer calculated using the hypothetical scanning method

S^M	Mean entropy of a polymer calculated using the hypothetical scanning method
SANS	Small angle neutron scattering
S_{mix}	Entropy of mixing
SAW	Self-avoiding walk
SAT	Self avoiding tree
SCFT	Self-consistent field theory
$S(q)$	Structure factor
T	Temperature
T_g	Glass transition temperature
TGAP	Triglycidyl-p-aminophenol
TGDDM	Tetraglycidyl 4,4-diaminodiphenyl-methane
THF	Tetrahydrofuran
TMA	Thermal mechanical analysis
TPE	Thermoplastic elastomer
UCST	Upper critical solution temperature
V	Volume
$V(q)$	Fourier transform of energetic interactions in the RPA
vol.%	Volume percent
WLF	Williams-Landal-Ferry, an empirical equation describing time-temperature superposition
wt.%	Weight percent
$\mathbf{x}$	Position
z	Coordination number, number of nearest neighbours
Z	Partition function
z_{eff}	Effective coordination number
ϵ	Nearest neighbour interaction energy between two segments

ϵ_{EE}	Epoxy-epoxy nearest neighbour interaction energy
ϵ_{ET}	Epoxy-thermoplastic nearest neighbour interaction energy
ϵ_{TT}	Thermoplastic-thermoplastic nearest neighbour interaction energy
ϵ_{PP}	Polymer-polymer nearest neighbour interaction energy
ϵ_{PS}	Polymer-solvent nearest neighbour interaction energy
κ	Gradient energy coefficient in Cahn-Hilliard equation
λ	Wavelength
μ	Chemical potential
μ	Viscosity
ν_i	Number of possible arrangements of polymer i on the Flory-Huggins lattice
ξ	Persistence length of polymer
ρ	Average density, overall or of a particular species
$\rho(r)$	Local density, overall or of a particular species
ϕ	Description of blend composition via volume fraction of one species
ϕ_0	Average blend composition in a system, i.e. composition of mixed state
ϕ_i	Volume fraction of component i
χ	Interaction parameter between polymers in a blend
χ_c	Critical interaction parameter for phase separation
Ω	Number of microstates in macrostate
Ω_M	Number of microstates in mixed state of blend

Contents

Chapter 1

Introduction

In recent years, there has been a driving trend to replace traditional aluminium-based aircraft components with carbon-fibre reinforced polymer composites (CFRPs). There are several advantages of doing this. Firstly and most importantly, polymers offer a 20–40 % weight saving compared to metals.[1,2] This allows greater fuel efficiency, which reduces operating costs and environmental impact. Reducing the aircraft weight has a domino effect on the amount of fuel required, so that each kilogram of fuselage weight saved can result in a fourfold reduction in take-off weight.[1,3]. It has been estimated that a 1 kg reduction aircraft in weight can save over 2900 L of fuel per year.[2] The manufacture of polymer-based components is becoming more cost effective,[4] and techniques such as injection moulding allow greater design flexibility.[2]

Extensive research is being done into self-healing resins, which polymerise healing agents into cracks to close them up, reducing maintenance requirements.[5] Another advantage of CFRPs is the naturally corrosion resistant nature of polymers,[2] which allows a greater humidity in the aircraft cabin, making for a more pleasant passenger experience. Polymers also fatigue less than metals under repeated applied loads,[2] meaning that fewer cracks are formed and less structural

weakness is introduced. Consequently, the cabins do not have to be kept as highly pressurised as in traditional aircraft, again improving passenger comfort.

Aerospace composites consist of continuous straight fibres embedded in a host matrix containing of a blend of different types of polymers. The aim is to combine the characteristics of the different materials together to produce improved mechanical properties. Rudimentary composite technology based on glass fibres has been around since the 1940s, first in the military and later in commercial aircraft.[1] Initially, composites were employed only in radomes and bullet-proofing of fuel tanks,[1] but by the early 1970s, after the discovery of carbon fibre in 1964,[2] their usage had progressed to flaps, tails, floor panels and wing fairings.[1] By the 1990s, 15–20 % of the structural weight of commercial aircraft consisted of composites.[1] In the last decade, the more advanced Boeing 787 Dreamliner and Airbus A350 XWB have come into service. These famously contain 50 wt.% of structural composite in their fuselages and wings,[6] equivalent to over 80 % by volume. Engine areas and leading edges of wings are still composed of aluminium alloy due to its ability to withstand high levels of heat and bird strikes.[7] A pictorial showing the material construction of a Boeing 787 Dreamliner is given in Figure 1.1.[8]

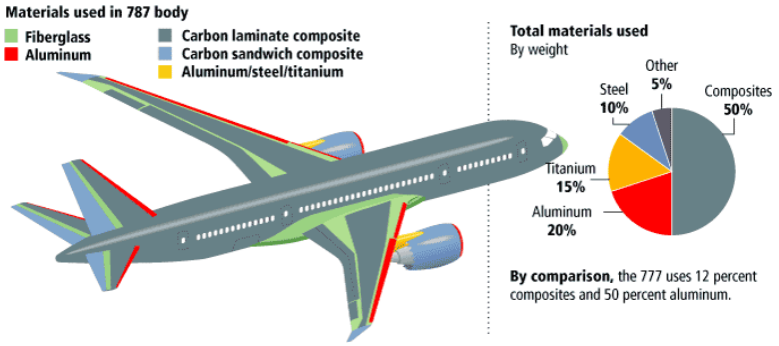

Figure 1.1: A schematic showing the construction materials for each area of a Boeing 787 Dreamliner aircraft. Reproduced from Tanasa et al.*[8]*

Although great progress has been made, the behaviour of aerospace compos-

ites is still poorly understood, both in terms of predicting structural morphologies from the thermodynamics and kinetics of the starting chemistries, and of predicting mechanical properties from known morphologies. In fact, the Boeing 787 uses essentially the same composite for all aircraft parts, with no optimisation for specific purpose.[9] There is therefore a large scope for research towards a fuller understanding of CFRPs, with the aim of developing composites with improved mechanical and thermal properties that are easier to process, maintain and recycle.

This thesis will be focused on developing our understanding of the impact of thermodynamics on the morphology of aerospace composites. The introductory chapter will be divided into five sections. The first will discuss the types of polymers that are used in aerospace materials, and why controlled phase separation is important to give optimal mechanical properties. The second will describe the theory of phase separation in polymer blends, both in general and in the specific case of aerospace composites. The third section will then look at some kinetic behaviours of the type of composites used in aerospace that complicate our understanding of phase separation. The fourth section will discuss Monte Carlo modelling, a computational simulation technique that will be used in the first two results chapters. The fifth and final section of this chapter will be a brief overview of the thesis, discussing the aims and some of the methodology.

1.1 Polymers

1.1.1 Types of polymers

Polymers are macromolecules which consist of repeating monomer units. They are usually hydrocarbons and have molecular weights ranging from thousands to

millions of atomic mass units. There are two main classes with distinct molecular architectures: thermoplastics and thermosets, each of which contain many different types of chemistries.[10,11]

1.1.1.1 Thermoplastics

The thermoplastic polymer class covers most everyday plastics, such as packaging, clothing, toys, glass substitutes, signs, building materials, and components in paints and lubricants.[11]

Thermoplastics are composed of linear polymer chains which are physically entangled together, as shown in Figure 1.2a. Depending on temperature, there is a movement of chains through these entanglements that allows the materials to retain some flexibility in their structures.[12] This gives a desirable feature of impact resistance, but also causes some structural weakness, characterised by a moderate value of the elastic modulus. The elastic modulus measures the ability of a material to resist non-permanent elastic deformation (i.e. to hold its shape) when a stress is applied.[13] Therefore, if a thermoplastic is hit by an external force, it will tend to change in shape but not fracture.

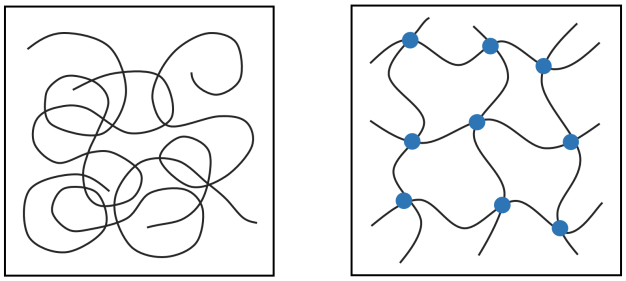

(a) Thermoplastic *(b) Thermoset*

Figure 1.2: Schematic of the arrangement of chains in thermoplastic and thermosetting polymers.

Thermoplastics melt to a liquid when exposed to high enough temperatures.[11]

This can be beneficial, as it allows them to be reshaped and recycled, but means they cannot generally be used for high temperature applications.

Recently, high performance thermoplastics such as the PAEK (polyaryl ether ketone) family have been developed. These are semi-crystalline polymers with unusually high mechanical strengths and temperature stabilities.[14] They exhibit melting points of between 340 °C and 390 °C,[15] and can withstand constant operating temperatures of up to 250 °C and short term exposure to 350 °C.[14] This allows them to be used for non-structural applications within the aerospace industry such as ducts, pipes and clamps, but the technology has not yet progressed to the stage where they are strong enough to be used for construction of the main fuselage.[16]

1.1.1.2 Thermosets

Thermosetting polymers tend to be used for more specialised purposes than thermoplastics. Bakelite is well known as the first thermoset polymer to be invented in the early 1900s.[17] Due to its heat resistance, it was widely used in electrical equipment, for handles of cookware, and in weapons manufacture during World War II. Thermosets are still used as electrical components, and now also see purposes in adhesives, construction equipment, furniture, sports products, the energy sector, and of course, in automotive and aerospace materials.[18]

In terms of molecular structure, thermosetting polymers are similar to thermoplastics, with the addition of irreversible covalently-bonded chemical cross-links between the chains, as shown in Figure 1.2b. These cross-links are branching points that fix the structure of thermosets into 3D networks. A high degree of cross-linking makes a thermoset extremely structurally strong, which can be characterised by a high elastic modulus.[18]

The covalent bonds in the cross-links between the chains are as strong as those within the chains. This prevents the polymer network from breaking into its constituent strands, making thermosets insoluble in any choice of solvent. It also means they cannot be melted, as their melting temperatures are raised higher than their degradation temperatures.[11,18] Structurally, this is very beneficial, as it allows the materials to retain their strength at increased temperatures, but it also makes them extremely difficult to recycle.

When thermosets are exposed to very high temperatures of several hundred degrees Celsius, there is enough thermal energy to overcome the bond dissociation energies, both of the cross-linking and intra-chain covalent bonds. The chemical bonds tying the polymer networks together are broken, and the thermosets decompose into elemental or small molecular constituents. If temperatures are only high enough to permit partial degradation, thermoset materials can appear intact but lose a large proportion of their strength.[19]

In a thermosetting polymer, the rigidity of the 3D network is highly desirable for structural strength, but also causes brittleness. In fact, one of the major challenges in aerospace engineering is the difficulty of increasing the fracture toughness (i.e. decreasing the brittleness) of the materials without compromising their moduli (strength).[18] Methods to mitigate this problem will be discussed in detail in the Section 1.1.3.1.

Thermosetting polymers are generally produced from monomers or oligomers (small chains) of linear polymer. These are heated to induce polymerisation chemical reactions, which form the cross-links between the chains that give the characteristic network structure.[18]

1.1.2 States of polymers

Even an unblended material containing only one type of polymer molecule can be found in several different states, depending on chemical composition and temperature.

1.1.2.1 Semi-crystalline polymers

Most thermoplastics, particularly those with regular repeating chemistries in their backbones, are susceptible to chain alignment, which gives a spatially ordered crystalline structure. Due to the long length of entangled polymer chains, it is difficult for them to align along the full backbone, even when folded. Instead, thermoplastic polymers tend to be semi-crystalline in nature, with a degree of crystallinity typically ranging from 10-80 %.[20,21] Small crystallites of ordered lamellae are separated by disordered, amorphous (non-crystalline) regions, as shown in Figure 1.3.[22]

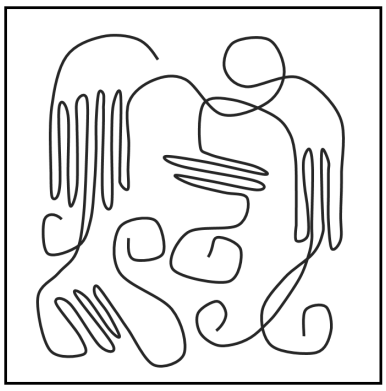

Figure 1.3: A schematic showing the orientation of polymer chains in a semi-crystalline polymer. Small crystallites of ordered lamellae are interspersed with disordered amorphous regions.

Crystalline behaviour can only occur below the melt temperature, where there is a favourable free energy for crystallisation. Here, the additional entropy aris-

ing from disordered chains becomes less important than the reduced interaction energy from optimally organising the polymers. Melt temperatures vary considerably, but are usually above room temperature.[20]

Crystallites tend to enhance the rigidity and strength of thermoplastics, at the cost of increased brittleness.[23] They also affect the chemical resistance of the polymers. Solubility is reduced as it is hard for solvent to penetrate through crystalline regions, and the binding force in the crystal provides an energy barrier for dissolution.[24]

Semi-crystalline polymers are opaque, due to the scattering of light from many boundaries between various crystallites and non-crystalline regions in the material.[25]

1.1.2.2 Polymer melts

A polymer melt occurs when a semi-crystalline polymer is raised above its melt temperature. The crystalline order is broken, and the polymer becomes liquid. A common analogy to aid visualisation is to imagine the polymer chains as strands of spaghetti; the individual chains are structurally distinct from one another, but are entangled together.[25] In a melt, polymer chains generally move smoothly past each other except at these entanglement points. Various theoretical models have described entanglements as temporary cross-links,[26,27] as tubes surrounding the polymer chains to confine motion,[28,29] or by introducing an effective friction at entanglement points.[30]

In thermosetting polymers, the strong cross-links binding the network together prevent the polymer chains from flowing past each other, so thermosets cannot be found in the melt state.

1.1.2.3 Glasses

Polymer glasses are amorphous (non-crystalline) polymeric solids. Similarly to liquids, they exhibit no long-range order, but do possess short-range atomic-scale order due to the chemical bonds holding the polymer segments together.[20]

On cooling a polymer from a melt state, the amount of heat energy in the system decreases, and restricts the kinetic energy available to the molecules. This reduces the mobility, so that the molecular positions are fixed and the polymer transitions from a melt to a glass.[22] This glass transition will be discussed in more detail in Section 1.3.2, but it is important to note that it is not a true phase transition, so glasses do not exhibit a melting point.

Polymer glasses are either transparent or translucent.[25] They are very strong, although less so than equivalent crystalline polymers.[20,23] They are also brittle, as their irregular structures mean there are no planes of atoms that can slip past each other to reduce stress.[31] Glasses tend to possess relatively low temperature resistances, and soften as the temperature increases.

Almost any substance can be forced into an glassy form, if it is cooled rapidly enough from a liquid that the constituent molecules are not able to reach their equilibrium crystalline form before mobility is arrested due to lack of kinetic energy.[20] However, some materials are inherently unable to form a crystalline state and therefore exhibit an intrinsically glassy solid form. Thermosetting polymers are prime candidates for this behaviour, as the random network arrangement of the covalent cross-links prevents the substance from aligning into a crystal.[32]

As mentioned in Section 1.1.1.2, a thermosetting polymer is formed by cross-linking short-chain oligomers. This initially takes place in the melt state, where the linear structure of the oligomers allows flow. When cross-links begin to form into a loose network, this flow is restricted, and the material becomes rubbery

in behaviour (see Section 1.1.2.4). As more cross-links form and the network becomes more tightly bound and rigid, the material becomes glassy. The thermoset is then unable to ever return to its melt state due to the strength of the covalently bonded cross-links binding its structure into place.

1.1.2.4 Elastomers / rubbers

Elastomers, also known as rubbers, are technically a subset of both the thermoplastic and thermosetting polymer classes. They are simply amorphous polymers maintained above their glass transition temperature.[20]

However, due to their vastly different mechanical properties to other polymer states, elastomers are often regarded as being a class of their own. The term elastomer is a contraction of the words 'elastic' and 'polymer', which gives a good indication of their behaviour. Due to weak intermolecular bonds, elastomers exhibit low elastic moduli, meaning they lack stiffness and can easily be deformed.[20,33] However, they spring back to their original shapes once the external stress is removed.[34] Their extremely high flexibilities naturally lead to high fracture resistances.

Traditional elastomers are formed from thermosets.[20] If a polymer melt can be visualised as spaghetti, elastomers can be similarly described as strands of spaghetti where some sections have clumped and stuck together. The spaghetti strands are the polymer chains, and these clumps are the cross-links that prevent the chains from long-distance flow. The sections of 'spaghetti' chain between the 'clump' cross-links maintain some level of mobility, which allows the material to deform by stretching out the polymer chains when an external stress is applied. On removal of this stress, the presence of cross-links and requirement to maximise entropy causes the elastomer to spring back to its original equilibrium shape.[20,34]

A thermoset that is elastomeric at room temperature will tend to have fewer cross-links than one in its glassy form, as longer stretches of chain between the cross-links enable the small-scale mobility that is necessary for a rubber. However, nearly all thermosetting polymer glasses exhibit elastomeric behaviour when raised above their glass transition temperatures.[20]

Thermoplastic elastomers (TPEs) also exist. These are similar to thermoset elastomers, but instead of the cross-links being chemically bonded, they are instead formed from physical, non-covalent interactions such as ionic or hydrogen bonds.[35,36] As these weaker bonds can be broken by thermal energy, TPEs can be repeatedly heated into a liquid state (i.e. a polymer melt) and cooled back to a rubber. They are also soluble in certain solvents. These characteristics allow them to be reused and recycled.[37] TPEs offer a wide range of properties that can be tuned to suit their purpose.

1.1.3 Aerospace composites

Aerospace composite materials are subject to, and must withstand, extreme operating conditions. There is commonly a pressure difference of approximately 60 kPa between the inside and outside of the aircraft cabin,[38] which the structural material must be strong enough to withstand without deformation. A combination of high speeds and air turbulence, as well as the impact of bird strikes, means that sudden forces are frequently applied, so the composite must be fracture-resistant. The aircraft material is also exposed to a large range of temperatures. Ground temperatures of up to 50 °C are common, and cabins are kept around 20 °C. Commercial aircraft fly at an altitude of approximately 11 km, where ambient air temperature drops to −55 °C,[39] but friction causes the leading edges to equilibrate at −25 °C. Engine areas of the aircraft experience extremely high temperatures of hundreds of degrees, and have to be made out of metal, as

current composites are unable to maintain their structural integrity and provide adequate fire resistance in these conditions.[7]

Aerospace composites are made from carbon fibre reinforced polymer, or CFRP. Much of the strength and rigidity of these composites comes from the reinforcing carbon fibres, but these are surrounded and bound together by a polymer resin matrix, which must also exhibit excellent mechanical properties.[2] This thesis will focus solely on the matrix component of the CFRP composite, although it must be noted that combining the polymer resin with the carbon fibres also leads to unique challenges, such as ensuring adequate adhesion at the interface, and managing the effect of disrupting the matrix structure with fibres on the mechanical properties[2]

The bulk, typically 70 wt.%, of the polymer matrix is composed of a thermosetting polymer resin network. This provides the structural strength and stiffness necessary to hold the composite in shape, even when exposed to the extreme environments detailed above. The thermoset must be maintained well below its glass transition temperature so that it can benefit from the strength of the glassy state without becoming rubbery.[18]

Unfortunately, as mentioned in Section 1.1.2.3, thermosetting polymer networks in the glassy state suffer from brittleness, so provide little protection against cracks caused by vibrations from engines, air turbulence or bird strikes. This low fracture resistance is characterised by low values of K_{IC}, the critical strength intensity factor, which is the lowest stress that will propagate a crack, and G_{IC}, the critical elastic energy release rate, which describes the energy per unit area of crack surface at fracture initiation.[40]

1.1.3.1 Toughening of thermoset matrices

Various attempts at improving the fracture toughness of thermosets have been made. The most straightforward is to simply cure the polymer at a higher temperature, once the material has undergone thermal expansion. This loosens the network, giving greater flexibility and reducing brittleness, but has limited scope.[41]

Another traditional method of toughening is to add regions of rubbery elastomer into the thermoset network. This prevents crack propagation by deforming the matrix in the vicinity of the crack tip via a method known as localised cavitation, and therefore allowing the impact energy to dissipate.[41] This works effectively in many cases, but has the disadvantage that the elasticity of the rubber greatly reduces the modulus of the material, so that it is structurally weakened. Also, if the thermoset matrix is highly cross-linked, its ability to deform reduces significantly and the main mechanism of crack prevention is lost.[41,42] These shortcomings make rubber-toughening unsuitable for use in aerospace composites.

Instead the aerospace industry has turned to using high-performance ductile thermoplastics as toughening additives[41,42], usually in quantities of about 30 wt.%. Thermoplastic modifiers do not rely on distorting the thermoset network to aid fracture resistance, but instead dissipate energy via other mechanisms which are less prevalent in rubber modifiers.[41] The effect varies with the structural morphology of the material. Some thermoplastic chains are usually dispersed homogeneously through the thermoset matrix, which loosens the network and changes its intrinsic properties.[41] However, as this mechanism doesn't affect the fracture mechanism, it has limited effect: Bucknall and Partridge found that for a system with homogeneous morphology, K_{IC} was barely increased.[43]

More significant improvements are apparent in inhomogeneous blends of thermosets and thermoplastics.[41,42] Bucknall and Gilbert found that introducing a

thermoplastic modifier to a thermoset, so that an inhomogeneous morphology was formed, caused an increase in both K_{IC} and G_{IC}, with minimal reduction in elastic modulus.[42] An addition of 16.6 vol.% thermoplastic modifier increased G_{IC} by a factor of 8 compared to the unmodified resin. Incidentally, this is far superior to the doubling of G_{IC} observed when adding rubber modifiers.[42]

The creation of such an inhomogeneous morphology takes place when phase separation (see Section 1.2) occurs to give distinct regions with different molecular compositions. In phase separated systems, regions rich in thermoplastic prevent the propagation of cracks using methods such as crack tip blunting or bridging[41]. Crack tip blunting occurs when plastic deformation in a thermoplastic-rich region widens a crack, reducing the stress intensity at the tip and making it harder for the crack to propagate. Crack bridging takes place when a material is not fully cleaved along a crack, leaving some ligaments connecting the two faces together; this reduces the pressure pushing the two faces apart, lowering the driving force for crack propagation.

The effectiveness of these toughening processes greatly depends on the sizes and compositions of the different regions in the material, so the mechanical properties of a thermoset/thermoplastic blend are strongly affected by miscibility and phase separation.[41,42] Therefore, in order to improve the performance of aerospace composites, it is vitally important to understand the process of phase separation within the material.

1.1.4 Chemistry of aerospace composites

Various types of thermosetting polymers have been considered for the network component of the aerospace composite matrix. They have different chemistries, each with benefits and drawbacks, but all are formed via a chemical cross-linking reaction known as curing.

1.1.4.1 Curing

Curing describes the polymerisation chemical reaction that joins monomers or short chain oligomers together and cross-links them into a thermoset network. In some cases, the thermoset monomers can react directly with each other, but often a curative or hardener is used as a co-reactant to aid the process. Curatives are usually multifunctional amine molecules, which contain two or more primary amine groups (a nitrogen attached to two hydrogens).[44]

Depending on the chemistries involved, curing can sometimes be undertaken at room temperature, but generally application of heat is required to drive the reaction. This can either be at a constant raised temperature (an isothermal cure), or under temperature ramping conditions. Most commonly, there is an initial increasing temperature ramp, followed by an isothermal cure for several hours at 150-180 °C and then a decreasing ramp to room temperature.[45,46]

The ramp before reaching peak temperature is beneficial for several reasons. The most important is safety. The type of polymerisation reactions used in the curing process are exothermic, meaning that they give out heat energy. If the reaction proceeds too fast, a huge amount of heat energy can be released at once, causing a fire or explosion.[47] By curing at initially low temperatures, the reaction can proceed in a more controlled manner. The temperature can then be safely raised to ensure full reaction once the majority of the available reactants have been used up.

The second reason for using an initial temperature ramp, rather than jumping straight to an isothermal high temperature cure, is to improve control over the morphology of the material. In Section 1.1.3.1, we saw that the presence of phase separated regions with different compositions greatly affects mechanical properties such as strength and toughness. The sizes of these regions are influenced by cure temperature. When curing at a high temperature, cross-links connect the

network very quickly, so there is little time for the component molecules to migrate through the material into their separated regions before they become fixed in place, and the resultant regions are very small. Conversely, curing at a low temperature allows for a long migration time, so that the regions can become very large.[41] For good mechanical properties, micrometre-scale regions are required, and this is most easily achieved by using a temperature ramp.

A third reason for not immediately curing at high temperature is to avoid causing residual stresses in the material due to a mismatch of expansion between the epoxy resin matrix and carbon fibres. The epoxy resin component can shrink by up to 6 vol.% during cross-linking, so it is beneficial to cure at lower temperature. This reduces the thermal expansion of the carbon fibre, and slows the cure rate to avoid shocking the system. For this reason, an isothermal dwell or soak is sometimes carried out at 120-140 °C for approximately an hour during the increasing temperature ramp. This first dwell can be also used to allow the material to flow and let volatiles escape the matrix, but has now mainly been replaced by a steady temperature ramp.[45,46,48]

After the main cure cycle is completed, thermoset resins are usually subject to a high temperature isothermal postcure. This increases the cross-linking density by ensuring as much of the thermoset reacts as possible, and therefore improves material properties such as rigidy, strength and chemical resistance.[46]

1.1.4.2 Benzoxazine resins

Benzoxazine resins are a type of thermosetting polymer that are of much interest with regards to their viability for aerospace materials.

Benzoxazine monomers are formed by chemical reactions between phenols, formaldehyde and primary aromatic amines, a generic example of which is shown

in Figure 1.4. The resultant monomer contains a characteristic oxazine group, which is a doubly unsaturated six-membered heterocyclic ring composed of four carbon atoms along with one nitrogen and one oxygen.[49]

Curing is then carried out by applying heat to the benzoxazine monomers to cross-link them via a thermal ring-opening polymerisation. Figure 1.4 shows this reaction and the general structure of the resulting benzoxazine resin, but the chemistry can be altered by changing the side groups on the initial phenol and amine molecules.[49]

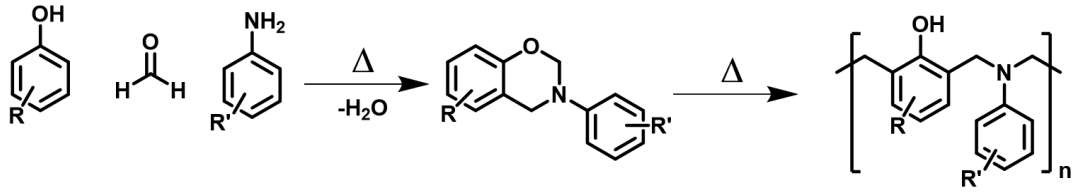

Figure 1.4: The reaction scheme of a phenol, formaldehyde and primary aromatic amine to give a benzoxazine monomer, and the following polymerisation reaction to give benzoxazine resin.

Benzoxazines typically perform well in increased temperature conditions due to high glass transition and decomposition temperatures. They are also extremely strong and have other beneficial properties, including flame retardancy and chemical resistance. However, they require very high cure temperatures of over 200 °C, making production of large quantities undesirable, and are extremely brittle. This low fracture toughness means they are currently unsuitable for structural purposes, but are ideal for use inside the aircraft cabin as overhead lockers and window frames.[49]

1.1.4.3 Bismaleimide resins

An alternative thermoset material is bismaleimide (BMI) resin. These materials are formed by a condensation curing reaction between maleic anhydride and a diamine curative (see Figure 1.5) at a maximum ramp temperature of 180 °C, followed by a postcure at 230 °C.[45]

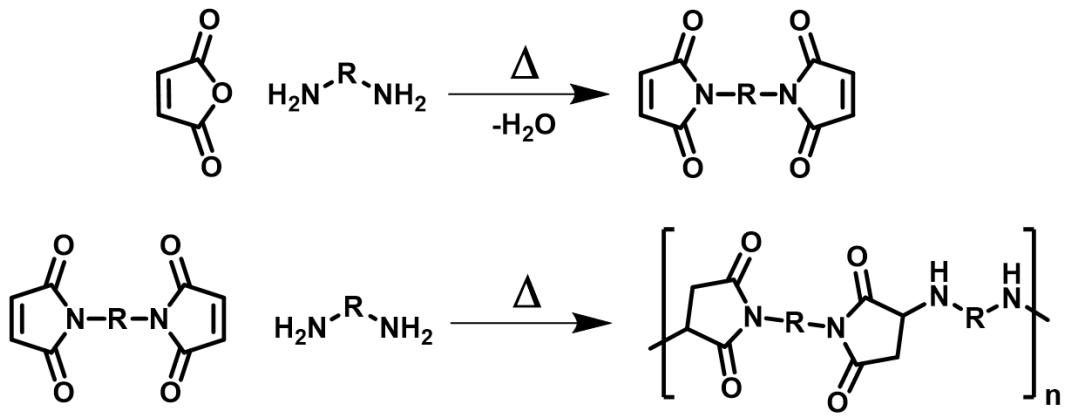

Figure 1.5: The reaction scheme for a bismaleimide resin. First maleic anhydride is reacted with diamine curative to give bismaleimide monomer, then this is reacted again with diamine curative to produce bismaleimide resin.

BMIs are high-end thermosets that offer extremely high strength, as well as both temperature and chemical resistance. They offer operation temperatures of up to 180 °C, which is beyond the capabilities of most aerospace resins.[50] However, they are difficult to toughen and have a particularly long cure cycle of approximately 6 h, compared to the industry standard of 2-3 h.[51] These features mean that BMIs tend to only be used in military jet fighters and engine parts, and not for structural components of regular commercial aircraft.[52]

1.1.4.4 Epoxy resins

Epoxy resins are by far the most widely used type of thermoset in aerospace materials,[50] and are therefore the one the work in this thesis will focus on. They are strong, and have the benefit of being easier to toughen than other types of thermoset.

Epoxy resins are made from epoxy monomers or oligomers. These molecules have at least two epoxide functional end groups, which are three-membered heterocyclic rings containing one oxygen atom attached to two adjacent carbon atoms (see Figure 1.6a). A basic example of an epoxy monomer that will be used during this thesis is bisphenol A diglycidyl ether (DGEBA), the chemical structure of which is shown in Figure 1.6b.[11]

(a) Epoxide group

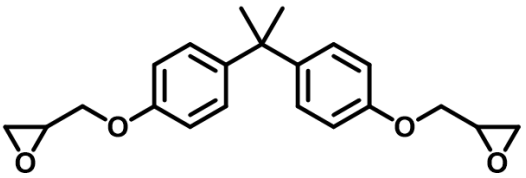

(b) DGEBA

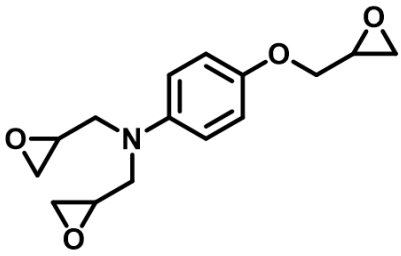

(c) TGAP

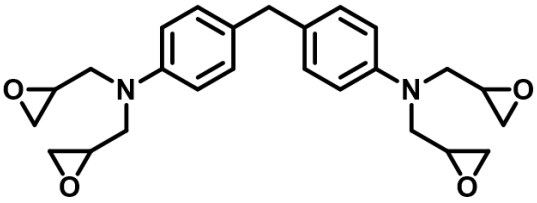

(d) TGDDM

Figure 1.6: Chemical structures of (a) an epoxide group and commonly used epoxy monomers: (b) DGEBA, (c) TGAP and (d) TGDDM.

Epoxide groups can self-react with each other, but tend not to until tempera-

tures of approximately 300 °C. Instead, they are generally reacted with multifunctional amine curatives to bring about polymerisation and cross-linking.[11] The cure cycle generally used for aerospace epoxy resins involves an increasing temperature ramp, followed by an isothermal cure at 150–180 °C for 2–3 h, a decreasing ramp to room temperature and then finally a postcure at above 200 °C.[51]

The ring-opening reaction scheme of a epoxide group with an amine group is shown in Figure 1.7a.[11] Both hydrogens of the primary amine group are able to react with a separate epoxy, but the second hydrogen often has a lower rate of reaction due to steric hindrance.[53] Therefore, most of the primary amines in the system may react before any of the secondary ones, which can give initially linear polymers.[54]

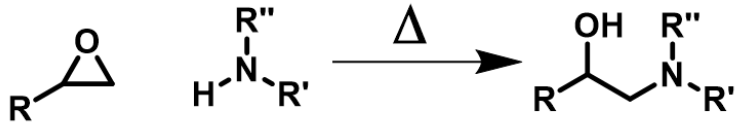

(a) Epoxide–amine reaction

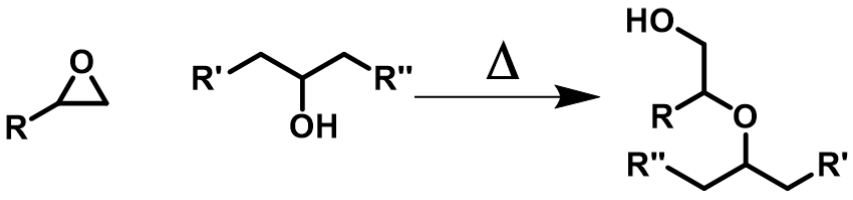

(b) Etherification

Figure 1.7: Reaction schemes for (a) an epoxide group with an amine group, and (b) an epoxide group with a hydroxyl group, also known as etherification.

Some epoxy resins monomers, such as DGEBA, are difunctional, meaning that they contain two epoxide functional groups, so all cross-links are due to the functionality of the curative. Others have higher functionality, allowing for a more tightly bound network.[50] In aerospace, a combination of trifunc-

tional triglycidyl-p-aminophenol (TGAP) and tetrafuctional tetraglycidyl 4,4-diaminodiphenyl-methane (TGDDM) molecules is common.[55,56] Molecular structures for these are shown in Figures 1.6cand 1.6d.

In addition to the desired epoxide-amine reaction, a secondary unwanted side reaction called etherification can sometimes also take place. Here, an epoxide group reacts with a hydroxyl (OH) group formed from a previous epoxide-amine reaction, as shown in Figure 1.7b.[57] This uses up some of the epoxide groups in the material, so weakens the cross-linking and leaves leftover unreacted amines, which can be toxic.[44] The chemical stoichiometry of such systems is often altered to ensure that no unreacted amines remain.

1.1.4.5 Amine curatives

A range of amine curatives can be reacted with epoxies and other thermosets, all with different characteristics that affect the final properties of the resin.[58] Diamines with primary two amine groups per molecule, each containing two hydrogen atoms, are generally used.[59] This means four branches can form from each curative molecule, allowing for an extensively branched network to be formed.

Aliphatic amines, which consist of a hydrocarbon chain between two amine end groups, allow fast curing and can often harden resins at room temperature.[60] An example of an aliphatic amine is hexamethylenediamine, which is shown in Figure 1.8a. Aliphatic amines such as hexamethylenediamine are used in the automotive industry, but due to relatively low temperature resistance,[60] they are not found in aerospace resins.

Benzene rings are six-membered carbon rings where each carbon is attached to one hydrogen atom or hydrocarbon side-chain; the remaining carbon electrons become delocalised above and below the ring, providing a stabilising resonance

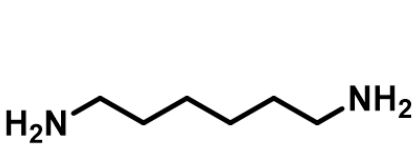

(a) Hexamethylenediamine

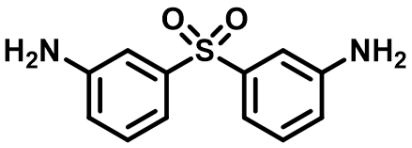

(b) 3,3'-DDS

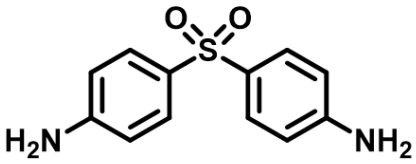

(c) 4,4'-DDS

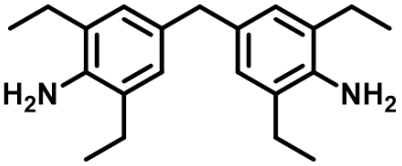

(d) MDEA

Figure 1.8: Chemical structures of commonly used diamine curatives: (a) hexamthylenediamine (b) 3,3'-DDS, (c) 4,4'-DDS and (d) MDEA.

structure. Aromatic amines, which contain at least one of these benzene rings, are much more suited to the high temperature applications of the aerospace industry, and also offer greater chemical resistance than their aliphatic relatives.[60] The high temperature stability is caused by an increase in the glass transition temperature due to the rigidity of the benzene rings.[61] Two aromatic amines commonly used in aerospace are 3,3'-diaminodiphenylsulfone (3,3'-DDS) and 4,4'-diaminodiphenylsulfone (4,4'-DDS), shown in Figures 1.8b and 1.8c.[55,56] These have very similar structures, both possessing two benzene rings, each of which is connected to a separate primary amine and a shared central sulfonyl (SO_2) group, differing only in the positions of the amines. However, even such a small change in molecular architecture can lead to vastly different performance. 3,3'-DDS reacts much more quickly with epoxy than 4,4'-DDS, and different amounts of phase separation are observed for each.[62] The presence of sulfur in amine curatives is desirable to improve the fire retardancy of epoxy resins, especially in combination with phosphorus,[63] but other aromatic amines are sometimes used, such as methylene bis(2,6-diethylaniline) or MDEA, shown in Figure 1.8d.[58]

1.1.4.6 PES/PEES thermoplastic tougheners

The type of thermoplastic used as a toughening agent will affect the properties of an epoxy resin matrix. Not only will the intrinsic characteristics of the thermoplastic directly influence the mechanical properties, but the chemistry will also affect the solubility and therefore the amount of phase separation.

A combination of poly(ether sulfones), PES, and poly(ether ether sulfones), PEES, are usually used, often with a mixture of both monomers in the same chain.[58,64] The chemical structures for these polysulfones are shown in Figure 1.9. PEES groups are more flexible than PES, so introducing them into the structure desirably reduces the viscosity of the material without compromising thermal stability.[64]

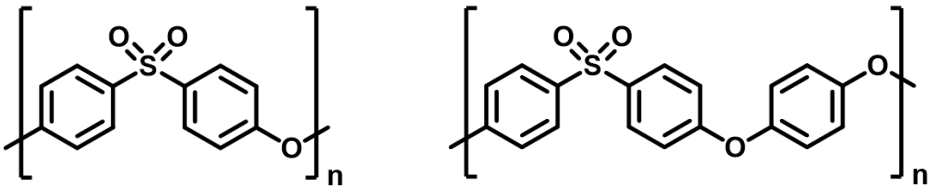

(a) PES *(b) PEES*

Figure 1.9: Chemical structure of (a) poly(ether sulfone), PES, and (b) poly(ether ether sulfone), PEES.

PES polymers are high performance thermoplastics which offer excellent mechanical properties and toughness over a wide range of temperatures from −50 °C to 180 °C, and have good thermal stability with glass transition temperatures of around 200 °C.[65] They also dissolve well into unreacted epoxy monomer/oligomers, allowing control over phase separation during the curing process.

The end groups of thermoplastic tougheners can be tuned to give optimal morphologies. In many cases, they have amine end groups, which react into the epoxy network in the same way as the curative to prevent too much phase

separation.[66] They can also be capped with hydroxyl groups, so that the reaction only happens partway through the cure at about 150 °C, or chlorine-ended so that no reaction takes place.

1.1.4.7 Thermoplastic composites

Although toughened thermoset matrices currently provide the best option for aerospace, there is interest in extending the use of high performance thermoplastic composites to structural purposes. These materials consist of carbon fibres which are bound together with thermoplastic resin, but contain no thermoset. The aim of this transition to thermoplastics is to provide better recyclability, and faster and easier processing, without the hurdle of the extremely high viscosities experienced when curing thermosets.[16,67]

As mentioned in Section 1.1.1.1, high performance thermoplastics such as PAEK are already used for non-structural or semi-structural purposes such as interiors, clips and brackets. However, the industry is now beginning to consider them for primary structural components like wing boxes and fuselage panels. However, they currently require extremely high processing temperatures of around 600 °C, and do not yet offer a cost-effective or mechanically sound solution.[16]

1.2 The Flory-Huggins model for phase separation in polymer blends

In the previous sections, we discussed the types of polymers used in the aerospace industry, along with their properties and characteristics. In Section 1.1.3.1, we saw that toughening of aerospace resins can be achieved by developing a mate-

rial with optimally sized regions of structurally strong thermoset and fracture-resistant thermoplastic. Therefore, control over phase separation during the materials' creation is necessary to give the required mechanical properties. We will now discuss the science behind phase separation, both in general and in the more specific case of aerospace resins.

A polymer solution is defined as a polymer in a simple solvent, and a blend is a mixture of polymers. A polymer solution or blend containing two or more components can either be found in a homogeneously mixed state, or in a heterogeneous phase separated state with regions of different compositions.[22] The state adopted by the system depends on the chemistry of the components of the blend, the volume fractions (concentrations) of each of these, and the temperature. These factors are combined together to give a free energy for mixing, which determines the miscibility of the components. This section will present the most well-known method for calculating this free energy of mixing, the Flory Huggins model, along with its limitations and some improvements and alternatives.

1.2.1 Free energy

In equilibrium, whether a blend is found in a mixed or demixed state is entirely determined by which is lowest in free energy.[22] There are two definitions of free energy, depending on system conditions.

The Helmholtz free energy (F, given by Equation 1.1) is defined for systems with constant volume and temperature.[68] It is a temperature-dependent competition between the internal energy of the system (E, the sum of the kinetic energies and interactions of the constituent atoms) and the entropy (S, a measure of disorder derived from the number of microstates available to the atoms).[69] Theoretical models tend to use the Helmholtz free energy, because incompressible (constant volume) systems are much easier to treat via lattice models than

compressible ones.

$$F = E - TS \tag{1.1}$$

The Gibbs free energy (G, given by Equation 1.2) is defined at constant pressure and temperature.[68] It is the type of free energy generally used for describing physical systems, because it is easier to conduct experiments at constant pressure than constant volume, meaning that the system volume adjusts in order to keep the pressure constant (except in extreme cases such as explosions where the pressure changes too quickly to be compensated for). The equation for the Gibbs free energy is similar to that of the Helmholtz free energy, except that enthalpy (H) is used instead of internal energy to account for the volume changes.

$$G = H - TS \tag{1.2}$$

Enthalpy is the total heat content of a system, and is defined in Equation 1.3 as the sum of the internal energy and the product of pressure (p) and volume (V).[68]

$$H = E + pV \tag{1.3}$$

As we develop the theory for this thesis, we will use the Helmholtz free energy and treat our systems as incompressible with constant volume and temperature, but it is worth noting the distinction between the two.

1.2.2 Fundamentals of phase separation

To determine whether a blend will phase separate or not, we need to calculate the free energy of mixing (F_{mix}), which describes the difference in free energy between the mixed and demixed states. When $F_{mix} < 0$, the blend will be stable in a homogeneously mixed state, and when $F_{mix} > 0$, the system will tend to

phase separate.[22]

By specialising Equation 1.1 to the case of blend miscibility (Equation 1.4), it is clear that F_{mix} depends on the the energy and entropy of mixing, E_{mix} and S_{mix}, which are defined similarly to F_{mix} as the difference between the mixed and demixed states.[22]

$$F_{mix} = E_{mix} - TS_{mix} \tag{1.4}$$

Therefore, the challenge of determining the phase behaviour of a blend in equilibrium lies in accurately calculating the entropy and energy of mixing.

1.2.3 The Flory-Huggins model

The Flory-Huggins model is the most commonly used theory for predicting the free energy of mixing, and therefore the likelihood of phase separation, due to its relative simplicity and effectiveness in most cases. It is a mean-field lattice theory, which treats polymers as random self avoiding walks on a simple cubic lattice, with one segment per lattice cell, as shown in Figure 1.10. The entropy and energy of mixing are calculated separately, and then added together to give F_{mix} according to Equation 1.4.

1.2.3.1 Entropy of mixing

To investigate the entropy of mixing for a polymer blend, we will first recap the basic definition of entropy, before moving on to the calculations in the Flory-Huggins model.

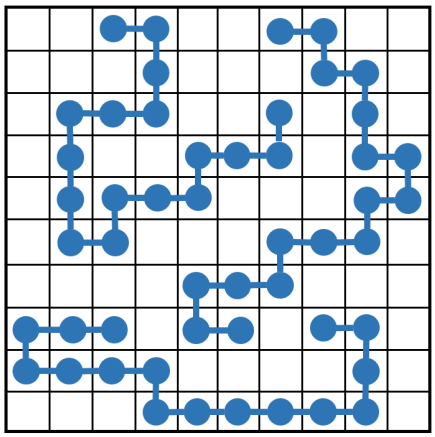

Figure 1.10: A schematic of polymers treated as random self avoiding walks on a simple cubic lattice as in the Flory-Huggins model. All empty lattice sites are treated as solvent molecules.

Definition of Entropy

In statistical physics, the macrostate of a system describes its macroscopic properties, with physically measurable values such as temperature, pressure, volume and density. In our case, the macrostate will be either mixed or demixed. On the other hand, a microstate describes a microscopic configuration of the system, with atomic positions and momenta taken into account.[69]

A simple way of visualising this is with an example of tossing two coins, as in Figure 1.11. There are three possible macrostates for this system: (1) both coins are heads, (2) both coins are tails, and (3) one coin is heads and the other is tails. When both coins are the same, there is only one way of organising the system, so there is only one microstate available for macrostates 1 and 2. However, for macrostate 3, where the coins are different, there are two possible microstates available, depending on which coin is heads and which is tails.

Using the Gibbs formula (Equation 1.5), the entropy of a macrostate can be characterised by the probabilities p_i of each constituent microstate i occurring.

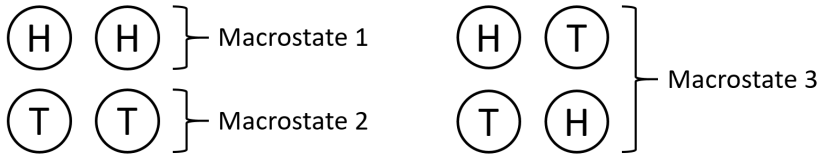

Figure 1.11: A pictorial showing the three macrostates available for a system of two simultaneous coin tosses. Macrostates 1 and 2 have only one microstate available to them as both coins are the same, but macrostate 3 has two available microstates depending on which coin is heads and which is tails.

k_B is the Boltzmann constant.[70]

$$S = -k_B \sum_i p_i \ln p_i \tag{1.5}$$

The Gibbs entropy formula works for all systems. However, a simplification can be made in the case where all microstates of the system are equally probable. This is true when the system is in global thermodynamic equilibrium and all macrostates have the same energy. Here, the probability p_i of being in one particular microstate i is simply the inverse of the total number of microstates (Ω) available to the macrostate (Equation 1.6).[70]

$$p_i = \frac{1}{\Omega} \tag{1.6}$$

We can subsitute this relation into Equation 1.5, and as our probabilities p_i are all now equal, we can replace the sum over the states with a multiplication by the number of states. This gives us Equation 1.7, the Boltzmann formula for entropy, which expresses the entropy of a macrostate in terms of its number of constituent microstates.[69,70]

$$S = k_B \ln \Omega \tag{1.7}$$

Flory Huggins Entropy

The entropy considered in the Flory-Huggins model is purely a configurational entropy generated from the geometric arrangements of the constituent molecules. The derivation for the Flory-Huggins entropy of mixing shown here follows closely that presented by Flory.[71].

In order to develop the theory for calculating the entropy of polymeric solutions and blends, it is prudent to begin by first considering the similar but more basic case of a blend of two simple liquids A and B. We will treat this system as a regular solution, which has random mixing similar to an ideal solution, but has energetic interactions that result in a non-zero enthalpy of mixing.[72]

We will assume these liquids have equivalently sized molecules, which each occupy one cell on the Flory-Huggins lattice (see Figure 1.12). There are n_A identical molecules of species A and n_B of species B. In total, there are $n = n_A + n_B$ molecules, and as all cells are occupied, n is also the total number of cells on the lattice.

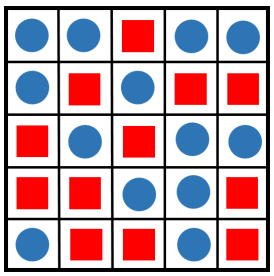

Figure 1.12: A pictorial showing the constituent molecules of two simple liquids on a Flory Huggins lattice. Molecules of species A are shown as red squares, and molecules of species B as blue circles.

The number of microstates Ω_M available to the mixed system is the number

of indistinguishable arrangements for all n molecules.

$$\Omega_M = \frac{n!}{n_A! n_B!} \tag{1.8}$$

The unmixed state consists of the pure components A and B on their own individual lattices. Due to the identical nature of their molecules, each of these components can only be arranged in one way, so Ω_A and Ω_B are both equal to 1. From Equation 1.7 ($S = k_B \ln \Omega$), the absolute configurational entropies of both pure components, and therefore also that of the unmixed state, are then zero.

The change in entropy due to mixing (S_{mix}) is the difference between the configurational entropies of the mixed and unmixed states. As we have determined that the unmixed state has no entropy, S_{mix} only has a contribution from the absolute entropy of the mixed state.

$$\begin{aligned} S_{mix} &= k_B \ln \Omega_M \\ &= k_B \ln \left[\frac{n!}{n_A! n_B!} \right] \\ &= k_B \left[\ln n! - \ln n_A! - \ln n_B! \right] \end{aligned} \tag{1.9}$$

Stirling's approximation ($\ln x! \approx x \ln x - x$) can be used to simplify the factorials in Equation 1.9. Remembering that $n = n_A + n_B$, the equation can then be rearranged.

$$\begin{aligned} S_{mix} &= k_B \left[n \ln n - n - (n_A \ln n_A - n_A) - (n_B \ln n_B - n_B) \right] \\ &= -k_B \left[n_A \ln \left(\frac{n_A}{n_A + n_B} \right) + n_B \ln \left(\frac{n_B}{n_A + n_B} \right) \right] \end{aligned} \tag{1.10}$$

The volume fraction (ϕ) of a component in a mixture is defined as the volume of that component divided by the total volume of all components. Therefore, in

our blend of two simple liquids, the volume fractions of the components A and B are given by Equations 1.11 and 1.12.

$$\phi_A = \frac{n_A}{n_A + n_B} \tag{1.11}$$

$$\phi_B = \frac{n_B}{n_A + n_B} \tag{1.12}$$

Substituting these definitions into Equation 1.10 gives us the change in configurational entropy when mixing two simple liquids.

$$S_{mix} = -k_B \left[n_A \ln \phi_A + n_B \ln \phi_B \right] \tag{1.13}$$

The value for S_{mix} given by Equation 1.13 is the entropy of mixing for the whole system, so is an extensive variable that depends on system size. Therefore, it is more appropriate to redefine S'_{mix} as an intensive variable, the change in entropy on mixing per molecule (or equivalently per lattice site). To achieve this, we can simply divide Equation 1.13 by $n = n_A + n_B$.

$$S'_{mix} = -k_B \left[\phi_A \ln \phi_A + \phi_B \ln \phi_B \right] \tag{1.14}$$

Now that the basic principles have been established, we can extend the theory to a polymer solution by replacing one of the simple liquid components B with polymer, and retaining the simple molecules of the solvent component A. In the lattice model, a polymer can be described as a series of N_B chain segments, each equivalent in size to a simple molecule, which must be placed on contiguous sites. An example is shown in Figure 1.13. Therefore, if we continue to define n_B as the number of molecules of species B, we now have $N_B n_B$ sites occupied by segments of polymer B. The total number of lattice sites is then $n = n_A + N_B n_B$.

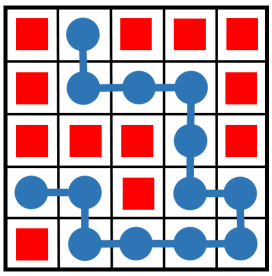

Figure 1.13: A pictorial showing the constituent molecules of a polymer solution on a Flory Huggins lattice. Segments of the polymer, shown as blue circles, are placed on contiguous sites on the lattice. Solvent molecules, shown as red squares, are placed on all remaining empty sites.

The number of microstates of the mixed system Ω_M can be calculated as the number of ways to arrange the n_B polymer molecules on the lattice, which is simply the product of the number of possible positions to place each segment. There is only one way to place the n_A indistinguishable solvent molecules on the remaining empty lattice sites, so the solvent gives no contribution to Ω_M.

If we assume that i of the n_B polymer molecules have already been placed on the lattice, the first step of each new polymer $(i+1)$ can then be placed on any of the $(n - N_B i)$ remaining empty lattice sites.

The number of available sites for the second segment of the polymer is more restricted, due to the necessity for placing it on one of the z neighbouring sites to the first segment. We must also take into account the probability f_i that this cell may already be occupied by a segment of a previous polymer. This gives us $z(1 - f_i)$ possible positions for the second step of polymer $(i+1)$. f_i can be evaluated as the average expectancy that a random cell is occupied, assuming an even distribution of molecules across the lattice.

$$f_i = \frac{N_B i}{n} \tag{1.15}$$

The number of possible positions for the third and subsequent polymer seg-

ments are calculated in a similar manner to the second segment, bearing in mind that one of the z neighbouring sites to the last segment is already occupied by the preceding chain. For the sake of simplicity, we will ignore the possibility that the chosen site could be occupied by any other previously-placed segments of the same chain, and retain our definition of f_i from Equation 1.15. Therefore, the number of available sites for each of the remaining $(N_B - 2)$ segments of polymer $(i + 1)$ is $(z - 1)(1 - f_i)$.

Overall, the number of possible arrangements ν_{i+1} for polymer $(i + 1)$ is calculated as a product of the number of possible positions for each constituent segment.

$$\nu_{i+1} = (n - N_B i)z(1 - f_i)(z - 1)^{N_B-2}(1 - f_i)^{N_B-2} \tag{1.16}$$

We can then substitute in the definition of f_i from Equation 1.15, for the sake of simplicity, replace the lone factor of z in Equation 1.16 with $(z - 1)$.

$$\begin{aligned}
\nu_{i+1} &= (n - N_B i)(z - 1)^{N_B-1}(1 - f_i)^{N_B-1} \\
&= (n - N_B i)(z - 1)^{N_B-1}\left(\frac{n - N_B i}{n}\right)^{N_B-1} \\
&= (n - N_B i)^{N_B}\left(\frac{z - 1}{n}\right)^{N_B-1}
\end{aligned} \tag{1.17}$$

Assuming that $n \gg N_B$, i.e. that a single polymer is small compared to size of the lattice, we can approximate the first term in 1.17 as $(n - N_B i)^{N_B} \approx \frac{(n-N_B i)!}{(n-N_B(i+1))!}$.

Now that we have calculated the number of arrangements for one polymer on the lattice, we can calculate the number of arrangements Ω_M for all n_B polymers,

bearing in mind their indistinguishability from one another.

$$\begin{aligned}\Omega_M &= \frac{1}{n_B!}\prod_{i=0}^{n_B-1}\nu_{i+1} \\ &= \frac{1}{n_B!}\prod_{i=0}^{n_B-1}\frac{(n-N_Bi)!}{(n-N_B(i+1))!}\left(\frac{z-1}{n}\right)^{N_B-1} \\ &= \frac{n!}{n_B!(n-N_Bn_B)!}\left(\frac{z-1}{n}\right)^{n_B(N_B-1)} \\ &= \frac{(n_A+n_B)!}{n_A!n_B!}\left(\frac{z-1}{n}\right)^{n_B(N_B-1)}\end{aligned} \tag{1.18}$$

The absolute configurational entropy of the mixed state (S_M) can then be obtained from the value of Ω_M, and simplified using Stirling's approximation and similar logic to Equation 1.10. In Equation 1.19, e is a mathematical constant, the base of the natural logarithm.

$$\begin{aligned}S_M &= k_B \ln \Omega_M \\ &= -k_B \ln\left[\frac{n_A!n_B!}{(n_A+n_B)!}\left(\frac{n}{z-1}\right)^{n_B(N_B-1)}\right] \\ &= -k_B\left[n_A \ln\left(\frac{n_A}{n_A+N_Bn_B}\right) + n_B \ln\left(\frac{n_B}{n_A+N_Bn_B}\right) - n_B(N_B-1)\ln\left(\frac{z-1}{e}\right)\right]\end{aligned} \tag{1.19}$$

In the case of the simple liquids at the beginning of this section, the configurational entropy of the pure components was zero, so the entropy change on mixing was equal to the absolute configurational entropy of the mixed state. This is no longer true when one of the components is polymeric. Here, the pure polymer component has zero entropy only when all the polymer molecules are perfectly aligned into a crystal. Therefore, even the pure polymer B has an inherent entropy associated with disordering the crystalline structure ($S_{disorder}$), which must be subtracted from the absolute entropy of the mixed state (S_M) to give the

change entropy for mixing (S_{mix}).

The entropy of the disordered pure polymer ($S_{disorder}$) is equivalent to the entropy of the mixed state (S_M) when there is no solvent present, i.e. Equation 1.19 with $n_A = 0$.

$$S_{disorder} = k_B n_B \left[\ln N_B + (N_B - 1) \ln \left(\frac{z-1}{e} \right) \right] \tag{1.20}$$

This allows the calculation of the change in configurational entropy when mixing a disordered pure polymer with a solvent.

$$\begin{aligned} S_{mix} &= S_M - S_{disorder} \\ &= -k_B \left[n_A \ln \left(\frac{n_A}{n_A + N_B n_B} \right) + n_B \ln \left(\frac{n_B}{n_A + N_B n_B} \right) - n_B (N_B - 1) \ln \left(\frac{z-1}{e} \right) \right] \\ &\quad -k_B n_B \left[\ln N_B + (N_B - 1) \ln \left(\frac{z-1}{e} \right) \right] \\ &= -k_B \left[n_A \ln \left(\frac{n_A}{n_A + N_B n_B} \right) + n_B \ln \left(\frac{N_B n_B}{n_A + N_B n_B} \right) \right] \end{aligned} \tag{1.21}$$

We must redefine the volume fractions of solvent A and polymer B from Equations 1.11 and 1.12 to take account of the fact that the each polymer occupies N_B lattice sites.

$$\phi_A = \frac{n_A}{n_A + N_B n_B} \tag{1.22}$$

$$\phi_B = \frac{N_B n_B}{n_A + N_B n_B} \tag{1.23}$$

We then arrive at the simplified equation for the Flory-Huggins configurational entropy change on mixing a polymer with a simple solvent.

$$S_{mix} = -k_B \left[n_A \ln \phi_A + n_B \ln \phi_B \right] \tag{1.24}$$

This expression for the extensive configurational entropy of mixing for a polymer solution (Equation 1.24) is identical to that for a blend of two simple liquids (Equation 1.13). However, a slight difference occurs when we rescale the value of S_{mix} to give an intensive expression. As the polymer and solvent molecules are different sizes, it is most prudent to take the entropy of mixing per lattice site (i.e. per molecule of solvent or segment of polymer). Therefore we divide Equation 1.24 by $n = n_A + N_B n_B$.

$$S'_{mix} = -k_B \left[\phi_A \ln \phi_A + \frac{\phi_B}{N_B} \ln \phi_B \right] \tag{1.25}$$

The theory can be extended further to treat the solvent as a second polymer component, giving the intensive change in configurational entropy of mixing two polymers together as Equation 1.26.

$$S'_{mix} = -k_B \left[\frac{\phi_A}{N_A} \ln \phi_A + \frac{\phi_B}{N_B} \ln \phi_B \right] \tag{1.26}$$

Here, the volume fractions of each species are once again rescaled to take into account that each of the n_A molecules of polymer A consists of N_A segments.

$$\phi_A = \frac{N_A n_A}{N_A n_A + N_B n_B} \tag{1.27}$$

$$\phi_B = \frac{N_B n_B}{N_A n_A + N_B n_B} \tag{1.28}$$

1.2.3.2 Energy of mixing

Section 1.2.2 showed that in order to predict phase separation via the free energy of mixing (F_{mix}), it is important to know the change in both entropy and energy during the mixing process. In Section 1.2.3.1, we calculated the configurational entropy of mixing for a blend of two polymers, so we must now focus on the energy.

The derivation given in this section will again follow the work of Flory.[71]

We need to calculate the change in energy (E_{mix}) when going from the separated pure components of polymers A and B to a miscible blend containing both polymer species. Therefore, we are only interested in the difference between the interaction energy in the miscible blend and that of the pure components.

As intermolecular forces in non-electrolytes decrease very rapidly with distance, it is reasonable to only consider the energetic interactions arising from nearest neighbour contacts between segments on the Flory-Huggins lattice. Therefore, the change in energy on mixing will originate from replacing some of the nearest neighbour contacts between segments of like species ($A-A$ and $B-B$) with unlike ones ($A-B$), as shown in Figure 1.14. The energy change associated with forming one such contact ($\Delta\epsilon$) can be described simply as a combination of the interaction energies between two segments of each type of polymer: ϵ_{AB}, ϵ_{AA} and ϵ_{BB}.

$$\Delta\epsilon = \epsilon_{AB} - \frac{1}{2}(\epsilon_{AA} + \epsilon_{BB}) \tag{1.29}$$

(a) Demixed *(b) Mixed*

Figure 1.14: Simple schematic showing the energetic interactions arising from nearest neighbour contacts in a demixed phase separated system and a mixed system. During mixing, nearest neighbour contacts between like species are replaced by those between unlike species.

E_{mix} will depend not only on the change in energy when forming one nearest neighbour contact of unlike segments, but also on the number of such contacts formed. We will calculate this as the number of nearest neighbours that segments of polymer species A have with segments of polymer species B in the mixed state,

but this could equivalently be carried out the other way around.

Each polymer segment has z nearest neighbours on the lattice, but two of these are already occupied by the preceding and following segments of the same chain. As the energetic interactions between chemically bonded segments are irrelevant here (they are the same for both the mixed and unmixed states), each segment has $(z-2)$ nearest neighbours available to form energetic contacts. Segments at the end of the chains have one additional contact available, but as polymers are long, the effect of this will be negligible. Note that for mathematical ease, the original Flory-Huggins model approximated the number of contacts per segment as z,[71] but it is more accurate to retain the value of $(z-2)$.[73] Some sources suggest that as interactions with other chains are more important to mixing than interactions with the same chain, an 'effective coordination number' z_{eff} should be used, which includes only the mean number of inter-chain nearest neighbours and therefore decreases in magnitude as the chain length is extended.[73,74]

We can calculate the total number of nearest neighbour contacts involving segments of polymer type A (c_A) from the number of type A segments in the system ($N_A n_A$).

$$c_A = (z-2) n_A N_A \tag{1.30}$$

Each of these contacts originating from type A segments leads to a segment of either species A or B. In the mixed state, we are interested in the number of contacts between unlike species, *i.e.* from A to B segments (c_{AB}). As in the derivation for the entropy S_{mix}, we will again assume that the molecules of each species are evenly distributed across the lattice. Therefore, the probability that a nearest neighbour to a type A segment will be a type B segment is equal to the probability that any random site on the lattice will be occupied by a B segment, i.e. the volume fraction of polymer B (ϕ_B). Therefore, the total number of

contacts between unlike species on the lattice can be estimated as Equation 1.31.

$$\begin{aligned} c_{AB} &= c_A \phi_B \\ &= (z-2) n_A N_A \phi_B \end{aligned} \tag{1.31}$$

We can now calculate the energy of mixing (E_{mix}) from the number of contacts between unlike species (c_{AB}) and the change in interaction energy of creating each such contact ($\Delta\epsilon$).

$$\begin{aligned} E_{mix} &= c_{AB} \Delta\epsilon \\ &= (z-2) n_A N_A \phi_B \Delta\epsilon \end{aligned} \tag{1.32}$$

E_{mix} in Equation 1.32 is an extensive variable that depends on the size of the lattice. Therefore, we must divide by the total number of segments (or lattice sites) to give the intensive value of E_{mix} per segment. This can then be simplified using the definition for the volume fraction of species A from Equation 1.27.

$$\begin{aligned} E'_{mix} &= \frac{(z-2) n_A N_A \phi_B \Delta\epsilon}{N_A n_A + N_B n_B} \\ &= (z-2) \phi_A \phi_B \Delta\epsilon \end{aligned} \tag{1.33}$$

Finally, we can remove the dependence on the lattice geometry by combining $(z-2)$ and ϵ into a single factor, the dimensionless χ interaction parameter. It is also customary to express the size of the interaction energies in units of $k_B T$.

$$E'_{mix} = k_B T \chi \phi_A \phi_B \tag{1.34}$$

$$\chi = \frac{(z-2)\Delta\epsilon}{k_B T} = \frac{(z-2)(\epsilon_{AB} - \frac{1}{2}(\epsilon_{AA} + \epsilon_{BB}))}{k_B T} \tag{1.35}$$

1.2.3.3 The Flory-Huggins equation and χ interaction parameter

The theories developed in Sections 1.2.3.1 and 1.2.3.2 for the entropy and energy of mixing can be substituted into Equation 1.4 to give the Flory-Huggins equation for the free energy change of mixing two polymers together, Equation 1.36.

$$\frac{F_{mix}}{k_B T} = \frac{\phi_A}{N_A} ln\phi_A + \frac{\phi_B}{N_B} ln\phi_B + \chi\phi_A\phi_B \tag{1.36}$$

As previously discussed, when $F_{mix} < 0$, the blend is stable in its mixed state, and when $F_{mix} > 0$, it will phase separate. The two configurational entropy terms on the right hand side are always negative, so drive the system towards mixing. As we saw in Section 1.2.3.1, they arise purely from the combinatorial entropy of non-interacting polymer chains.

The third term can be either positive or negative, depending on interactions between molecules in the blend. The derivation in the pure Flory-Huggins theory (Section 1.2.3.2) treats this interaction as purely energetic in origin. However, more modern approaches show us that the χ parameter also has an entropic contribution arising from sources other than the combinatorial entropy described in Section 1.2.3.1.[10] Therefore, an alternative temperature-dependent definition for the χ interaction parameter is generally used.[75]

$$\chi = a + \frac{b}{T} \tag{1.37}$$

Here, b is taken from the derivation of the energetic χ parameter in Section 1.2.3.2. It describes the energetic molecular interactions between polymer segments, where $b > 0$ if interactions between segments of the same species are more favourable than different species, and $b < 0$ if interspecies interactions are preferred over intraspecies ones.

The variable a in Equation 1.37 describes a non-combinatorial entropy in the system that can result from interactions between species. There are several possible sources for this. One of the most important factors is non-uniformity in the blend caused by energetic interactions, which then affects molecular packing.[71] For example, polymers with favourable interspecies interactions are likely to be found in more open conformations than those with unfavourable interspecies interactions. Some purely theoretical attempts to adjust the entropy of mixing to these energetic interactions have been made, but these are relatively complex, are only designed for simple mixtures or polymer-solvent systems, and are inaccurate at high concentration.[76,77] Similarly, strong energetic interactions such as hydrogen bonding in polar polymers can cause a regular structure to occur, reducing the entropy of mixing.[10]

Another possible contribution to the non-combinatorial entropy arises from the two blended polymers having different segment volumes, stiffnesses or geometries, necessitating one to contract in order to mix with the other.[10] This reduces the amount of free volume available to the polymer segments, and therefore gives an unfavourable entropy of mixing, with a positive a value. This behaviour cannot be described using a regular lattice model, but can be treated mathematically with equation of state theories, such as the Flory,[78–80] Patterson,[81,82] Prigogine,[83] or lattice-fluid[84–86] models. Equation of state theories describe each component of the blend by a characteristic temperature, pressure and specific volume, and calculate thermodynamic properties via the partition function.[87] Unlike the Flory-Huggins model, they treat blended systems as compressible due to the inclusion of free volume, which is necessary for studying unfavourable entropies of mixing.

It is also possible that changes in entropy could occur if the accessibility of energy levels or freedom of rotation are affected by mixing two polymers together.[88] Purely theoretical approaches to calculating χ tend to ignore these

entropic contributions.

The enthalpic part of the χ interaction parameter from Equation 1.35 is also non-trivial to calculate. It is proportional to the change in energy on mixing ($\Delta\epsilon = \epsilon_{AB} - \frac{1}{2}(\epsilon_{AA} + \epsilon_{BB})$). The intraspecies interaction energies ϵ_{AA} and ϵ_{BB} can be measured experimentally for simple liquids using the cohesive energy density, which is the energy of vaporisation (E_v) per unit volume (V) of material. Taking the square roots of cohesive energy densities gives Hildebrand solubility parameters (δ_p, Equation 1.38), which must be matched between materials to allow miscibility.[89–91]

$$\delta_p = \sqrt{\frac{E_v}{V}} \tag{1.38}$$

As polymers do not vaporise, the Hildebrand solubility parameters are in this case determined by testing the swelling of a cross-linked sample in a series of solvents, and assigning δ_p to be equal to Hildebrand solubility parameter of the solvent which induces the best swelling, i.e. the most miscible solvent.[92]

The calculation of the interspecies interaction parameter ϵ_{AB} has little theoretical basis. It is often estimated as the geometric mean of the intraspecies interactions (Equation 1.39), sometimes biased by a weighting factor g, which can be adjusted to fit with experimental data.[93] This methodology is purely empirical in nature, and is known to often give inaccurate results.[94]

$$\epsilon_{AB} = g\sqrt{\epsilon_{AA}\epsilon_{BB}} \tag{1.39}$$

The resulting χ parameter is then given by Equation 1.40, where A is a weighting coefficient.[90,91]

$$\chi_{AB} = A(\delta_{pA} - \delta_{pA})^2 \tag{1.40}$$

Due to the hydrocarbon nature of polymers, many are polar and able to form strong, directional hydrogen bonds which greatly affect the value of the χ parameter. One method for including these is via a three-dimensional (i.e. directional) Hansen solubility parameter,[95] which works well for many polymer-solvent mixtures, but is usually inaccurate for polymer-polymer blends.[92] Another approach is to use the infrared spectra of hydrogen-bonded blends to calculate their specific free energy contribution.[96,97]

Assuming independence of chain length, χ can also be determined by fitting small-angle scattering data to theoretically produced structure factors, or calculated from atomistic simulations.[73]

In addition to the temperature dependence of the χ parameter outlined in Equations 1.35 and 1.37, there can also be a dependence on the volume fractions or concentrations of the components in the blends, approximated mathematically as a power series of ϕ, but this is often neglected for ease.[98]

1.2.3.4 Assumptions and limitations of Flory-Huggins

Although the Flory-Huggins model works relatively well in many cases, its derivation requires some assumptions that can act as limitations or shortcomings in some situations. Here, these assumptions will be listed along with their implications.

- *The same lattice can be used for the segments of all types of molecule.* The use of a lattice is not inherently inaccurate, as only the first shell of nearest neighbours on the lattice is taken into account in the calculations, and this is similar to the well-defined solvation layer around each molecule in a real liquid. The lattice geometry is also irrelevant, as the number of nearest neighbours z drops out of the Equation 1.34 if a phenomenological

approach to calculating the χ interaction parameter is used. However, the assumption that all segments of each type of polymer or solvent molecule are equal in size and geometry to each other, both in the pure components and mixtures, has no physical basis and is a fundamental drawback of the lattice description.[71]

- *The conformations of the polymers in the solution are random.* This is equivalent to the assumption that the χ parameter has no entropic contribution, which was shown to be inaccurate in Section 1.2.3.3. It ignores the effect of energetic interactions on polymer conformation.

- *The local concentration of occupied lattice sites is equivalent to the lattice-wide average.* This is a mean-field assumption. It treats the segments of each polymer species as being randomly distributed over the lattice, and ignores the fact that previous polymer segments will have been placed on contiguous sites. This is usually a reasonable approximation, but if the volume fraction of one polymer is low, the segments will be clustered together with regions of much higher and lower concentration than the average.[71] Some corrections to this have been attempted by applying a field theory involving series expansions in volume fraction and number of nearest neighbours,[99,100] which give an improvement to the Flory-Huggins model for high density systems, but still overestimate the entropy.[101,102].

- *The theory is designed for linear polymers.* The number of available sites for each polymer segment used in the derivation for S_{mix} assumes each polymer segment is connected to two others. This is true for linear thermoplastic polymers, but does not well represent branched ones (e.g. polymer stars, combs or thermosets), where some of the segments have higher functionalities. In addition, the different architectures of branched polymers will affect the packing, and therefore the prevalence of each type of nearest neighbour

energetic interaction. Taken together, these features mean that the calculated free energies are less accurate for branched polymers than for linear ones.

- *The interaction energy term is poorly defined.* The geometric mean construction for calculating interspecies energetic interactions has little theoretical basis and is often inaccurate, meaning that calculations for the energy of mixing are unreliable.

1.2.3.5 Developments to the Flory-Huggins model

During the last few sections, we have seen that several attempts to improve on the Flory-Huggins model have been made, particularly in the area of improving the calculation of the χ interaction parameter. Although these methods have improved predictions of phase separation, the limitations of the model ensure that theoretical developments and alternatives are still being sought.

Self-consistent field theory

One such alternative is the self-consistent field theory method, or SCFT, first applied to polymers by Edwards.[103] SCFT is a numerical implementation of a mean-field theory, and allows an iterative approach to deriving the interactions between polymer segments. An initial prediction for the segment-segment interaction is chosen, and this, along with the segment concentration, is used to calculate a potential. A non-interacting polymer chain is then added into the system, and the concentration profile is checked for consistency with the calculated potential. The interactions are then turned on for the added chain, and the concentration profile and potential are repeatedly adjusted until consistency is achieved.[29]

Edwards' initial use of the SCFT model[103] was to predict the conformations of linear polymers, treating them as random walks with an excluded volume interaction between the polymer segments. Various SCFTs have since been used to study phase separation in multicomponent systems. They are among the most successful theories in polymer blend research, but are held back by their reliance on mean-field assumptions.[104]

Lattice cluster theory

The lattice cluster theory or LCT, attributed to Dudowic and Freed, is a method of improving the calculation of the entropic contribution to the χ parameter. It aims to reproduce experimental observations by introducing non-random mixing effects and a χ dependence on molecular weight, composition and pressure.[105] It is one of the very few theories capable of taking the architecture of branched polymer into account in free energy calculations.

An extended lattice model that allows each polymer segment to cover multiple lattice sites is used, where each site represents a 'united atom group' containing fewer atoms than a monomer, allowing more detailed chemical structures to be included. Examples of the united atom groups in poly(propylene) are shown in Figure 1.15. A partition function is then calculated in the high temperature limit ($T \to \infty$), where all possible positions for the bonds between united atom groups are summed over, with respect to excluded volume constraints. This produces a cluster expansion for the partition function, and subsequently the free energy, as a double power series of the inverse coordination number z and the interaction energy ϵ. A coefficient can be chosen so that the first term in the free energy expansion is equivalent to the combinatorial entropy in the Flory-Huggins model, and further terms then provide corrections for non-random mixing.[105]

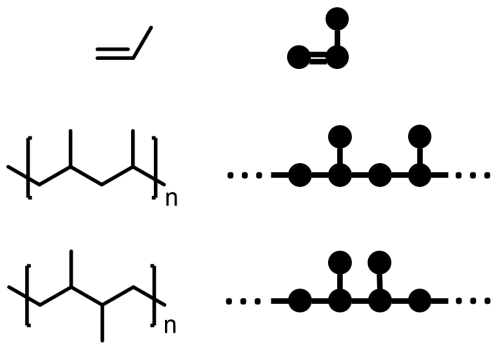

Figure 1.15: The chemical structures of the monomer propylene and two possible architectures of its resulting polymer polypropylene, depending on the relative orientations of the monomer units. The lattice cluster theory 'united atom groups' for these molecules are also given. Here, each united atom group represents one carbon atom with its attached hydrogens, allowing the chemical structure of the monomer to be included in the model.

The lattice cluster theory is a well-renowned model that can be adapted to both incompressible and compressible systems, and is able to reproduce experimental mixing behaviour in many cases.[106] However, due to the truncation of the power series in ϵ (required because of the difficulty of calculating the cluster expansion), it is only valid at high temperatures.[105] Due to the lengthy mathematics required for calculating all possible bond orientations, it also only works well for branched polymers with a simple and repetitive architecture, so has limited applicability in the case of randomly and heavily branched thermosets.

1.2.3.6 Computational alternatives to the Flory-Huggins model

In addition to theoretical methods, there are various modelling techniques available that may potentially allow insight to be gained into the phase behaviour of polymer blends.

The most widely-known technique is molecular dynamics, which is designed to simulate the physical movements of atoms and molecules to give informa-

tion about the dynamic evolution of the system's morphology. Force fields are used to characterise interactions between particles, and trajectories are calculated according to Newton's laws of motion. Due to the realistic nature of the movements, molecular dynamics simulations have the potential to be highly accurate, although this of course depends on the choice of force field.[107–109] Their drawback lies in the computational expense of carrying out the calculations. Only very small simulation boxes with a few tens or hundreds of molecules can be used; unfortunately this is not large enough to study phase separation, which involves long-range, collective motion. In addition, timesteps must be taken on the order of a femtosecond to avoid inaccuracies due to discretisation, with the result that the entire simulations can only span a time period of nanoseconds or microseconds. These inefficiencies can be combatted to some extent by coarse graining, where large parts of a molecule are incorporated into a single particle rather than treating each atom individually, but this is not sufficient to allow simulations long enough to cover the phase separation process.[110]

Dissipative particle dynamics is a related mesoscopic technique that has experienced more success in the area of phase behaviour. This method treats entire molecules or groups of molecules as single particules, and no longer employs the use of complex forcefields. Instead, simplified soft pairwise potentials are used for particles within a cut-off distance of each other. These consist of a combination of conservative, dissipative and random forces, such that mass and local momentum are conserved but energy is not. The effect of these simplified calculations means that longer lengthscales (100 nm) and time periods (tens of microseconds) can be studied than in molecular dynamics.[111] Dissipative particle dynamics has been applied successfully to the study of phase behaviour in diblock copolymers[112] and simple binary blends,[113,114] but has not been extended to systems containing more complex polymers or branching.

Most computational modelling of phase behaviour in polymeric systems has

been restricted to Monte Carlo simulations. Instead of tracking small, realistic movements of molecules, Monte Carlo uses larger-scale, often unphysical, structural reorganisations according to a random sampling methodology (see Section 1.4 for more detail). This means that the kinetics of the phase behaviour cannot usually be tracked with time, but equilibrium morphologies of the materials can be found much more quickly than with other techniques. There are many different algorithms available to simulate polymers with Monte Carlo methods, most of which take place using a self-avoiding walk on a lattice for ease of simulation.[109] Off-lattice techniques using the bead-spring model also exist, however, where bond lengths between polymer segments are allowed to vary with an a potential relating to the spring constant of the bond.[110] There are several examples of the use of Monte Carlo modelling to study phase behaviour of multicomponent polymer blends in the literature,[74,115,116] although finite-size scaling techniques are often required to account for the small size of the simulation boxes, and little research has been undertaken into systems containing branched molecules.[117]

1.2.4 Mechanisms of phase separation

We have already discovered that the value of the free energy of mixing is sufficient evidence to determine whether or not a polymer blend in equilibrium is susceptible to phase separation. However, more information is required to ascertain the mechanism by which the phase separation takes place. This section will discuss the two possible mechanisms, nucleation and growth and spinodal decomposition, as well as circumstances required for each to take place and the compositions of the resulting phases.

1.2.4.1 Upper and lower critical solution temperatures

Blend composition can be described via the volume fraction of one of the components. For ease of notation, we can denote this volume fraction simply as $\phi_A = \phi$, where in an incompressible blend, the volume fraction of the other component is $\phi_B = (1 - \phi)$.

By plotting $F_{mix} = 0$ onto a graph of temperature against blend composition, a U-shaped curve called the binodal is produced. This characterises the stability of the blend: for temperatures and blend compositions inside the binodal curve, the blend will be driven towards phase separation, but outside the binodal curve, it will be stable in the mixed state.[22] The binodal curve can be approximated experimentally by the cloud-point curve, or CPC, which denotes the first temperature at which phase separation is observed for each blend composition. This is often carried out by using microscopy to observe the point where the material becomes clouded and reduces in transmittance due to scattered light from phase boundaries.[118]

Two possible examples of binodal curves for different types of blend are shown in Figure 1.16.

The typical, intuitive case is that of the inverted U-shape shown in Figure 1.16a, where the blend is phase separated at low temperatures and mixed at high temperatures. This generally occurs when $b > 0$ in Equation 1.37, so that intraspecies energetic interactions are favoured over interspecies ones.[119] Therefore, energetics tend to drive the system towards phase separation, but entropy, which favours disorder, encourages mixing. As entropy has more impact on free energy at higher temperatures ($F = E - TS$), there will be a certain temperature for each blend composition above which entropy will dominate and the system will transition from a demixed to mixed state. This is called upper critical solu-

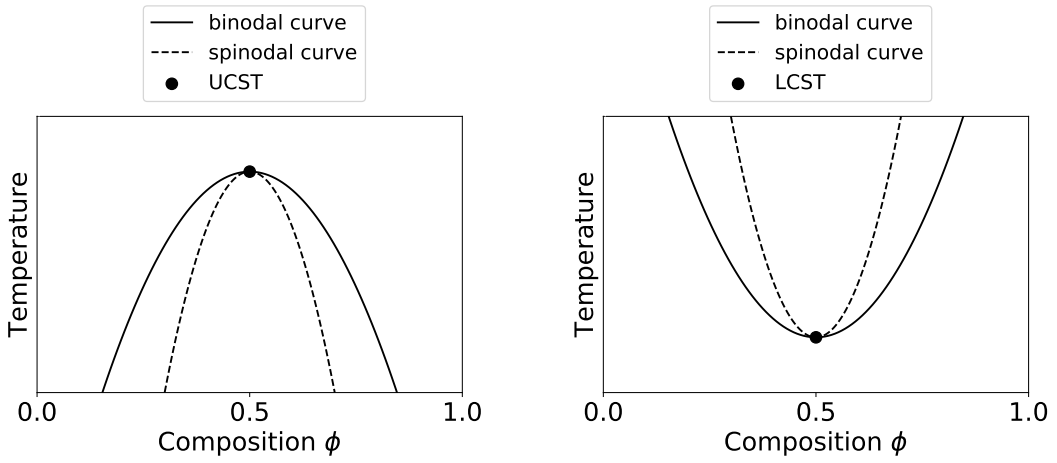

(a) UCST *(b) LCST*

Figure 1.16: Phase diagrams of a blends exhibiting (a) upper critical solution behaviour and (b) lower critical solution behaviour. The solid line represents the binodal curve and the dashed line the spinodal curve.

tion temperature (USCT) behaviour, where the UCST describes the temperature above which the blend components are miscible in all proportions.[11]

The less intuitive case is lower critical solution temperature (LCST) behaviour, shown in Figure 1.16b. Here, the blend is miscible at low temperatures, but will phase separate as temperature increases. This behaviour can occur when $b < 0$, so that interspecies interactions are favoured over intraspecies ones, which encourages mixing when energy is dominant at low temperatures.[119] An example of this is a system where there are strong hydrogen bonds that can only form with the involvement of both species,[10] such as in an amine-water blend.[120]

Another origin of LCST behaviour is a non-combinatorial entropy that discourages mixing (see Section 1.2.3.3). This is usually due to compressibility effects, where the components experience different amounts of thermal expansion at high temperatures, so that the more expanded component must contract to mix with the other, reducing free volume and freedom of motion. This is particularly prevalent in polymer-solvent blends close to the boiling point of the

solvent, where the solvent molecules become diffuse, but the polymer segments are covalently bonded together so cannot easily move apart.[10,121]

LCST behaviour is very rare for blends of small molecules, but is surprisingly common for polymers due to these compressibility effects. In fact, many polymer blends that exhibit UCST behaviour also have an LCST at higher temperatures, producing a graph with two U-shaped curves of different inversions (see Figure 1.17).[122]

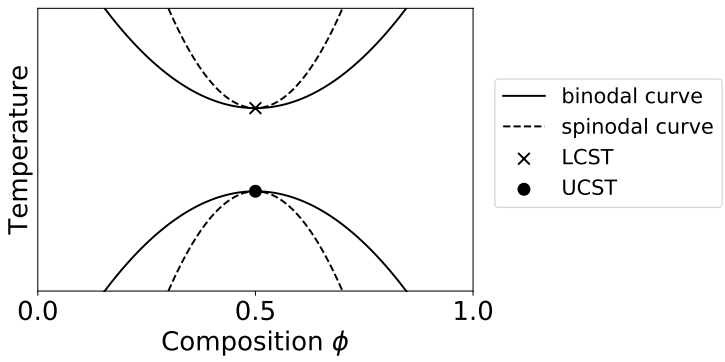

Figure 1.17: An example phase diagram of a polymer blend showing both lower and upper critical solution behaviour. UCST behaviour is observed at low temperatures due to configurational entropy, and LCST behaviour is observed at higher temperatures when compressibility effects come into play.

1.2.4.2 Concentration fluctuations

Even in a homogeneous miscible blend of two or more components, molecular motion causes small spatial variations in the concentrations of each component. These variations typically have a characteristic domain size for each blend composition and temperature, typically ranging from 1 nm to 1 µm. The fluctuations become larger as the spinodal is approached from the miscible part of the phase diagram, so increase upon cooling for systems with UCST behaviour and increase upon heating for systems with LCST behaviour. The sizes and shapes of

the constituent molecules can also affect concentration fluctuations, as covalent bonds between polymer segments introduce connectivity that cannot be broken by molecular motion, which then affects the entropy.[123]

Concentration fluctuations are often visualised both theoretically and experimentally using radial distribution functions and structure factors, which will be described in detail in Sections 3.2.3.3 and 3.2.3.4. The radial distribution function, abbreviated RDF or $g(r)$, describes the variation of density (overall or of a particular species) with distance from a reference particle. The structure factor, $S(q)$, is the Fourier transform of the RDF and can be determined experimentally by x-ray or neutron scattering.[70]

Concentration fluctuations give insight into the mechanisms behind phase separation. Inside the binodal curves in Figure 1.16, there is a second U-shaped curve called the spinodal curve, which is defined where there is no curvature of F_{mix}, i.e. when $\frac{\partial^2 F_{mix}(\phi)}{\partial \phi^2} = 0$. Using the Flory-Huggins equation for F_{mix} (Equation 1.36), an expression for the spinodal curve can be obtained.

$$\frac{1}{N_A \phi_A} + \frac{1}{N_B \phi_B} - 2\chi = 0 \tag{1.41}$$

Inside the spinodal, the curvature is negative, and between the spinodal and binodal, the curvature is positive.[22] The effect of this is seen most easily by plotting F_{mix} against composition, as in Figure 1.18.

Concentration fluctuations involve a small change in composition from ϕ to $\phi + \delta\phi$ and $\phi - \delta\phi$, with the overall free energy an average of the two new compositions. Inside the spinodal curve, where the curvature is negative $\left(\frac{\partial^2 F_{mix}(\phi)}{\partial \phi^2} < 0\right)$, small changes in concentration cause the overall free energy to decrease, meaning that any small fluctuations are amplified and the mixed blend is completely unstable.

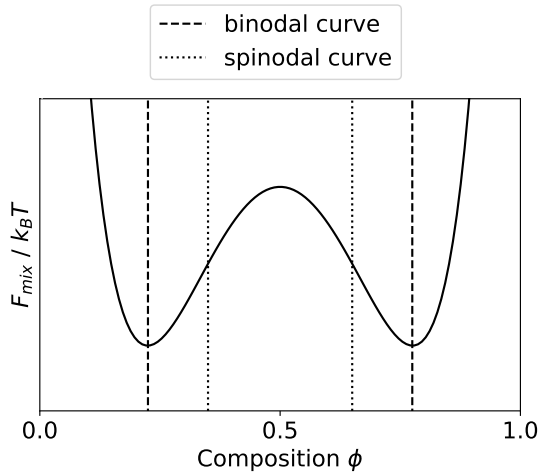

(a) Curvature of F_{mix}

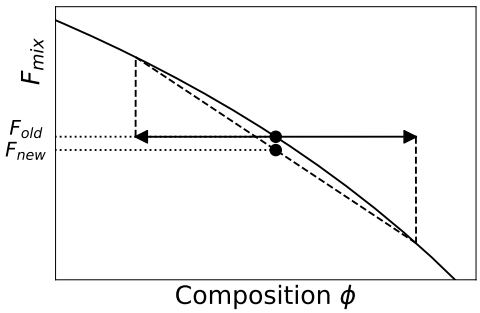

(b) Unstable blend behaviour inside the spinodal.

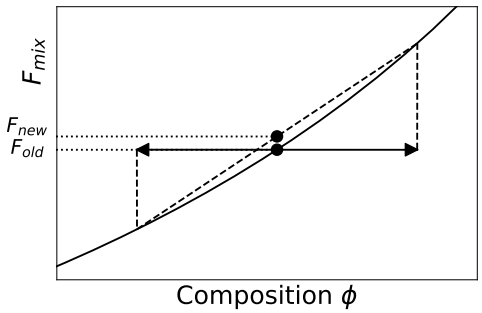

(c) Metastable blend behaviour between the spinodal and binodal.

Figure 1.18: Figure (a) shows the free energy of mixing against blend composition. Inside the spinodal, the curvature of F_{mix} is negative and between the spinodal and binodal, the curvature is positive. (b) For a blend inside the spinodal, small fluctuations in concentration will decrease the overall free energy of the system, so the blend will be unstable. (c) Between the spinodal and binodal, small changes in composition increase the free energy, so the blend is metastable and will only separate if large enough fluctuations are experienced that the free energy barrier can be overcome.

However, where the curvature is positive, between the binodal and the spinodal $\left(\frac{\partial^2 F_{mix}(\phi)}{\partial \phi^2} > 0\right)$, small changes in concentration cause an increase in the average free energy. Therefore, there is a free energy barrier that must be overcome by

sufficiently large concentration fluctuations before a reduction in free energy can be achieved. This causes the mixed blend to be metastable, meaning that it is not thermodynamically stable, but is stable to small fluctuations.[22]

1.2.4.3 Nucleation and growth

In the metastable region between the binodal and spinodal, phase separation takes place via a nucleation and growth mechanism, which can be explained relatively well by classical nucleation theory, which describes homogeneous nucleation.[22] This theory has some limitations, including the fact that it assumes small clusters of material exhibit bulk-like properties for the interfacial tension and the stability of the interior phase, when there is little evidence that this is the case.[124] It also assumes that spherical clusters are formed by a stepwise addition of particles, and ignores the possibility of merging and fragmentation.[125]

However, the theory provides a simple and effective description for the process of nucleation and growth, so will be described here. Fluctuations in concentration cause a droplet of a new phase to form. This is associated with a drop in free energy, due to the formation of a bulk core phase in its thermodynamically favourable state. However, there is also a free energy penalty for creating new interface around the droplet. Both of these effects are included in Equation 1.42, which describes the change in free energy for forming a droplet of radius r, and is plotted in Figure 1.19. ΔF_v is the free energy change per unit volume of forming thermodynamically stable phase from the metastable phase, so is negative, and γ is the interfacial energy per unit area of the new surface, so is positive.[22]

$$\Delta F(r) = \frac{4}{3}\pi r^3 \Delta F_v + 4\pi r^2 \gamma \tag{1.42}$$

For small droplets, the surface area is large compared to the bulk, so $\Delta F(r) >$

0 and the droplet dissipates in order to decrease the free energy back to the original value. However, if a droplet caused by random concentration fluctuations has a radius larger than the critical size r_c (which can be obtained by setting $\frac{\partial \Delta F(r)}{\partial r} = 0$), the change in free energy due to the bulk stable phase is large compared to the size of the new interface. Here, the free energy barrier in Figure 1.19 can be overcome, and the free energy is then reduced by growing the droplet. [22]

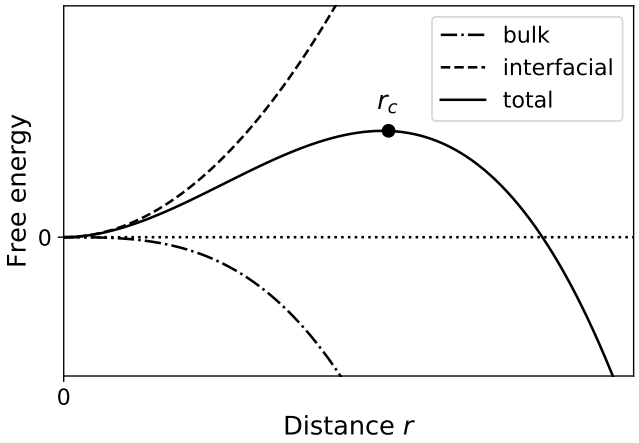

Figure 1.19: A plot showing the free energy change during nucleation and growth as a function of droplet size. The total free energy change is given, along with the contributions from the formation of a favourable new bulk phase and an unfavourable interface. Droplets of new phase smaller than the critical radius r_c will dissipate, and those larger than r_c will be amplified.

Throughout growth, the droplets remain spherical in order to minimise interfacial area. Therefore, a nucleation and growth morphology is characterised by dispersed spheres, but if enough growth takes place for the spheres to touch, they can interconnect to form a continuous structure. During nucleation and growth, the composition of the droplet phase remains constant over time. [10]

1.2.4.4 Spinodal decomposition

In the unstable region of the phase diagram inside the spinodal curve, any spatial variations in composition are amplified. This is unusual because it involves the flow of material from regions of low to high concentration, but the driving force of free energy reduction remains unchanged.[22]

During spinodal decomposition, systems become inhomogeneous. The total free energy can then be expressed as the integral of the spatially-varying local free energy density $f(\boldsymbol{x})$ over the volume of the blend, where $\boldsymbol{x}$ is a vector denoting position.[22]

$$F = \int_V f(\boldsymbol{x}) d\boldsymbol{x} \tag{1.43}$$

$f(\boldsymbol{x})$ encapsulates both the thermodynamic stability of the local phase at position $\boldsymbol{x}$ (with a bulk free energy f_0 per unit volume for a uniform blend of average composition ϕ), and also the unfavourable interfaces within the system (via a concentration gradient across the interfaces with respect to position $\boldsymbol{x}$). A phenomenological equation was proposed by Cahn and Hilliard in 1958 as the simplest mathematical form capable of reproducing these effects. This is given by Equation 1.44, where κ is the gradient energy coefficient, which is treated as a constant, a reasonable assumption if the concentration gradients are fairly shallow. $\nabla\phi$ denotes the concentration gradient across phase boundaries with respect to position $\boldsymbol{x}$.[22,126]

$$f(\boldsymbol{x}) = f_0(\phi) + \kappa \left[\nabla\phi(\boldsymbol{x})\right]^2 \tag{1.44}$$

Chemical potential (μ) is the free energy change associated with adding or removing particles of a given species, which happens for each region during the composition changes of a phase transition. Therefore, μ can be defined as the

derivative of free energy F with respect to composition ϕ.[126]

$$\mu = \left(\frac{\partial F(\phi)}{\partial \phi}\right)_{T,V,N} \tag{1.45}$$

Using the definition for free energy density in Equation 1.44, we have a description for the chemical potential during spinodal decomposition.[22,126]

$$\mu = \frac{\partial f_0(\phi)}{\partial \phi} + 2\kappa\nabla^2\phi(\boldsymbol{x}) \tag{1.46}$$

To maintain equilibrium, chemical potential must remain constant across the whole system.[126] Therefore, the flux ($\boldsymbol{J}$, the rate of flow of material through the system), is proportional to the gradient of the chemical potential, with a coefficient M that describes the mobility of the particles in the system. M is called the Onsager transport coefficient and is treated as a constant.[22] The negative sign in Equation 1.47 is introduced to ensure that M is always positive.

$$\boldsymbol{J} = -M\nabla\mu \tag{1.47}$$

By substituting Equation 1.46 for the chemical potential into Equation 1.47, we get an expression for the flux in a spinodally decomposing system in the limit of small fluctuations.

$$\boldsymbol{J}(\phi(\boldsymbol{x})) = -M\left[\frac{\partial^2 f_0(\phi)}{\partial \phi^2}\nabla\phi(\boldsymbol{x}) + 2\kappa\nabla^3\phi(\boldsymbol{x})\right] \tag{1.48}$$

Finally, we can introduce the concept of a continuity equation for conservation of mass, which states that the material inside a region can only change when there

is a flux of material flowing in or out through the region's boundaries.[22,126]

$$\frac{\partial \phi(\boldsymbol{x})}{\partial t} = -\boldsymbol{\nabla} \cdot \boldsymbol{J}(\phi(\boldsymbol{x})) \tag{1.49}$$

By substituting in our expression for flux (Equation 1.48), this allows us to arrive at the well-known Cahn-Hilliard equation, which describes the early stage time evolution of the composition at each point of a system undergoing spinodal decomposition.[22,126]

$$\frac{\partial \phi(\boldsymbol{x})}{\partial t} = M \frac{\partial^2 f_0(\phi)}{\partial \phi^2} \nabla^2 \phi(\boldsymbol{x}) + 2M\kappa \nabla^4 \phi(\boldsymbol{x}) \tag{1.50}$$

We can compare the Cahn-Hilliard equation with Fick's second law, the standard diffusion equation, where D is the diffusion coefficient.[22]

$$\frac{\partial \phi(\boldsymbol{x})}{\partial t} = D \nabla^2 \phi(\boldsymbol{x}) \tag{1.51}$$

The equivalence of the leading terms in Equations 1.50 and 1.51 shows us that during spinodal decomposition, diffusion occurs with an effective diffusion coefficient of $D_{eff} = M \frac{\partial^2 f_0(\phi)}{\partial \phi^2}$.[22] M is defined to always be positive, but we know from Section 1.2.4.2 that the curvature of the free energy is negative inside the spinodal. Therefore, during spinodal decomposition, $D_{eff} < 0$, and matter flows from areas of low to high concentration.[22] This causes each phase to become more and more rich in one component, aiding the phase separation process.

Solutions to the Cahn-Hilliard equation are given by Equations 1.52 and 1.53.[22] These describe the time and position dependent local compositions in the system, against a reference of the average composition ϕ_0. $\boldsymbol{q}$ denotes the wavevector of the variation in composition; the magnitude of this is the wavenumber q, which is related to the wavelength or lengthscale of the concentration fluctua-

tions by $q = \frac{2\pi}{\lambda}$. As only the scalar product of $\boldsymbol{q}$ with itself appears in Equation 1.53, the directional properties of wavevector $\boldsymbol{q}$ are unimportant and only the magnitude, i.e. the wavenumber q, is of interest. A is an amplitude coefficient.

$$\phi(\boldsymbol{x}, t) - \phi_0 = A cos(\boldsymbol{q} \cdot \boldsymbol{x}) \exp(R(q)t) \tag{1.52}$$

$$R(q) = -Mq^2 \left[\frac{\partial^2 f_0(\phi)}{\partial \phi^2} + 2\kappa q^2 \right] \tag{1.53}$$

$R(q)$ is an amplification factor, which determines the stability of composition variations with wavenumber q. According to Equation 1.52, concentration fluctuations below a critical wavenumber, where $R(q) > 0$, will grow exponentially in the blend. This defines a characteristic domain size for the phase separated regions during spinodal decomposition.[22] Fluctuations with smaller wavelengths are unstable as they cause a large amount of costly surface area between the phases, and those with higher wavelengths are unfavourable as they require matter to be transported over large distances.

The absence of the vector form of q in Equation 1.53 implies that spinodal decomposition is direction-independent. Therefore, a random pattern of bicontinuous phases is formed with a characteristic lengthscale, as in the schematic shown in Figure 1.20a.[22] Over time, higher order terms in the Cahn-Hilliard equation come into play, and the lengthscale of the phase separation increases in order to reduce interfacial energy in the system. This process is known as coarsening, and can eventually lead to the bicontinuous morphology breaking down, first to interconnected globules and then to fully separated spherical regions, as shown in Figure 1.20.[22,127]

Spinodal decomposition can be tracked experimentally via x-ray or neutron scattering, an example of which is shown in Figure 1.21. Initially, an intensity peak appears at the characteristic wavenumber for spinodal decomposition. Over

time, the peak moves towards lower q as the lengthscale of the phase separation increases, and the intensity increases as the compositions of the phases become more distinct.[22]

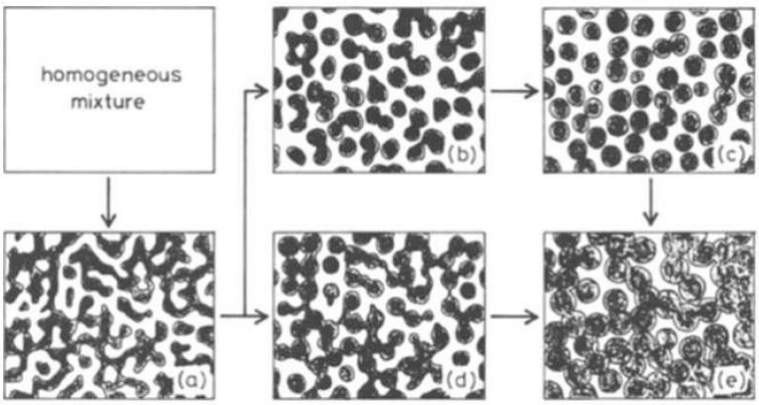

Figure 1.20: A schematic of the spinodal decomposition coarsening process to give dispersed spheres and then an interconnected globule structure. Reproduced with permission from Yamanaka et al.*[127]*

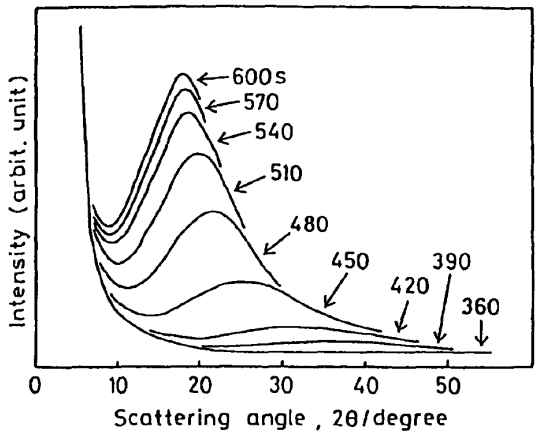

Figure 1.21: The characteristic changes with time in the height and position of the intensity peak in a scattering experiment for a system undergoing spinodal decomposition. Reproduced with permission from Yamanaka et al.*[127]*

1.2.4.5 Compositions of phase separated regions

It is a common misconception that unstable blends phase separate into regions containing pure components. Instead, the regions are just richer in one species than the system average. We have already stated that the composition of the droplet phase remains constant during nucleation and growth, and that the compositions of the bicontinuous phases become increasingly divergent during spinodal decomposition. Here, we will discuss a method for determining the exact compositions of the phase-separated regions.

If we plot the Flory-Huggins equation (Equation 1.36) for the free energy of mixing F_{mix} onto a graph against composition ϕ when χ is less than a critical value χ_c, we get a U-shaped curve with a single minimum at a mixed composition (see Figure 1.22a). The lowest free energy state that will be adopted is at this minimum, so phase separation will not occur.[22]

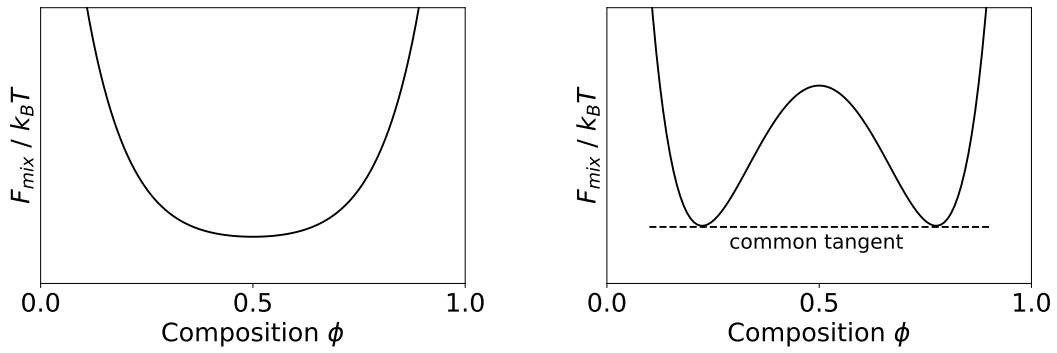

(a) $\chi < \chi_c$ *(b)* $\chi > \chi_c$

Figure 1.22: Plots of free energy of mixing for systems with different χ interaction parameters. (a) For $\chi < \chi_c$, there is a single free energy minimum, so the mixed state will be stable. (b) For $\chi > \chi_c$, there are two free energy minima, so the system will phase separate into the two compositions which share a common tangent.

However, for $\chi \geq \chi_c$, we have two minima, with the mixed state appearing at a local maximum between them. For this case, shown in Figure 1.22b it is most

favourable for the system to separate into two phases. For two phases to coexist in equilibrium, their chemical potentials must be equal. As chemical potential can be described as the derivative of free energy with respect to composition (Equation 1.45), the compositions of the coexisting phases can be determined as the two points on the free energy curve that share a common tangent (see Figure 1.22b).[22]

By plotting these common tangent points onto a graph of temperature against composition (Figure 1.23), we can view the compositions of the separated phases as a coexistence curve. A blend at a point on the graph susceptible to phase separation (i.e. inside the binodal), will split into two phases α and β along a horizontal tie-line. The compositions of the new phases (ϕ_α and ϕ_β) are determined by the ϕ values at the coexistence curve along this tie-line.[22]

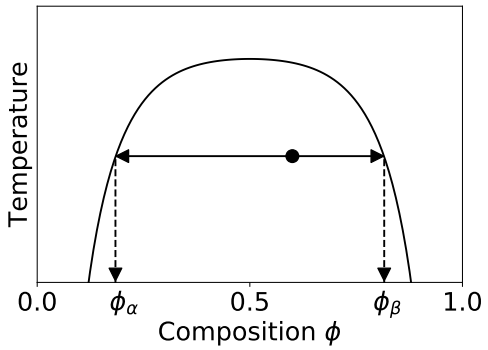

Figure 1.23: Coexistence curve for an example UCST system. An unstable blend will separate along a horizontal tie-line into two phases with equal chemical potential, the compositions of which are determined using a common tangent construction.

The volume fraction of each new phase can be determined by the lever rule. Working along the tie line, the closer a stable composition is to the starting composition, the more of that phase will be present. The volume fraction of new phase α can be calculated as the difference in compositions between the overall starting composition and the other new phase β, divided by the total length of

the tie line.[22]

$$\phi_\alpha = \frac{\phi - \phi_\beta}{\phi_\beta - \phi_\alpha} \tag{1.54}$$

For a two component system, the coexistence curve is identical to the binodal, so anything inside the coexistence curve will phase separate. However, for multicomponent systems, or those with heterogeneities in molecular size (polydispersity), the two curves are different.[128]

1.2.5 Reaction-induced phase separation

In most cases where phase separation is experienced, the temperature is altered to move the system into an unstable region of the phase diagram. However, the picture can be more complicated if one of the components undergoes a polymerisation reaction, as is the case during curing of an aerospace resin. Thermoplastic polymers are dissolved into a mixture of epoxy monomers or oligomers and curing agent. The molecular weight and degree of polymerisation of the thermosetting epoxy component B increases over time.[129] This affects the Flory-Huggins equation (Equation 1.36, repeated in Equation 1.55) by increasing the value of N_B.

$$\frac{F_{mix}}{k_B T} = \frac{\phi_A}{N_A} ln\phi_A + \frac{\phi_B}{N_B} ln\phi_B + \chi\phi_A\phi_B \tag{1.55}$$

The configurational entropy terms (the first two terms on the right hand side of Equation 1.55) are always negative and drive mixing. Therefore, increasing the value of N_B causes the term $\frac{\phi_B}{N_B} \ln \phi_B$ to become less negative, increasing the free energy of mixing F_{mix}. During this process, the entropy per polymer segment decreases, but the entropy per molecule increases.

The shape of the phase separation diagram is affected as F_{mix} changes, with the binodal and spinodal curves both shifted up for blends with UCST behaviour,

and down for those with LCST behaviour. In all cases, the size of the unstable region of the phase diagram increases as the polymerisation reaction proceeds. This means that over time, a reacting mixture tends to become unstable and phase separation begins to take place, even when operating at a constant cure temperature with initially miscible polymers. This process is called reaction-induced phase separation, or RIPS.[130]

1.3 Complications in aerospace blends

We now have a basic understanding of how and why phase separation takes place, but there are two features of aerospace resins that complicate the picture by reducing the mobility of the molecules in the system: gelation and glass transitions. These effects mean that blends cannot always reach their equilibrium states, causing the final morphology to be affected by kinetics as well as thermodynamics.[130]

1.3.1 Gelation

Gelation of a thermoset describes the formation of cross-links to produce a 3D network. Initially, cross-linking causes a collection of individual clusters known as a sol to appear. Further bonding reactions then attaches these clusters together into a large macromolecule called a gel. Theoretically, the gel point, or sol-gel phase transition, describes the critical point at which an infinite macromolecule spanning the entire width of the material is formed.[131] Experimentally, it is usually determined by rheological measurements, where a sharp increase in viscosity occurs so that the material can no longer flow.[132] The material effectively transitions from a viscous liquid to a solid.

Models of gelation are known as percolation theories, because they describe

percolation of bonds forming through the material. Classical percolation theories were initially put forward by Flory and Stockmayer in the 1940s and are still widely used today.[133–135] They allow both the position of the gel point and the molecular weight distribution in the material to be predicted. Flory's work[133] requires the calculation to be started with trifunctional or tetrafunctional monomer units, and is only valid in the latter case for long chains of uniform length. Stockmayer presents an alternative and superior approach that allows monomers of any functionality,[134] and that was later extended to allow any arbitrary initial size distribution.[135]

These classical theories make several assumptions. One notable example is that they neglect cyclic bonds, so intramolecular bonds cannot be formed.[131,134] There is some experimental justification for this assumption, because only a small percentage of bonds are observed to be intramolecular at gelation[133], but it is still a restriction for thermosetting polymers. Another important assumption is that all unreacted functional groups are assumed to be equally reactive, independent of excluded volume interactions or steric hindrance,[131,134] so this limits the applicability of the model to systems that conform with these requirements. The relative speeds of diffusion and reaction are also not considered, meaning that the resulting molecular size distributions are temperature-independent.[131]

The omission of cyclical bonds allows classical percolation theories to be represented by a Bethe lattice or Cayley tree (see Figure 1.24), where each vertex represents a monomer with a number of branches according to its functionality f. Note that f must be greater than or equal to 3 to allow cross-linking to take place. If p is the conversion, or fraction of bonds that have already formed, then assuming equal reactivity, it is also the probability of each individual bond being formed. The critical gel point is then given by the percolation threshold p_c, the

lowest value of p that allows an infinite network to be formed.

$$p_c = \frac{1}{f-1} \tag{1.56}$$

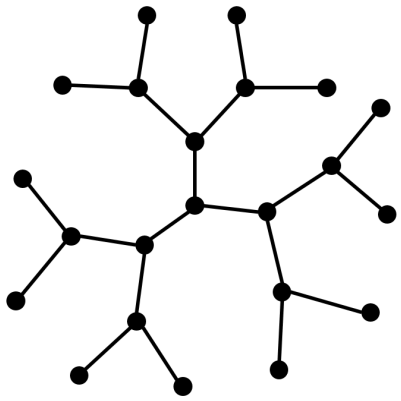

Figure 1.24: A Bethe lattice or Cayley tree where each monomer has a functionality of 3. Cyclical bonds are forbidden.

This relation holds for systems where all monomers can react with each other and have the same functionality. It also works in situations where there are two types of functional group that can only react with each other and not with themselves, such as in an epoxy resin and curative system under normal reaction conditions.[134] Here, one type of monomer must be bifunctional ($f = 2$) so that it cannot increase the number of cross-links, which is a good representation of some epoxy monomers such as DGEBA. The other type of functional group must reside on monomers with $f \geq 3$, such as a diamine curative with $f = 4$.

These treatments also allow the molecular weight distributions within the reacting mixture to be calculated. We work with Stockmayer's model,[134] as we have shown its functionality requirements match those of an epoxy-diamine blend. The volume fraction $\phi(N)$ of each cluster containing N monomers is given by Equation 1.57, where n is the number of diamine curative monomers in each

cluster, s the number of bifunctional epoxy monomers in each cluster, $m(n, s)$ is a distribution law, and k is a normalisation constant that ensures a total volume fraction of 1.[136]

$$\phi(N) = kN \sum_{n_{min}}^{n_{max}} m(n, s) \tag{1.57}$$

Following some *"tedious"* mathematics outlined by Stockmayer[134] and then simplified, a formula for the distribution law $m(n, s)$ can be obtained for our situation of bifunctional epoxy monomers and tetrafunctional diamines. This is given by Equation 1.58. As before, p represents the conversion in terms of the fraction of possible amine groups that have reacted. r describes the stoichiometry as the ratio of reactive amine hydrogens to epoxide groups in the system.

$$m(n, s) = \frac{(1-p)^{(1+3n-s)}(1-rp)^{(1+s-n)}r^{(n-1)}p^{(n+s-1)}(3n)!}{n!(3n+1-s)!(s-n+1)!} \tag{1.58}$$

The comparative values of n and s are restricted by the possible architectures of clusters that can be formed from monomers with the required functionalities.[134] As demonstrated in Figure 1.25, the possible values of s in a non-cyclical cluster containing n curative monomers range from $s_{min} = n-1$ to $s_{max} = 3n+1$. For a cluster with a total of N monomers, the maximal value of n occurs when s is minimised, and vice versa.

Substituting these constraints into Equation 1.57 allows the volume fraction of clusters with each degree of polymerisation N to be determined. If we assume the epoxy and curative monomers have equal molecular weights, it allows us to also calculate a molecular weight distribution for the clusters during cross-linking. Due to some simplifying assumptions made during the derivation, this model is only valid during the early stages of cure, when the conversion is low and the system is well below the gel point.[134]

Over the years, various improvements to the classical percolation theories have been attempted.[137] Most of these involve percolation of nearest-neighbour bonds on a regular square lattice rather than a Cayley tree, so they can include the effects of excluded volume, steric hindrance and cyclic bonds neglected by the previous classical models. However, they are more complex, requiring Monte Carlo simulations or series expansions to evaluate, and do not always give improved results.[131,138]

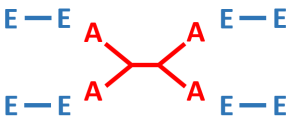

(a) $n = 1,\ s = 0 \rightarrow 4$

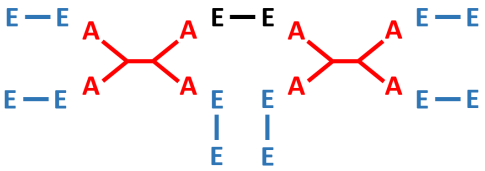

(b) $n = 2,\ s = 1 \rightarrow 7$

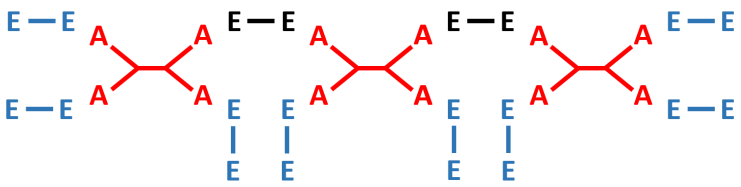

(c) $n = 3,\ s = 2 \rightarrow 10$

Figure 1.25: The number of epoxy (s) and amine (n) molecules that can be found in a non-cyclical cluster are restricted by geometry. For a particular number of tetrafunctional amine molecules, the number of attached difunctional epoxy molecules can range from $s_{min} = n - 1$ *to* $s_{max} = 3n + 1$*. Epoxies necessary to maintain connectivity are shown in black and optional ones are shown in blue.*

Gelation can also be incorporated into the Flory-Huggins model by introducing a polydispersity to the molecular sizes in the branched component that depends on the level of cure. This causes an adjustment to the combinatorial entropy term for the branched component in the Flory-Huggins equation (Equation 1.36 or 1.55), so that it is now represented as a sum over the sizes of the branched molecules, as shown in Equation 1.59.[139,140]

$$\frac{\phi_B}{N_B} \ln \phi_B \rightarrow \sum_i \frac{\phi_{Bi}}{N_{Bi}} \ln \phi_{Bi} \tag{1.59}$$

Another method of introducing the effect of gelation, attributed to Binder and Frisch, is to add an elastic term to the free energy.[141] This generates an energy penalty for deviations in the positions of the polymer segments from their optimum locations, and therefore represents the rigid network nature of the gelled thermoset. This theory was later extended by Henderson *et al.*,[142], who introduced both a time evolution of gelation and a local dependency, so that the elastic term only appears in domains where cross-linking has taken place.

Molecular weight distributions within a polymerised material can be characterised by several types of average molar weight. The three simplest are M_n, the number average molar weight (Equation 1.60), M_w, the weight average molar weight (Equation 1.61), and M_z, the Z or centrifugal average molar weight (Equation 1.62), where N_i is the number of molecules with molecular weight M_i. Taken together, these characterise the overall shape of the distribution. Typically $M_n < M_w < M_z$, and the polydispersity of a polymerised material can be described via a polydispersity index of M_w/M_n. Different experimental techniques measure different averages; for example NMR expresses molecular weight in terms of M_n, and GPC can measure both M_n and M_w.

$$M_n = \frac{\sum_i M_i N_i}{\sum_i N_i} \tag{1.60}$$

$$M_w = \frac{\sum_i M_i^2 N_i}{\sum_i M_i N_i} \tag{1.61}$$

$$M_z = \frac{\sum_i M_i^3 N_i}{\sum_i M_i^2 N_i} \tag{1.62}$$

1.3.2 Glass transitions

In addition to gelation, there is another phenomenon that causes polymer viscosity to diverge, arresting molecular motion and suppressing phase separation. Vitrification describes the rapid decrease in mobility when a material passes through its glass transition temperature (T_g) to become an amorphous solid, as discussed in Section 1.1.2.3.

The glass transition is a poorly understood feature of soft matter research. It occurs when a material is cooled without freezing, so that there is no structural change but the mobility of the constituent molecules falls to effectively zero. This is often explained using the theory of cooperativity. Each molecule in an amorphous material is held within a shell, or cage, of nearest neighbour molecules, as demonstrated in Figure 1.26. Many 'cage' molecules must move together, cooperatively, to allow the captured molecule to escape, which produces a large energy barrier for molecular motion. At temperatures above T_g, random Brownian motion is enough to allow the molecules to move past each other, so each molecule is able to easily hop between cages. However, when the temperature falls below T_g, the molecules have less kinetic energy, so Brownian motion is no longer sufficient to allow the molecules to escape their cages, and mobility is drastically reduced. The glass transition marks the point at which no mobility is observed on an experimental timescale.[22]

This means that the exact position of the glass transition depends on the experimental technique used to measure it. It is therefore not generally regarded

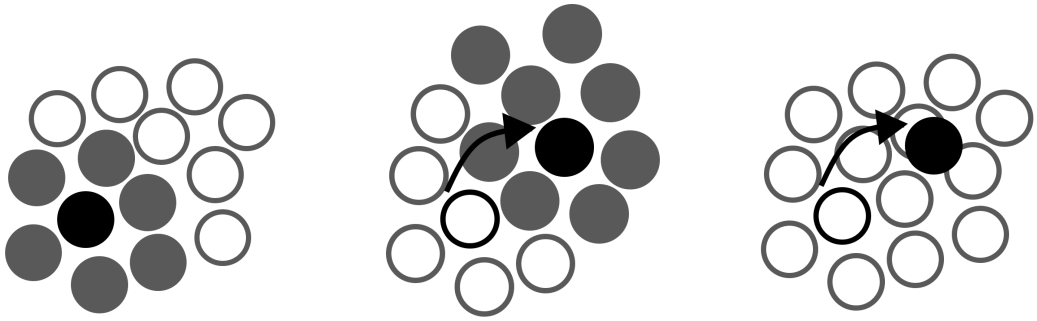

(a) Molecular cages in an amorphous material.

(b) $T > T_g$, material can flow.

(c) $T > T_g$, material cannot flow

Figure 1.26: (a) Each molecule (shown in black) in an amorphous material is held in place by a shell or cage of other molecules (shaded in grey) that must be escaped in order for the material to flow. (b) At temperatures above T_g, the molecules have enough Brownian motion to allow the caged molecule to escape its shell and contribute to flow. The cooperative motion required for this move is shown by the shaded molecules. (c) At temperatures below T_g, the molecules do not have enough kinetic energy to perform this cooperative motion, so the material cannot flow and behaves like a solid.

as a true phase transition, but as more of a kinetic transition. It describes the point at which the system can no longer sample all of its microstates on the experimental timescale, and is therefore not necessarily measured in its equilibrium state.[22]

Although glass transitions do not exhibit structural transformations, they are associated with sudden changes in material properties, such as discontinuities in heat capacity and thermal expansivity.[20,22] This allows T_g to be measured experimentally, usually by DSC (differential scanning calorimetry, which considers the change in heat capacity), TMA (thermal mechanical analysis, which looks at thermal expansivity), or DMA (dynamic mechanical analysis, which examines the dynamic modulus, or strength under vibration).[143]

Because glass transition behaviour is governed by molecular motion, the T_g of a material is dependent on the types of molecules present and therefore the

composition.[143] Generally, larger molecules inhibit molecular motion to a greater extent, so materials containing larger polymers will have a higher T_g. This means that as the thermoset component of a polymer blend is cured, the T_g of all phases containing thermoset will be increased. If the T_g of a particular phase rises above the cure temperature, that phase will become vitrified and the local morphology will be frozen in place.

The T_g of a homogeneous blend can be calculated from those of the pure components, along with their volume fractions, using empirical formulae such as the Fox,[144] Gordon-Taylor[145] or Kwei[146] equations. Heterogeneous blends have a separate glass transition for each phase, with the T_g of each dependent on its local composition.[143]

1.3.3 The effect of gelation and T_g on RIPS

Both gelation and glass transitions can cause a diverging viscosity to occur in any or all phases during the cure of a thermoset/thermoplastic blend. This drastically decreases the mobility of molecules within the blend, so that phase separation is suppressed and morphologies become locked in, with higher miscibility than would be expected from the thermodynamics. Polymer chains are unable to rearrange into their lowest free energy conformations and a 'quasi-equilibrium' is reached.[138] This makes systems undergoing reaction-induced phase separation extremely difficult to study, as there is a complex balance between the competing effects of thermodynamically-favourable phase separation and the mobility restriction of the curing reaction.[127]

This competition has been described in terms of a 'K value' which is the ratio between the rates of phase separation and polymerisation, where the polymerisation reaction controls the changes in the phase diagram during curing.[41] A high K value means that the kinetics of phase separation are much faster

than the reaction kinetics, so the system is always in its equilibrium state and a large amount of phase separation can occur. On the other hand, a low K value implies that the system increases in molecular weight quickly, so that viscosity suppresses phase separation before equilibrium is reached and the blend will be more miscible than the thermodynamics suggest.[41] The most interesting case is at intermediate values of K, where the critical temperature for phase separation to occur is only just below the temperature at which the viscosity diverges.[129] This means the cure rate greatly affects the amount of phase separation that can take place before structure fixation occurs, so that the final morphology can be controlled by changing the curative or cure temperature.[129]

In corroboration with this, Henderson *et al.*[142] found (with their model for gelation with an evolving elastic term mentioned in Section 1.3.1) that as the cure proceeds, phase separation becomes unfavourable due to energetically-costly deformations in the network. In some cases, this not only prevents phase separation from occurring, but also causes previously-separated phases to remix. Increasing the volume fraction of the branched thermoset allows more network to form, so reduces the amount of phase separation that can take place.

Another peculiarity of the arrested mobility of polymer molecules is the occurrence of secondary phase separation. This arises when curing causes the molecular weight to increase within a particular phase such that the previously-separated phase becomes unstable itself. Mobility restrictions prevent the entire system from rearranging, so instead a secondary level of phase separation takes place within the unstable phase, usually by nucleation and growth.[138] This can produce complex and unusual morphologies (e.g. smalls spheres inside a larger bicontinuous structure), which makes determining the mechanical properties of the resulting materials very difficult.

1.4 Monte Carlo simulations

Now that we have described the physical properties of phase separating systems, we will discuss one of the main computational techniques used to study them in this thesis, Monte Carlo modelling. This is a type of molecular simulation that aims to use a model system to predict the properties of a real experimental system. A stochastic method based on random numbers is used to move the model system between a variety of possible states, and the expectation values of thermodynamic variables are estimated as averages of the simulated system passing through these states.[108]

1.4.1 Importance sampling

Due to restrictions based on computational efficiency, a Monte Carlo simulation is not able to visit all possible microstates of a system in the same way an experimental system can. Therefore, only a small subset of the states is considered when calculating expectation values for variables, which introduces inaccuracy into the results. In order to minimise this inaccuracy, an appropriate probability distribution must be chosen for the subset of states.[147]

A simple choice would be to choose all states with equal probability, but this would lead to very poor results. High energy states would be frequently sampled in the simulation, when in real life they are only rarely experienced due to the domination of the ground state.

Instead, an importance sampling technique is used to ensure that the probability of each state occurring in the simulation is approximately equal to the statistical weight that the state would have in the equivalent real life system. To achieve this, states are chosen with a Boltzmann probability distribution using a Markov chain process.[147]

1.4.2 Markov chains

A Markov chain is a stochastic process that randomly generates a new state ν from the current state of the system μ, with a transition probability $P(\mu \to \nu)$. Transition probabilities are constant over time and only depend on the states μ and ν, so are independent of any previous conditions of the system. At each step of the simulation, a new state ν is chosen, although this can be equivalent to the previous state μ.[147]

1.4.3 Acceptance ratios

In a Monte Carlo simulation, we randomly choose a new target state ν and attempt to transition to it from the current state μ. We then choose whether or not to accept this transition based on the desired probability distribution. Therefore, the overall probability of transitioning from state μ to state ν consists of two parts.

$$P(\mu \to \nu) = g(\mu \to \nu)A(\mu \to \nu) \tag{1.63}$$

$g(\mu \to \nu)$ is the selection probability, or the probability of choosing the target state ν from the initial state μ. $A(\mu \to \nu)$ is the acceptance ratio, or probability of accepting the transition, given that the target state ν has already been chosen.[147]

1.4.4 Metropolis algorithm

The Metropolis algorithm is generally used to calculate acceptance ratios in statistical mechanics simulations, due to its ability to create a Boltzmann distribution using a simple methodology. Here, all selection probabilities $g(\mu \to \nu)$ are taken to be equal, and acceptance ratios are chosen using the equivalent definitions in

Equations 1.64[147] and 1.65.[108]

$$A(\mu \rightarrow \nu) = \begin{cases} \exp\left(-\frac{E_\nu - E_\mu}{k_B T}\right) & \text{if } E_\nu > E_\mu. \\ 1 & \text{otherwise.} \end{cases} \tag{1.64}$$

$$A(\mu \rightarrow \nu) = \min\left[1, \exp\left(-\frac{E_\nu - E_\mu}{k_B T}\right)\right] \tag{1.65}$$

Therefore, if a new state ν is chosen with a lower energy than the previous state μ, it is always accepted. If ν has a higher energy than μ, it is accepted with a probability of $\exp\left(-\frac{E_\nu - E_\mu}{k_B T}\right)$. In practice, this is achieved by selecting a random number between 0 and 1, and accepting the move if this is lower than the calculated value of $A(\mu \rightarrow \nu)$.[108,147]

1.4.5 Ergodicity

In order for a Monte Carlo simulation to be valid, it must obey the condition of ergodicity. An ergodic system is defined as one which has the same properties when either a time average or an ensemble average is taken.[108] In practice, maintaining ergodicity means the Markov process must be able to reach any state of the system from any other state, if the simulation is left to run long enough.[147]

1.4.6 Detailed balance

The transition probabilities for a Markov chain must ensure that an equilibrium Boltzmann distribution is maintained. To remain in equilibrium, the average number of accepted moves leaving a state must be equal to the number of accepted moves entering it from any other state. In practice, a stronger equilibrium

condition of detailed balance is usually applied, because this is more convenient to enforce. In this case, the total number of transitions between states in one direction ($\mu \rightarrow \nu$) must be exactly equal to the number of transitions in the reverse direction ($\nu \rightarrow \mu$). The total number of transitions depends both on the probability of the system being in the initial state, and the transition probability from that state to the other. The detailed balance condition can therefore be expressed by Equation 1.66, where N_i is the number of molecules in state i.[108]

$$N_\mu P(\mu \rightarrow \nu) = N_\nu P(\nu \rightarrow \mu) \tag{1.66}$$

1.5 Aims

The work in this thesis will focus on investigating the thermodynamics of phase separation in blends of branched and linear molecules.

The change in free energy associated with the mixing process is one of the most important factors governing the phase behaviour of polymer blends. Unfortunately, current techniques used to calculate this are designed for linear polymers or those with very simple, regular branching structures, and are not applicable to the randomly branched architectures of the polymers used in aerospace composites. Therefore, Chapter 2 aims to develop a computational method to allow the entropy and free energy of polymers with arbitrary branching points to be calculated.

The work in Chapter 3 develops a Monte Carlo modelling methodology to directly simulate concentration fluctuations within polymer blends. Concentration fluctuations are the precursor for phase separation, so by comparing their sizes between different systems, an indication of the relative stabilities of the blends can be obtained. The aim here was to design a process for simulating these con-

centration fluctuations in blends containing branched and linear polymers, and to characterise the sizes of the fluctuations using radial distribution functions. Structure factors can then be calculated, which should in the future allow comparison between computational predictions and neutron scattering experimental data. By calibrating the model to these experimental results, information about industrially-relevant blends could be obtained with fewer expensive and time-consuming experiments.

The aim of Chapter 4 was to design a simple model experimental system, similar to an aerospace blend, that would enable concentration fluctuations to be measured by neutron scattering. The system should allow the competing effects of temperature and cure extent on phase behaviour to be isolated and compared. An attempt will also be made to extract χ interaction parameters for each of the blends. This data would be very useful, as the experimental system will ideally be used to validate the computational model designed in Chapter 3, and knowledge of the χ interaction parameters would allow the intersegment energetic interactions to be calibrated.

Chapter 2

Entropy and free energy

2.1 Introduction

We saw in Section 1.2 that the phase behaviour of polymer solutions and blends in equilibrium depends entirely on their free energy of mixing. A mean-field lattice theory known as the Flory-Huggins model is usually used to calculate this, but it has shortcomings that make it unsuitable for studying branched polymers. It calculates entropy and energy completely separately, each according to mean-field assumptions. This is often inaccurate, because it does not account for the interplay between the two: polymers with strongly attractive segment interactions will form compact conformations with correspondingly low entropy; those with strongly repulsive segment interactions will form very stretched out conformations, also with low entropy; and polymers with intermediate interaction energies will form open coils with higher entropy. Similarly, strong entropic effects will influence the most likely polymer conformations and therefore the prevalence of each type of energetic interaction.

The Flory-Huggins model was designed for linear polymers, so it calculates

the entropy based on each segment having two connections to neighbours along the chain. This makes the entropy calculations inaccurate for branched polymers, where some segments have higher functionalities. There are fewer ways to place segments around a higher functionality branch point, so branching reduces entropy. In addition, branching influences the packing of the segments on the lattice, and therefore the interactions between the segments of polymer (and solvent where relevant), meaning that energy calculations are also unreliable.

The lattice cluster theory, discussed in Section 1.2.3.5, is the only relatively successful theoretical approach to calculating the free energy of branched polymers.[105] Unfortunately, it relies on series expansions that become mathematically complex for intricately branched polymers, so is only really applicable to those with simple and repetitive architectures.

Due to the difficulty of adding variability in segment functionality into a theoretical model for entropy and free energy calculations, the most sensible way to include more detail is to use computer simulation. Unfortunately, the most commonly used methods for computationally calculating free energy do not apply to branched polymers. For example, thermodynamic integration calculates free energy compared to that of a known reference state, by integrating along a thermal path between the two states.[108] The ideal chain can be used as a reference state for linear polymers,[148,149] but no suitable reference state exists for branched polymers.

Another widely used method for calculating free energy is the Widom particle insertion method, which examines the effect of adding ghost particles into the system.[150] The analogue for polymer systems is to attempt to insert an entire polymer molecule into the system. This has been done successfully for small linear molecules,[151–153] but is difficult without causing overlaps in even moderately dense systems of branched polymers or long linear chains. An alternative is to

add a single test segment onto the end of one of the polymers in the system,[154] but this is not so simple for branched polymers, where adding the segment onto different parts of molecule would produce different results.

The most promising starting point for calculating the free energy of branched molecules is to adapt the hypothetical scanning simulation method,[155,156] designed for linear polymers and also applicable to simple molecules, to more complex architectures. This chapter will discuss the theory behind the original method, the developments required to adapt it to branched molecules, and the resulting entropies and free energies calculated for a series of small molecules with various architectures and energetic interactions.

2.2 Background theory

A good theoretical representation of a polymer is a self-avoiding walk (SAW) on a lattice, used in the Flory-Huggins model and shown in Figure 2.1a. The polymer is split into Kuhn length segments, where one Kuhn length is defined as the longest section of the chain that can be treated as freely-jointed with its neighbouring segments.[22] To maintain connectivity, each segment is placed on a neighbouring lattice site to the previous segment. Only one segment may be placed on each site, to represent the excluded volume of the atoms in the segments. An analogy can be made in the case of branched polymers by depicting them as self-avoiding trees (SATs, see Figure 2.1b), which are similar to SAWs but with different bonding.

In the purely entropic case, the polymers segments are placed randomly according to the rules defined above. Nearest neighbour energetic interactions may also be included, which bias the segment positions towards conformations with

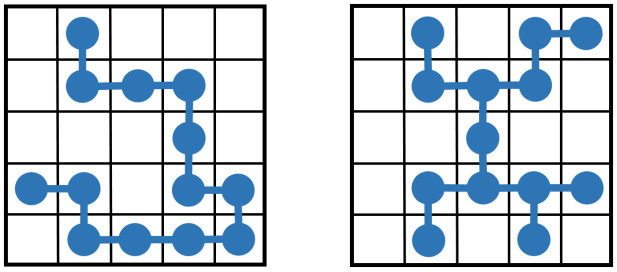

(a) Self-avoiding walk *(b) Self-avoiding tree*

Figure 2.1: Lattice representations of (a) a linear polymer as a self-avoiding walk, and (b) a branched polymer as a self-avoiding tree.

favourable energies.

2.2.1 Statistical mechanics of self avoiding walks

In this section, thermodynamic variables for self-avoiding walks and trees will be defined. Assuming the canonical ensemble, the partition function (Z) for a SAW or SAT is given by Equation 2.1, where i runs over all possible conformations (microstates) of the polymer, E_i is the total interaction energy for that conformation, k_B is the Boltzmann constant and T is the temperature.[157]

$$Z = \sum_i \exp(-E_i/k_BT) \tag{2.1}$$

Therefore, the probability (P_i^B) of finding a particular conformation i of the SAW or SAT in a Boltzmann distributed ensemble is given by Equation 2.2.

$$\begin{aligned} P_i^B &= \frac{\exp(-E_i/k_BT)}{Z} \\ &= \frac{\exp(-E_i/k_BT)}{\sum_i \exp(-E_i/k_BT)} \end{aligned} \tag{2.2}$$

The expectations values for energy (E) and entropy (S) are given by Equations

2.3 and 2.4 respectively, and the free energy (F) is calculated by combining these together into Equation 2.5.[157]

$$E = \sum_i P_i^B E_i \tag{2.3}$$

$$S = -k_B \sum_i P_i^B \ln P_i^B \tag{2.4}$$

$$\begin{aligned} F &= E - TS \\ &= \sum_i P_i^B E_i - T\left[k_B \sum_i P_i^B \ln P_i^B\right] \\ &= \sum_i P_i^B \left[E_i + k_B T \ln P_i^B\right] \end{aligned} \tag{2.5}$$

In the purely entropic case with no energetic interactions (i.e. all $E_i = 0$), the partition function is simply equal to the total number of conformations for the self-avoiding walk or tree, so $P_i^B = 1/Z$ and the probability of finding each conformation is equal. Free energy can be expressed by $F = -k_B T \ln Z$, and as all states have an equal energy of zero here, the entropy follows as in Equation 2.6.[149]

$$S = -F/T = k_B \ln Z = -k_B \ln P_i^B \tag{2.6}$$

2.2.2 The hypothetical scanning method

For an exact calculation of the free energy of a SAW or SAT according to Equation 2.5, it is necessary to know P_i^B. However, as this involves summing over all the possible conformations, the quantity of which grows exponentially with the number of polymer segments, the calculation quickly becomes intractable. Instead, it is more appropriate to estimate the value of P_i by simulation, for example using the hypothetical scanning (HS) method.[155,156]

The basis of HS relies on the principle that samples of the same equilibrium system produced by different simulation methods will have the same properties.[149] Therefore, a Boltzmann distributed ensemble of self-avoiding walks or trees can be produced by any method, such as a Monte Carlo simulation (see Section 2.2.4). The free energy can then be calculated and averaged over this ensemble to give an estimate of the true value, with larger ensembles generally giving more accurate results.

An estimate of the probability ($P_i(f)$) of creating one conformation in the ensemble can be made using a similar method to the Flory-Huggins model (see Section 1.2.3.1), by multiplying together the probabilities of placing each segment of the polymer in turn.

In the HS methodology, the single segment probabilities ($P_j(f)$, where j denotes the position of the segment in the polymer) are calculated by rebuilding each polymer one segment at a time, holding all the previously placed segments before j frozen in space. All of the possible positions for the next f segments that maintain the required connectivity are searched using a scanning simulation, a simple example of which is given in Figure 2.2. Each of these routes is allocated a weighting according to the Boltzmann factor (e^{-E/k_BT}) of the nearest neighbour interaction energies it induces. These interaction energies can either occur between two polymer segments (ϵ_{PP}) or between a polymer segment and solvent (ϵ_{PS}). For simplicity, an implicit solvent is used, which occupies all lattice sites not taken up by polymer segments, so all solvent-solvent interactions are assumed to be zero. $P_j(f)$ can then be calculated as the ratio between the sum of the weightings for the routes that place step j in its correct position, and the sum of the weightings for all possible routes.

Once the probabilities P_j for placing all of the segments in their specified positions have been calculated, they are multiplied together to give the confor-

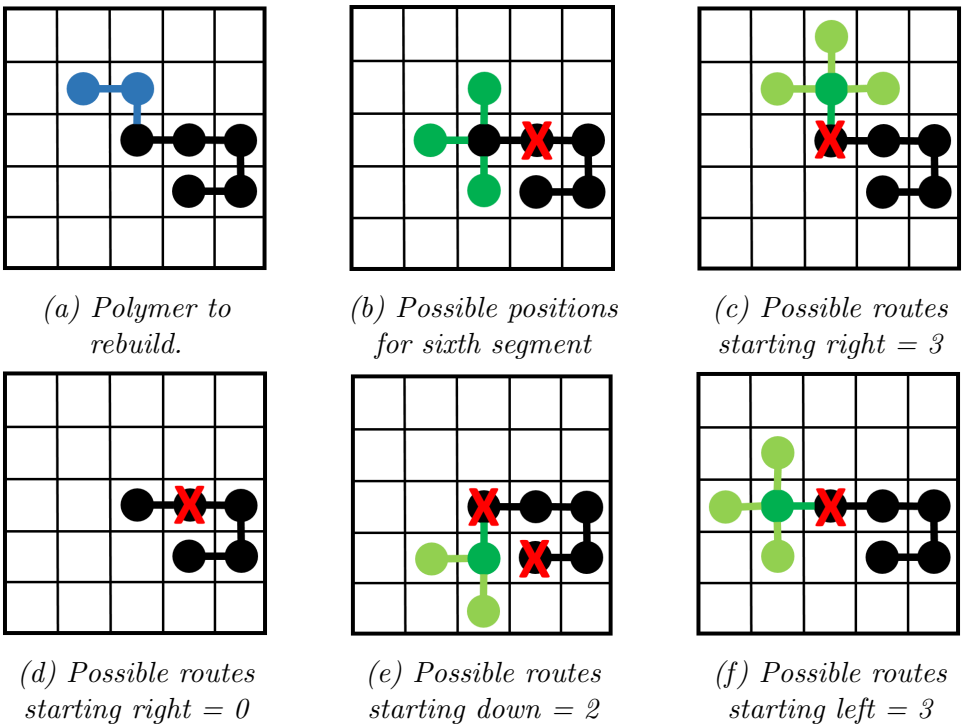

(a) Polymer to rebuild. *(b) Possible positions for sixth segment* *(c) Possible routes starting right = 3*

(d) Possible routes starting right = 0 *(e) Possible routes starting down = 2* *(f) Possible routes starting left = 3*

Figure 2.2: Simple example of the hypothetical scanning methodology in 2D. (a) shows the polymer being rebuilt, where the probability of placing the sixth polymer segment in its specified direction (up), is being calculated. The previous five segments (shown in black) are frozen in space, and we are interested in calculating the number of possible self-avoiding routes for the next $f = 2$ segments. (b) shows the three possible positions for placing the sixth segment. (c), (d), (e) and (f) show all of the possible positions for the seventh segment in light green, starting from each direction of the sixth segment (dark green). Positions for the chain that result in overlaps and are therefore not self-avoiding are shown as red crosses.

mational entropy of the polymer $P_i(f) = \prod_j P_j(f)$.

The value of f is restricted by computational efficiency to around 10, so for polymers with many more segments than this, an error is incurred by not searching all the possible states. Ways to mitigate this include adding a mean-field parameter to account for the rest of the chain,[155] or using a Monte Carlo simulation to estimate P_j instead of numerical counting methods.[149].

An additional step in the calculations for $P_i(f)$ that is necessary for branched

polymers, and new to this work, is the requirement to account for indistinguishable polymer conformations. When scanning the possible routes for the polymer chains, each segment is treated as distinguishable, so that two conformations which look exactly the same but have differently-labelled segments in each position are counted separately. However, in reality, polymers are made up of repeating monomer units, so their constituent segments are generally identical to each other. This leads to an over-counting of the number of possible conformational states for the polymer, and a corresponding underestimation of $P_i(f)$.

In order to account for this and obtain the true $P_i(f)$, the values for $P_i(f)$ initially calculated using the HS method should be multiplied by the number of ways the polymer architecture could be assembled. As we start the HS simulations from a specified segment of the polymer (usually one of the ends), we need to divide by the number of equivalent starting sites. In linear polymers, this number is always two, because there are two ends to every chain. For branched polymers, the number varies with both architecture and the chosen starting point.

This is the only step required for linear polymers, but for branched polymers, there may also be indistinguishablilty caused by having two or more side-branches of the same size and shape emanating from the same segment. In this case, it is necessary to multiply $P_i(f)$ by the number of ways they could be labelled, namely $x!$ where x is the number of indistinguishable side-branches. This step should be repeated for every occasion where indistinguishable side-branches are experienced when moving along the polymer from the starting position.

An example of these calculations can be seen in Figure 2.3. Although the chosen starting point determines the balance between starting position indistinguishability and side-branch indistinguishability, the overall value that $P_i(f)$ must be multiplied by is independent of starting position for each polymer architecture.

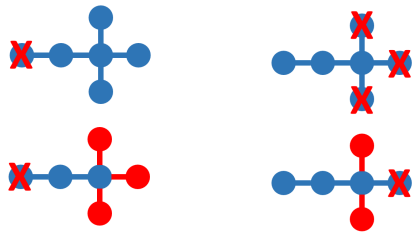

(a)
$P_i(f) \rightarrow P_i'(f) \cdot 1 \cdot 3! = 6P_i(f)$

(b)
$P_i(f) \rightarrow P_i'(f) \cdot 3 \cdot 2! = 6P_i(f)$

Figure 2.3: Indistinguishability calculations for an example branched polymer with six segments. Equivalent starting segments are shown as red crosses, and identical side-branches are highlighted in red. In (a), the starting position is taken as the left hand end of the polymer, which has no other equivalent segments. However, there are 3 identical side-branches along the chain, so $P_i(f)$ must be multiplied by $3! = 6$. If the starting position is taken as any of the other ends, as in (b), $P_i(f)$ must be multiplied by 3 to account for their equivalence. Two identical side branches are then encountered, so $P_i(f)$ must be divided again by $2! = 2$.

In addition to calculating $P_i(f)$, the total energy for each conformation in the Boltzmann-distributed ensemble (E_i) should also be determined to allow calculations of thermodynamic variables. E_i is simply the sum of all the polymer-polymer and polymer-solvent nearest neighbour interaction energies incurred along the chain.

2.2.3 Entropy and free energy calculations

Once the probabilities for each conformation in the Boltzmann distributed ensemble ($P_i(f)$) have been determined using the hypothetical scanning methodology, the values of energy, entropy and free energy can then be calculated by averaging over all of the n conformations in the ensemble. Since we only have approximate values ($P_i(f)$) rather than the exact values (P_i^B), the resulting calculations will also be inexact. Therefore, two calculations will be carried out for each of the thermodynamic variables, one of which can be shown to underestimate the

correct values, and one to overestimate them.

In the first set of calculations, the first occurrence of P_i^B in Equation 2.5 (which refers to the probability of finding the polymer in the ensemble) is taken to be equal for all polymers in the ensemble, so $P_i^B \rightarrow 1/n$, where n is the ensemble size. The second occurrence of P_i^B (which refers to the probability of constructing each polymer) is estimated using the $P_i(f)$ values calculated from the HS simulation. The resulting expressions for energy (E^A), entropy (S^A) and free energy (F^A) are given by Equations 2.7, 2.8 and 2.9 respectively. S^A provides a rigorous upper bound for the true entropy, and E^A and F^A provide rigorous lower bounds for the true energy and free energy.[158,159]

$$E^A = \frac{1}{n}\sum_{i=1}^{n} E_i \tag{2.7}$$

$$S^A = -\frac{k_B}{n}\sum_{i=1}^{n} \ln P_i(f) \tag{2.8}$$

$$F^A = \frac{1}{n}\sum_{i=1}^{n}\left[E_i + k_B T \sum_{i=1}^{n} \ln P_i(f)\right] \tag{2.9}$$

In the second set of calculations, the probability of finding the polymer in the ensemble is approximated by the normalised value of $P_i(f)/\sum_{i=1}^{n} P_i(f)$. The resulting expressions for the energy (E^B), entropy (S^B) and free energy (F^B) are given by Equations 2.10, 2.11 and 2.12.[149,157–159] These values are not rigorous bounds for the true energy, entropy and free energy, although it is always true that $E^B > E^A$, $S^B < S^A$ and $F^B > F^A$. S^B, E^B and F^B are usually found to also underestimate the true entropy and overestimate the true energy and free energy respectively when compared to other calculation methods such as direct Monte Carlo.[157,160]

$$E^B = \frac{\sum_{i=1}^{n} P_i(f) E_i}{\sum_{i=1}^{n} P_i(f)} \tag{2.10}$$

$$S^B = -k_B \frac{\sum_{i=1}^{n} P_i(f) \ln P_i(f)}{\sum_{i=1}^{n} P_i(f)} \tag{2.11}$$

$$F^B = \frac{\sum_{i=1}^{n} P_i(f)[E_i + k_B T \ln P_i(f)]}{\sum_{i=1}^{n} P_i(f)} \tag{2.12}$$

Therefore, the most accurate estimates of the true expectation values of the thermodynamic variables can be found by taking the arithmetic mean of the two approximations, as the true value will most likely lie somewhere in the middle. These means will be denoted E^M, S^M and F^M

2.2.4 Creating a sample ensemble of branched polymers

In order for correct free energy values to be obtained, an average must be taken over an ensemble of systems arranged according to the Boltzmann distribution, as this best represents the real distribution of states. The best way to do this is to initially arrange the polymers on lattices in any position (for example with the backbone placed in a straight line), and then equilibrate using a Metropolis Monte Carlo method (see Section 1.4.4).

A range of different Monte Carlo moves for self-avoiding walks are available in the literature, each with advantages and disadvantages[109] Some commonly used options are reptation, corner flips, crankshafts, and pivots, shown in Figure 2.4.

Unfortunately, choosing a suitable algorithm that worked effectively for branched polymers without breaking or altering the connectivity of the bonds proved difficult. The only technique found to work was an adapted version of the pivot algorithm.[161] Here, a segment along the polymer is chosen at random, and a symmetry operation (e.g. a rotation or reflection) is applied to all subsequent segments. A schematic of this is shown in Figure 2.4d. In the case of branched polymers, only segments located on the same branch as the chosen segment were moved during each pivot operation.

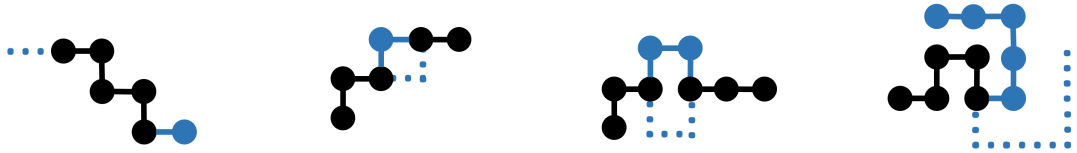

(a) Reptation *(b) Corner flip* *(c) Crankshaft* *(d) Pivot*

Figure 2.4: Examples of Monte Carlo algorithms available to linear self-avoiding walks. Sections of polymer held steady during the moves are shown in black, new segment positions in blue, and old segment positions as a blue dashed line. The only technique found to maintain connectivity in the case of branched self-avoiding trees is the pivot move.

2.3 Results and discussion

In order to produce reliable results for entropy and free energy, a large ensemble of Boltzmann distributed systems had to be produced and measured. To reduce the computational time required, parallel programming using a CUDA supported graphics processing unit (GPU) was employed, where repeats were run in separate processing threads. The Tesla K40c GPU used for this work allowed 15 360 threads to run simultaneously, so 16 batches were performed to achieve a total of 245 760 repeats for each simulation.

To create the initial distribution of states, 15 360 copies of the chosen polymer were placed onto separate lattices with their backbones lying along the x-axes. Monte Carlo pivot moves were then carried out on each polymer to equilibrate with the energetic interaction parameters. One end of each polymer was tethered to the lattice origin. The conformations of the polymers were then recorded 16 times, with a large number of equilibration steps in between each sampling to avoid correlations. For the samples in 3D, $1000N$ initial equilibration pivot moves were attempted, and a further $100N$ moves between each sampling, where N was the number of bonds between segments in the polymer being tested. In 2D, a

lower percentage of the pivot moves were successful due to higher excluded volume, so twice as many pivot moves were attempted, with $2000N$ during the initial equilibration, and $200N$ between each sampling. These values produced comparable distributions to ensembles that had been simulated for 10 times as many steps, so were deemed to provide sufficient equilibration for the small molecules used here. Longer run times may be required to fully equilibrate larger polymers.

Hypothetical scanning simulations were then carried out on each of the repeats. The possible positions of the next eight segments were considered when calculating the probabilities for placing the current segment in its specified position ($f = 8$). As all of the polymers used during this work were small, this meant these calculations were exact, and that the only errors arose from the reliability of producing the Boltzmann distributed ensemble, and from the assumptions of the shape of this distribution made while deriving Equations 2.7 to 2.12. Calculated values for the entropy of linear polymers were found to be consistent to at least 10 significant figures with accepted literature values via enumeration methods for all lengths of polymer studied.[162,163]

Calculations were carried out for all possible architectures of polymers up to nine segments in size, with the maximum functionality of each segment limited only by the number of nearest neighbour sites available on the lattice, to four in 2D (simple square) and six in 3D (simple cubic). As each segment represents a Kuhn length of polymer which may contain many reactive groups, this condition is physically feasible.

The size of the polymers studied here, although very small compared to fully reacted epoxy resin thermosets, is nevertheless of interest to aerospace resins, where much of the phase behaviour of the blends is observed to take place during the early stages of cure.[62] The methodology developed is applicable to polymers of arbitrary size, dependent only on computational power. As an example, using

the methodology and equipment described above, the full simulation for single polymer architecture containing 50 Kuhn segments was found to take approximately three days.

The number of possible polymer architectures increases very quickly with size, so only polymers with up to seven segments will be shown here for the sake of clarity. This will allow the main trends to be observed without becoming hindered by a large amount of data.

2.3.1 Entropy of branched polymers

The main case that will be studied here is a purely entropic system with no energetic interactions. This is relevant to aerospace resins, where all constituent polymers have relatively similar chemistries. This means there are roughly equivalent energetic interactions between the different types of segments, which cancel out to leave a system mostly governed by entropy.

Energetic interactions between polymer segments are also notoriously difficult to determine, as they require in-depth calculations of all the atomic interactions between two segments, each of which depends on the relevant separation distance. Segment interactions can also be estimated from cohesive energy densities, which determine intermolecular interactions by measuring the amount of energy required to completely separate molecules into an ideal gas state, but this method requires accurate vapour pressure data and lengthy calculations.[164] The interaction potentials of the segments also depend on their local environments, so vary with the position of the segments within the molecule and the amount of polymerisation that has taken place.

Therefore, the work here focussed mostly on entropy, in order to avoid the use of inaccurate energy parameters. The calculated entropies for all possible

architectures of polymers between four and seven segments in size are shown in Figure 2.5, for both 2D and 3D lattices. Results are given as entropy per molecule in units of k_B.

It is clear that this method is able to show significant differences between the entropies of polymers with different architectures, whereas classical models such as Flory-Huggins would predict the same value for all polymers with an equal number of segments. As intuitively expected, a higher prevalence of branching points generally reduces entropy. This is because there are fewer ways to organise branches around a central segment with higher functionality, due to the possible positions for each new segment being restricted by the excluded volume of the segments that have already been placed. In general, it can be observed from Figure 2.5 that the presence of higher functionality branching points causes a larger reduction in entropy than multiple lower functionality branching points.

There are some exceptions to these trends due to molecular symmetry, examples of which can be found in the calculated entropies of polymers with seven segments, shown in Figure 2.5d. The first polymer on the left has a single trifunctional branching point placed such that none of the branches are equivalent, and this actually has higher entropy than a linear polymer of the same size. This is due to the indistinguishability effects discussed at the end of Section 2.2.2: the two ends of the linear polymer are identical, so the number of distinguishable microstates is lower than for the architecture where no segments are placed equivalently. This effect is large enough to overcome the reduced choice of ways to place segments on the lattice in the branched molecule, so the entropy of the linear polymer is ultimately lower. There are a few other trend-breaking orderings evident in Figure 2.5d, all of which are also a result of the number of indistinguishable symmetries.

Another factor that can influence the entropy, although to a lesser extent than

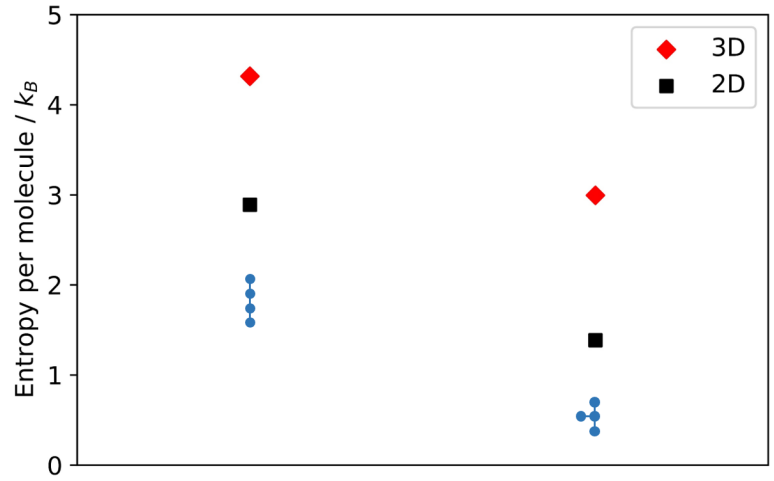

(a) 4 segments

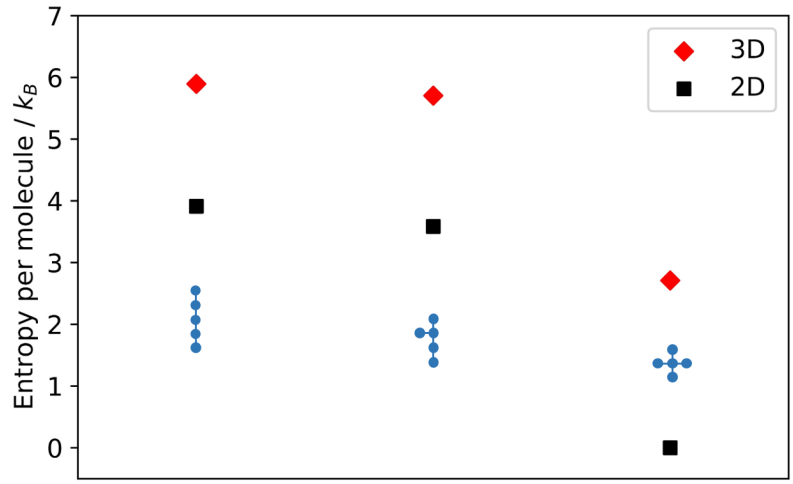

(b) 5 segments

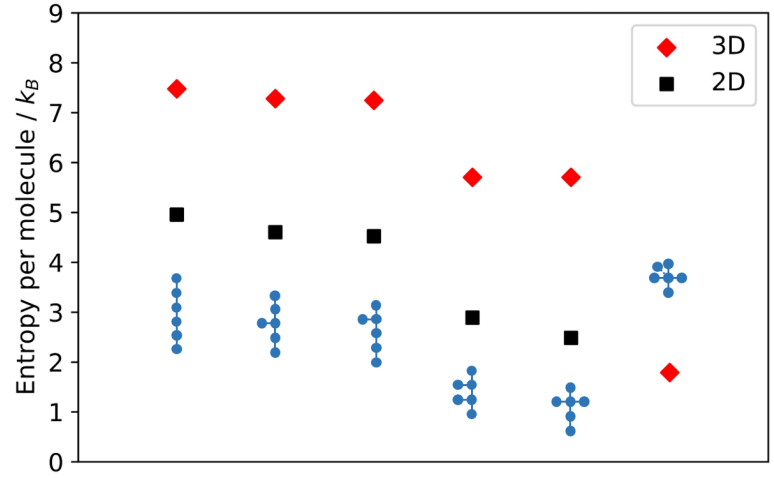

(c) 6 segments

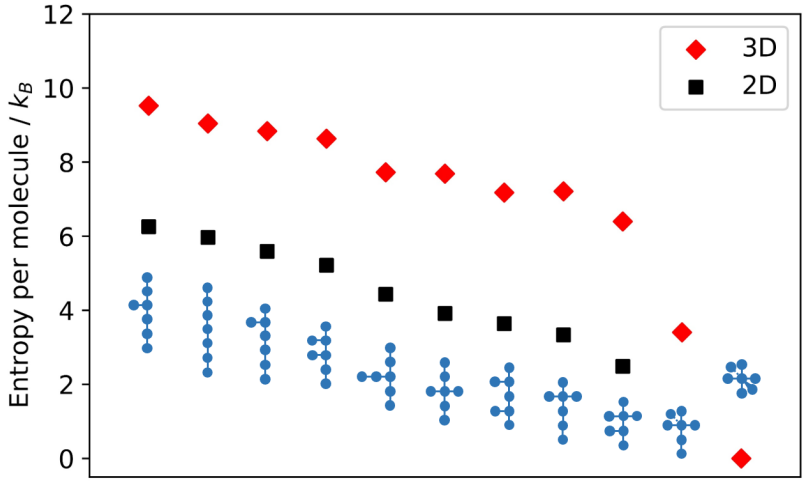

(d) 7 segments

Figure 2.5: Entropy per segment for polymers with all possible architectures and sizes of between four and seven segments.

the other reasons mentioned above, is the ability of the architecture to fold in on itself and produce overlaps. In the self-avoiding model of a polymer that we are using, such intersections are forbidden. This means that geometries capable of overlapping have fewer permitted conformations, and correspondingly lower entropies. An example of this is the difference between the polymers with the second and third highest entropies for six segments in Figure 2.5c. These each have one trifunctional branching point, and equal amounts of indistinguishability. However, as shown in Figure 2.6, the architecture with the branching point close to one end of the backbone has more propensity to intersect than the one with the branching point in the centre. This causes the former to have slightly lower entropy.

The entropy is higher for all polymers on 3D lattices than 2D lattices, as a result of the increased degrees of freedom and lower excluded volume. In general, the values are approximately one and a half times higher in 3D, because there are six neighbouring sites from which to choose segment positions on a cubic lattice, compared to four on a square lattice. The impact of branching is greater

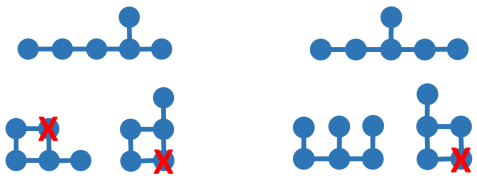

(a) (b)

Figure 2.6: Schematic of two polymers with six segments and equivalent amounts of branching. Each of the two polymers are shown in their most open and most folded conformations. The architecture in (a) has the propensity to intersect when folded in either direction, but (b) is only geometrically capably of intersecting when folded downwards, and not upwards.

in 2D than 3D, resulting in larger differences in entropy between the different architectures. This is because the reduced degrees of freedom mean that there is a more severe restriction on the number of ways to place segments around branching points. This suggests that lattice symmetry in general will affect the quantitative values for entropy, with a greater coordination number resulting in higher entropy, but trends within a series of molecules would be expected to remain consistent.

2.3.2 Entropy changes during polymerisation

Intuitively, and in traditional theories such as the Flory-Huggins model, the entropy of a molecule increases with polymerisation, because an increased number of segments generally leads to more degrees of freedom. However, the hypothetical scanning model demonstrates that this is not always true of branched molecules. Figure 2.7 shows all the possible geometric ways a polymer of x segments can be polymerised to a molecule of $x + 1$ segments (where here x ranges from 3 to 6), along with the corresponding entropies for each molecule.

In most cases, the entropy per molecule increases during polymerisation, as expected. However, there are a few examples where a counter-intuitive decrease

is observed, due to increased symmetry of the larger, polymerised molecule compared to the smaller, unpolymerised one. This effect is more prevalent in 2D than 3D, because the variation between the entropies of different architectures is already more pronounced, as mentioned above. These deviations from the usual trend during polymerisation suggest that a mean-field model based on linear polymers may not be sufficiently detailed to accurately predict the behaviour of branched molecules.

2.3.3 Free energy of linear polymers

Another limitation of the Flory-Huggins model mentioned in Section 2.1 is that it treats entropy and energy individually according to separate mean-field theories, and ignores any interplay between the two. The hypothetical scanning model includes the true local conditions of all the polymer segments during the calculations, so is likely to improve on this shortcoming.

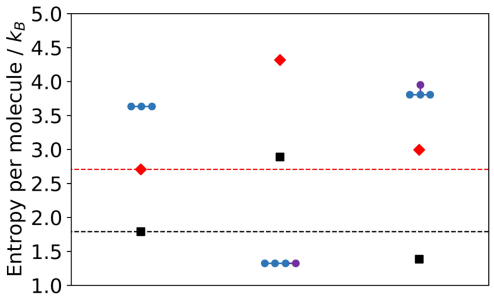

(a) $3 \rightarrow 4$ *segments*

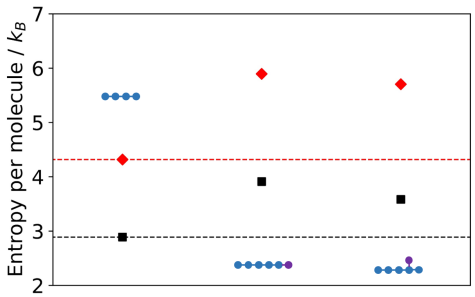

(b) $4 \rightarrow 5$ *segments*

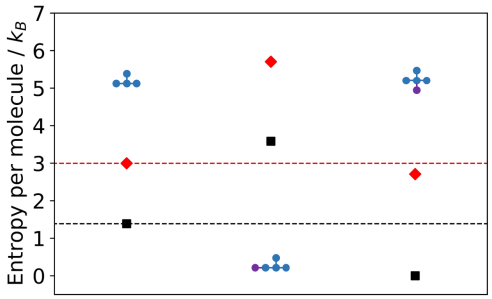

(c) $4 \rightarrow 5$ *segments*

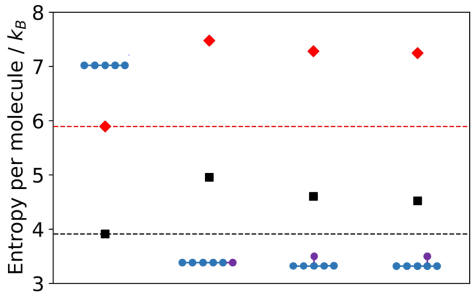

(d) $5 \rightarrow 6$ *segments*

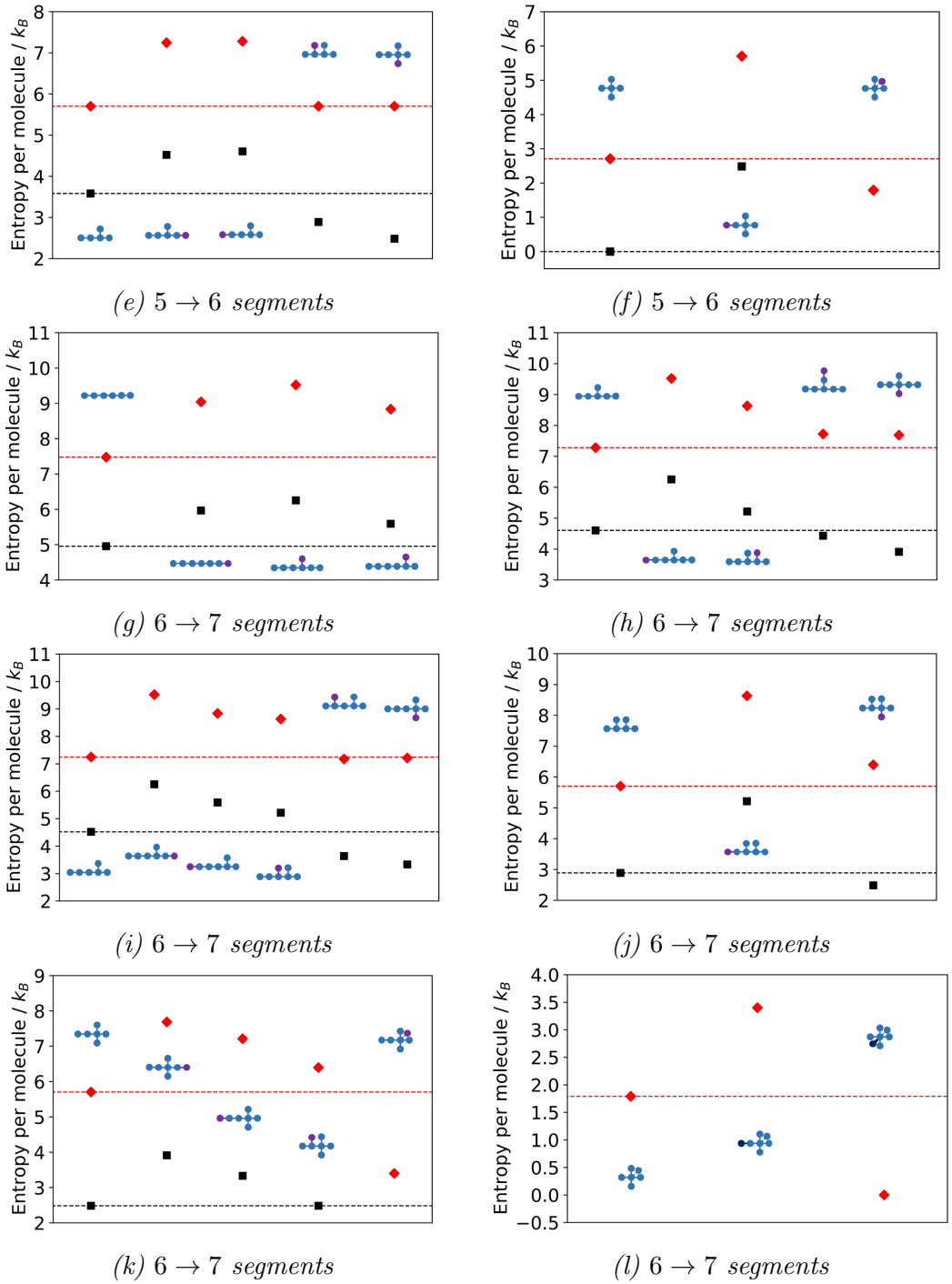

(e) $5 \rightarrow 6$ *segments*

(f) $5 \rightarrow 6$ *segments*

(g) $6 \rightarrow 7$ *segments*

(h) $6 \rightarrow 7$ *segments*

(i) $6 \rightarrow 7$ *segments*

(j) $6 \rightarrow 7$ *segments*

(k) $6 \rightarrow 7$ *segments*

(l) $6 \rightarrow 7$ *segments*

Figure 2.7: The entropy changes when polymerising a molecule of x segments to $x+1$ segments. All the possible geometric ways to add a single segment to initial molecules with 3, 4, 5 and 6 segments are included. The shapes of each molecule are shown, where the purple represents newly-added segments. The entropy on a 2D square lattice is given by black squares, and the entropy on a 3D cubic lattice is given by red diamonds. The dashed lines show the entropy of the initial molecule before polymerisation.

The free energies for linear polymers of several lengths were calculated using the hypothetical scanning method. The polymer-polymer segment interaction was held at zero, so that the only energetic interactions in the system were between polymer segments and solvent. The value of this ϵ_{PS} interaction was varied between $-5k_BT$ and $5k_BT$. In a mean-field model, energetic interactions would not influence the conformations of the polymer, so a linear trend would be observed between the overall free energy of the polymer and the size of the polymer-solvent segment interaction. The results calculated using the hypothetical scanning method (see Figure 2.8) deviate from this straight line, with the free energy reduced where strong polymer-solvent interactions are experienced.

These deviations from the linear trend indicate the interplay between energy and entropy. When interactions are strong, the polymer conformations are no longer random and become biased towards those with lower overall energy. In the case of repulsive (positive) polymer-solvent interactions, compact conformations are favoured, and when polymer-solvent interactions are attractive (negative), stretched, open conformations are more likely.

This has two competing effects on the overall free energy. The dominating effect is the expected reduction in the average energy of each polymer. There is also a small decrease in entropy due to there being fewer possible microstates for polymers with preferentially compact or stretched conformations than with entirely random conformations. However, as energy dominates, the average free energy per molecule drops compared to the mean-field predictions.

The effect is larger for longer chains, because there is more flexibility over conformation, so any biases are correspondingly stronger. Bearing in mind that the polymers studied here are extremely small, with a maximum of seven Kuhn segments, this suggests that traditional methods used to predict free energy are likely to be inaccurate in the presence of strong energetic interactions, even for

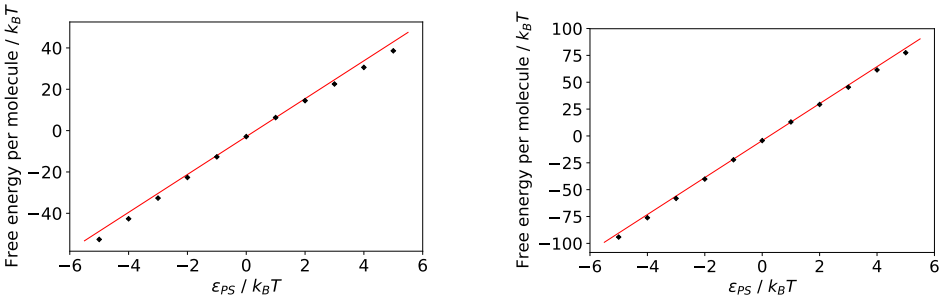

(a) 4 segments, 2D

(b) 4 segments, 3D

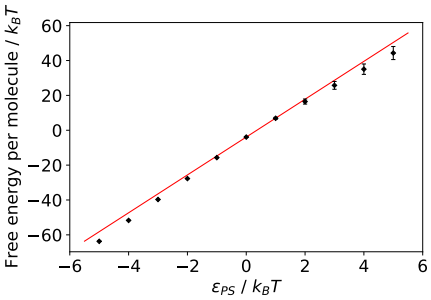

(c) 5 segments, 2D

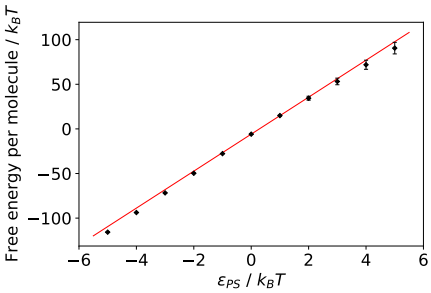

(d) 5 segments, 3D

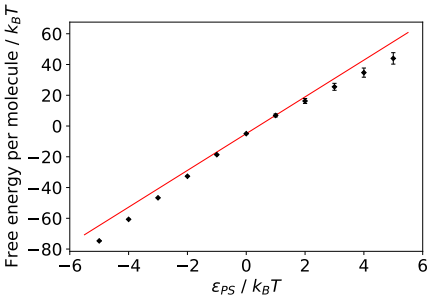

(e) 6 segments, 2D

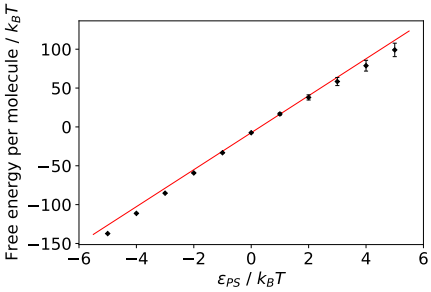

(f) 6 segments, 3D

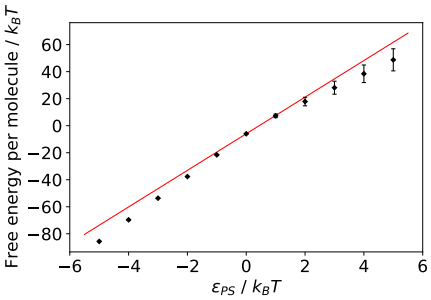

(g) 7 segments, 2D

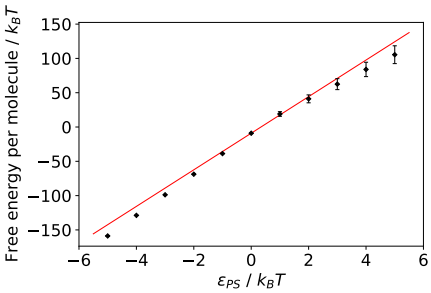

(h) 7 segments, 3D

Figure 2.8: Free energies calculated for linear polymers of various lengths using the hypothetical scanning method, in both 2D and 3D. The polymer-polymer segment interaction was held at zero, and the polymer-solvent interaction (ϵ_{PS}) was varied between $-5k_BT$ and $5k_BT$. Calculated values of F^M are shown in black, with error bars representing the lower and upper bounds of the free energy, F^A and F^B. The linear trends between the overall free energy and the size of the polymer-solvent interaction predicted by mean-field models are shown in red.

linear polymers.

More pronounced deviation is observed for polymers on 2D square lattices than on 3D cubic ones. In 2D, the entropy of the polymer chains is already small in comparison to 3D due to the reduced degrees of freedom. Therefore, biasing the distribution of conformations towards energetically favourable ones causes a smaller decrease in entropy than in the 3D case. This means there is less competition against the reduction in energy from having more favourable conformations, even though this is also smaller. The decrease in free energy is therefore larger, resulting in more deviation from the mean-field predictions.

2.4 Conclusions and further work

In this chapter, the hypothetical scanning method [155,156] was adapted to provide calculations for the entropy and free energy of branched polymers. Results for small branched molecules of up to seven segments were presented here, but the methodology can be extended to polymers of arbitrary shape and size.

The entropies of branched polymers were shown to vary with architecture; more symmetrical molecules with higher branching had lower entropies. Although the trends were generally intuitive, these calculations allowed the differences to be quantified, and small effects to be discerned.

It was also observed that in the case of branched molecules, polymerisation sometimes led to a decrease in the entropy per molecule, as opposed to the increase always experienced with linear polymers. This implies that models based on linear polymers do not always well represent branched ones, and may not predict the correct trends.

Lastly, we saw that the hypothetical scanning method indicates deviation

from the mean-field free energy calculations, as a result of including the local conditions of the polymer segments in the model. This allowed the conformations of the polymer segments to become biased towards those with favourable interaction energies, and caused a significant decrease in the free energy when these interactions were strong.

This methodology is currently only valid for single polymers in implicit solvent, and does not consider interactions with other polymers on the same lattice. This means that it cannot yet be used to calculate free energies of mixing, which relate to how well molecules pack together when mixed compared to demixed. In order to rectify this shortcoming, multiple molecules would have to be placed onto the same lattice, and the entropy or free energy for each polymer calculated with consideration of the positions of the other polymers. This has previously been carried out in the literature for the entropies of linear molecules with moderate densities of up to 0.63 total volume fraction.[165,166]

A major problem with this method in the case of branched polymers is the difficulty associated with finding a Monte Carlo algorithm that allows a Boltzmann distribution to be produced ready for the free energy calculations. The only common algorithm for self-avoiding walks that could be adapted to the branched case is the pivot algorithm, as the other techniques in the literature do not allow molecular architectures to be maintained around branching points. Unfortunately, the pivot algorithm is not suitable for simulating multiple polymers on the same lattice, as it does not provide a mechanism for molecules to easily translate across the lattice. Therefore, the initial distribution of polymer positions cannot be equilibrated effectively. It also performs poorly in dense systems because it attempts to produce large changes in a single move, and most of these are not accepted in a dense system with high excluded volume. Therefore, the system becomes stuck in a non-equilibrium state, and will not give accurate results.

Methods to simulate linear polymers in dense systems are numerous,[167–170] but as the algorithms all involve cutting the molecules and swapping sections with other molecules or other parts of the same molecule, they would break the connectivity within branched architectures.

Therefore, it is preferable to use a calculation method for the free energy that does not require equilibration to a Boltzmann distribution via Monte Carlo moves. A potential option is the scanning method[165] which directly calculates the entropy and free energy using a construction procedure. The probabilities for placing each segment of the polymer are calculated by scanning the possible locations for the next f segments, and counting the percentage of these that start in each neighbouring site to the current segment. A position for the next segment is then chosen randomly, with probabilities biased by these values. The probability of creating the whole polymer chain ($P_i(f)$) is then the product of the probabilities for placing each constituent segment in its chosen position. The drawback of this method is a high attrition rate, because positions can be chosen for polymer segments that do not geometrically allow the rest of the polymer to fit onto the lattice. This would reduce the efficiency of the simulation, meaning that the density of the system would be limited and less interaction between different molecules would be experienced than in an equivalent real system. However, this method remains a viable option and will likely form the next part of the work.

Chapter 3

Monte Carlo modelling of concentration fluctuations

3.1 Introduction

In the previous chapter, a method for calculating entropy and free energy of infinitely dilute solutions of branched polymers was developed. However, this cannot yet provide the free energy of mixing, and does not provide the whole picture because it neglects the interactions between polymers that would be present in industrially relevant blends.

Therefore, it is important to also study systems with higher polymer concentrations. We saw in Section 2.4 that the previously discussed Monte Carlo methods for the simple cubic model with one polymer segment per lattice site cannot be used for dense systems containing branched polymers. Instead, a technique called the bond fluctuation model (BFM) can be employed, which will be described in detail in Section 3.2.1.[171] Due to the large number of potential nearest neighbour bonding sites available (108 rather than 6 for the simple cu-

bic model), the BFM would be extremely inefficient for the type of free energy calculations detailed in Chapter 2, but it can be used to study inhomogeneities within a blend via variations in the local concentrations of each component.

Limits on computational efficiency severely restrict the size of lattice that can be simulated, even when using a course-grained model where each monomer or Kuhn segment of polymer is represented as one simulation bead. A widely-used trick to combat this is to use periodic boundary conditions (PBCs), where any material that leaves one side of the simulation box immediately re-enters from the opposite side. This method allows the properties of the bulk material to be investigated, whereas if PBCs are not used, the boundaries of the simulation box represent the edges of the material, and only surface effects can be investigated.

Even when using a small simulation box, PBCs are very effective for studying properties that depend mainly on short range interactions between particles in the simulation, such as energy, diffusion and conductivity. However, they cannot be used to accurately calculate properties where long range interactions are important, due to correlations between particles in the main simulation box and their images in the neighbouring boxes. Therefore, phase transitions, which involve large-scale restructuring of the material, cannot be investigated unless a large simulation box is used.

Therefore, to prevent excessively long simulation times, the work in this chapter will focus on modelling concentration fluctuations, which are the precursor for phase separation, rather than simulating the phase behaviour directly. As described in Section 1.2.4.2, concentration fluctuations become larger and more pronounced as miscible blends approach the spinodal and become closer to phase separating. Therefore, by comparing differences in concentration fluctuations between systems, an indication of their relative stability can be obtained.

The aim of this work was to develop a computational methodology that would

allow concentration fluctuations to be studied in blends of linear and branched polymers. This would mean that in the future, with appropriate characterisation and calibration with neutron scattering data, information about morphological properties and phase separation behaviour could be gained for industrially-relevant aerospace polymer blends with fewer expensive and time-consuming experiments.

3.2 Background theory

In this section, the background theory required to understand the simulations used during this part of the work will be described. The general Monte Carlo algorithm, the specific usage of it in this work, and the methods employed to calculate system properties will be covered.

3.2.1 The bond fluctuation model

The bond fluctuation model (BFM) is a dynamic Monte Carlo algorithm developed in 1988 by Carmesin and Kremer.[171] It has seen wide-spread use for simulating various features of polymer systems such as glass transitions[172–174], phase behaviour[175], chain dynamics,[176] and structural properties that change with chemical reaction.[177]

The BFM uses a simple cubic lattice, where each polymer segment occupies a unit cube of eight lattice sites instead of the single site used for Flory-Huggins type models. Neighbouring chain segments are connected by one of 108 different bond vectors, which are composed of all the permutations and sign inversions of the following six vector families: $P_{\pm}(2,0,0) \cup P_{\pm}(2,1,0) \cup P_{\pm}(2,1,1) \cup P_{\pm}(2,2,1) \cup P_{\pm}(3,0,0) \cup P_{\pm}(3,1,0)$. Resulting bond lengths can vary between 2, $\sqrt{5}$, $\sqrt{6}$,

3 and $\sqrt{10}$ lattice units. The intermediate bond vector $P_{\pm}(2,2,0)$, of length $\sqrt{8}$ lattice units is not permitted, as this positioning lets other segments pass through the gap between the bonded ones, allowing chain intersections (which should be prohibited in self-avoiding models of polymers) to occur.[171,175]

The BFM algorithm is carried out as follows. A segment is selected at random and an attempt is made to move it by one lattice site in any of the six nearest neighbour directions (see Figure 3.1). If none of the lattice sites required by the new position of the segment are already occupied, and all bond vectors remain within the families specified above, the move is carried out according to normal Metropolis Monte Carlo acceptance rules (see Section 1.4.4). Otherwise, the move is rejected and the segment position remains unchanged.[171,175]

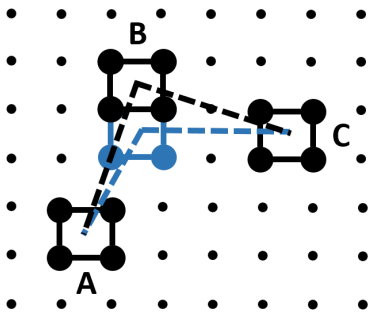

Figure 3.1: Schematic of the bond fluctuation model for a simple molecule of three segments A, B and C. Dashed lines represent bond vectors between segments. An attempted Monte Carlo move of segment B is shown, from the blue to the black position. None of the newly-used lattice sites are already occupied, so the move is self-avoiding. The bond vector between segments A and B changes from (1,2,0) and (1,3,0), and the bond vector between segments B and C changes from (3,0,0) to (3,-1,0). Both these new bond vectors are within the permitted set, so the move will be accepted according to normal Metropolis Monte Carlo rules.

The bond fluctuation model is well designed for studying phase behaviour in blends containing branched molecules. In 3D, the model maintains ergodicity (see Section 1.4.5) and bond connectivity for both branched and linear molecules.

Note that in 2D, reorganisation of multiple bonds originating from the same segment is impossible, so the BFM is only ergodic in 3D for branched molecules. The high number of 108 possible bond vectors and 87 possible bond angles in the BFM also allows more flexibility than in the set-up used in Chapter 2, so higher density systems can be studied. In addition, none of the attempted moves are unphysical, so dynamic properties such as diffusion coefficients can be studied as well as static properties.[171]

3.2.2 Model design

In this work, the 3D bond fluctuation model was used to simulate concentration fluctuations in blends of linear thermoplastic and branched theromosetting polymers.

Due to difficulties associated with laying branched molecules onto lattices without overlap, the branched components were inserted as monomer units which were then reacted *in situ*. Strictly speaking, including irreversible bonding reactions in Monte Carlo simulations is mathematically invalid due to a lack of equilibrium and detailed balance (see Section 1.4.6), but there is prior usage in the literature.[177] Unfortunately, the reactive canonical Monte Carlo methodology[179] cannot be used, as it relies on equilibrium with a reverse reaction which is not present when curing thermosets. In any case, as long as the bonding simulations are only used to populate the lattice with the desired molecules and not for any property calculations, their usage is acceptable, although the resulting molecular shapes and size distributions may not accurately represent those that would be present in equivalent experimental systems.

To set up the simulations used in this chapter, chains of linear thermoplastic molecules were placed onto a cubic lattice with a side length of L lattice units in a snake-like, end-to-end fashion. Segments were spaced by bond vectors

of $P_{\pm}(2,0,0)$ to comply with the restrictions of the BFM. Single unconnected segments representing epoxy monomers and amine curative molecules were then placed in the same manner, following on from the thermoplastic molecules.

The system was then allowed to equilibrate using the BFM algorithm. In order to reduce equilibration times, systems should first be equilibrated without energetic interactions (equivalent to an infinite temperature regime) to mix the molecules effectively on the lattice, then the temperature may be reduced and a further equilibration carried out with the desired energetic interactions between segments switched on as required. Due to time constraints, all systems used during this chapter were initially equilibrated and reacted without the presence of energetic interactions, which were only switched on after the bonding simulation was complete.

Once equilibration had been carried out, the bonding simulation was run. Each segment was allocated a maximum functionality to restrict the amount of bonds it could form. All thermoplastic segments were assumed to be unreactive. Difunctional epoxy molecules were allowed to form a maximum of two bonds and tetrafunctional diamine curatives a maximum of four bonds. Epoxy molecules were only allowed to react with amines and vice versa. To ensure ergodicity in the resulting cured system, no cyclical bonds were allowed to form. Optionally, an upper limit on the size of each molecule could also be enforced, but that was not deemed necessary here as the resulting molecules remained relatively small anyway.

During the bonding simulations, the BFM algorithm was performed as normal, but the possibility of a bonding reaction was also included with a certain probability. During an attempted bonding step, an epoxy and amine segment were chosen at random, and if the distance between them was within the allowed set of bond vectors and both molecules had remaining functionality, they were

reacted with a chosen probability. Reaction probabilities could be varied with the number of bonds already formed by the chosen amine segment (to represent steric hindrance), but were all assumed to be equal to one here. Theoretically, interaction energies and bonding probabilities could be altered to match the final molecular weight distributions to those measured by experiment.

Once the bonding simulations were complete, the systems were then equilibrated using the normal BFM algorithm, including the desired energetic interactions between the segments, so that the morphological properties could be investigated.

In order to investigate differences between systems at various stages of cure, the amount of amine segments added to the lattice was limited to well below that required to give a stoichiometric full reaction. By varying the amount of amine molecules and reacting until all possible amine bonds had formed, the extent of cure and molecular weight distribution could be controlled. Any unreacted epoxy molecules remained as single segments. Due to the functionalities of the chosen epoxy and amine, a 2:1 ratio of epoxy to amine segments would allow a full reaction of 100 % cure extent. Ratios of 40:1, 20:1 and 10:1 were used during these simulations, with final cure extents of 5 %, 10 % and 20 % respectively. The cure extent was kept low in order to maintain ergodicity and prevent the formation of molecules large in size compared to the simulation box, which would introduce correlations by interacting with their images in neighbouring simulation cells. Investigating properties at low cure extent is also valuable when studying aerospace resins, as much phase separation often happens during the early stages of the cure cycle.[62]

3.2.3 Calculating system properties

Although entropy and free energy cannot be measured efficiently using the BFM, several other properties can be calculated that give an indication of the phase behaviour.

3.2.3.1 Total energy

The total interaction energy in the system can be calculated by summing over all nearest neighbour segment interactions, where each type of component pair is allocated a different energy. In this work, three types of neighbour interactions energies are allocated: epoxy-epoxy (ϵ_{EE}), epoxy-thermoplastic (ϵ_{ET}) and thermoplastic-thermoplastic (ϵ_{TT}). To simplify the model, all segments of the same type were allocated the same interaction energies, even though in reality their properties would depend slightly on their positioning within a molecule. Amine curative segments were assumed to interact similarly to epoxy segments.

The interaction energies may be designed to decrease with increasing distance between segments by using a Lennard-Jones potential[172], or tuned to favour particular bond lengths to study glass formation[173] or account for structural constraints.[174] However, a simpler step potential can also be used. Here, all segments within a certain distance of each other are allocated a constant interaction energy (dependent on the type of segments involved), and all interactions outside of this distance contribute zero energy. In addition to being computationally cheaper, this method is also analogous to the nearest neighbour interactions used in the Flory-Huggins model, which assumes that interactions within a polymer blend die off very quickly with distance.[71] Therefore, for these simulations, a maximum energetic interaction distance of $\sqrt{6}$ was used to correspond to the first shell of neighbouring segments.

For systems of the same size with equivalent volume fractions of each component and equal values for nearest neighbour interactions energies, the difference in total energy depends only the relative proportions of each type of interaction present. Total energy therefore constitutes a measure of the amount of interface between the components, and, correspondingly, the size of the concentration inhomogeneities present.

3.2.3.2 Radius of gyration

In general, the radius of gyration (R_g) of a body is the distance away from the axis of rotation at which all the mass of the body can be assumed to be concentrated in order to give the correct moment of inertia. For polymers, R_g describes the conformational dimensions of the chains, and can be measured by scattering experiments. R_g can be calculated equivalently by Equations 3.1 and 3.2, where $\boldsymbol{r}_i$ and $\boldsymbol{r}_j$ denote the positions of each of the polymer segments, $\boldsymbol{r}_{COM}$ gives the polymer's centre of mass, and N is the number of segments in the polymer.[180] Equation 3.2 is generally used to calculate R_g in simulations, as periodic boundary conditions make it difficult to calculate the centre of mass for molecules that cross the boundaries of the simulation box.[181]

$$R_g^2 = \frac{1}{N}\sum_{i=1}^{N}(\boldsymbol{r}_i - \boldsymbol{r}_{COM})^2 \tag{3.1}$$

$$R_g^2 = \frac{1}{2N^2}\sum_{i=1}^{N}\sum_{j=1}^{N}(\boldsymbol{r}_i - \boldsymbol{r}_j)^2 \tag{3.2}$$

R_g is a particularly appropriate measure of size for branched polymers, because other commonly-used measures such as the average end-to-end distance are undefined for molecules with more than two ends.

The R_g of a polymer gives information about the local environment, as poly-

mers with unfavourable nearest-neighbour interactions tend to form compact conformations with low R_gs in order to minimise the interfacial area, and vice versa. Therefore, polymers in more miscible blends tend to have higher R_gs. At higher temperatures, the importance of energetic interactions reduces, so R_g is also temperature dependent.

3.2.3.3 Radial distribution functions

The radial distribution function, also known as the pair correlation function and abbreviated RDF or $g(r)$, is given by Equation 3.3, where $\rho(r)$ is the radially averaged local density at distance r from a reference particle and ρ is the overall average density of the system.

$$g(r) = \frac{\rho(r)}{\rho} \tag{3.3}$$

$g(r)$ therefore describes how the local density (total density or in terms of the concentration of a particular species) varies with distance from a reference particle, with peaks at distances exhibiting high local concentration (such as coordination shells of well-defined nearest neighbours) and troughs depicting low local concentration.[70]

RDFs are useful for characterising inhomogeneities in blends because, if a separate value of $g(r)$ is calculated for each combination of components, the characteristic sizes of regions containing each component can be determined. Due to the radial averaging process, the final value $g(r)$ is isotropic, which is an appropriate average for phenomena such as concentration fluctuations or spinodal decomposition.

In these simulations, three types of RDF are calculated, with the same breakdown as for the energetic interactions. $g_{EE}(r)$ gives the average concentration

of epoxy segments at distances relative to epoxy reference segments and $g_{TT}(r)$ gives the average concentration of thermoplastic segments at distances relative to thermoplastic reference segments. The interspecies radial distribution function is independent of which species is taken as the reference particle, so only one of $g_{ET}(r) = g_{TE}(r)$ needs to be calculated. As with energy, amine segments are classed as epoxy segments for the sake of simplification.

Computationally, RDFs between two species A and B (where A and B can be identical) are calculated by taking each A particle in turn and summing together all the B particles within a shell of thickness dr at distance r from that A particle. The number of B particles in each shell ($N_{B,r}$) are placed into histogram bins corresponding to distances from the A particle. The values for $g(r)$ at each distance are then calculated according to Equation 3.4.[108]

$$g_{AB}(r) = N_{B,r}\frac{4\pi}{3}\left[(r+dr)^3 - dr^3\right]\frac{L^3}{N_A N_B} \tag{3.4}$$

The $4\pi/3\left[(r+dr)^3 - dr^3\right]$ term denotes the volume of the spherical shell used to count B particles, and N_B/L^3 gives the average density of B particles in the system, where L is the length of one side of a cubic simulation box. The final value of $g(r)$ must be divided by N_A to account for the fact that we carried out calculations over all A particles in order to take an average. For lattice models, the final values of $g(r)$ should also be normalised against the number of lattice points present within each shell. In this work, histogram bins of two lattice units in size were used.

For simulations with periodic boundary conditions, it is important to avoid correlations between the relative positions of particles with their images in neighbouring cells, so, RDFs should only be calculated up to a distance of $L/2$ from the reference particle.

3.2.3.4 Structure factors

Radial distribution functions provide an easy-to-interpret picture of composition variations within the system, but cannot easily be measured experimentally. In order to validate simulation results against results from scattering experiments, the Fourier transform of the pair correlation function ($h(r) = g(r) - 1$) in reciprocal space, known as the static structure factor $S(q)$, should be calculated. This can be derived directly from the particle positions, but is computationally cheaper to calculate from the RDF, as in Equation 3.5, where r_{min} and r_{max} are the minimum and maximum shell distances considered in the RDF computations.[182,183] The values used for wavenumber q are evenly spaced in reciprocal space between $2\pi/r_{max}$ and $2\pi/r_{min}$, using the same total number of q denominations as r denominations.

$$\begin{aligned} S(q) &= 1 + 4\pi\rho \int_0^\infty r\left[g(r) - 1\right] \frac{\sin qr}{q} dr \\ &= 1 + 4\pi \frac{\sqrt{N_A N_B}}{L^3} \sum_{r_{min}}^{r_{max}} r\left[g(r) - 1\right] \frac{\sin qr}{q} dr \end{aligned} \tag{3.5}$$

3.3 Results and discussion

During the work in this chapter, simulations of the type described in Section 3.2.2 were carried out under different conditions. Initial screening tests were run for simulation boxes with side lengths of $L = 64$, $L = 96$ and $L = 128$ lattice units. No significant differences were observed in any of the measured properties between otherwise equivalent systems, so a box size of $L = 64$ was used throughout the rest of the work to reduce computation times.

Simulations were performed on systems with cure extents of 5 %, 10 % and

20 % by limiting the amount of amine curative, as described in Section 3.2.2. The effect of varying the density was also investigated by considering systems with total volume fractions ϕ of 0.7, 0.8 and 0.9, where the ratio between the thermoplastic and epoxy components was held constant at 20 vol.% thermoplastic and 80 vol.% epoxy. Relatively short thermoplastic molecules with chain lengths of 10 segments were used throughout, in order to prevent correlations between molecules with their images in neighbouring simulation boxes.

In systems with volume fractions of $\phi = 0.8$ and $\phi = 0.9$, all simulations were carried out with no energetic interactions, so only entropic effects were considered. In the systems with $\phi = 0.7$, three different energy combinations were used for all cure extents. The zero energy case was tested, with $\epsilon_{EE} = \epsilon_{TT} = \epsilon_{ET} = 0$. A combination with attractive intraspecies and repulsive interspecies interactions was also used ($\epsilon_{EE} = \epsilon_{TT} = -1$, $\epsilon_{ET} = 1$), as well as one with repulsive intraspecies and attractive interspecies interactions ($\epsilon_{EE} = \epsilon_{TT} = 1$, $\epsilon_{ET} = -1$).

Nine repeats of each simulation condition were run, all with separate initial equilibration and bonding simulations, and quoted uncertainties represent the standard deviation between these repeats. In every case, equilibration was carried out until the radial distribution functions and total energies (where relevant) became constant.

3.3.1 Molecular weight distributions

Bonding simulations were carried out to cure the systems before their properties could be investigated. The resulting molecular size distributions were analysed to ensure that valid comparisons could be drawn between the systems. In these simulations, all monomer weights are assumed to be equal to 1 in reduced units, so molecular weight distributions are equivalent to size distributions.

The first step was to test how the molecular weight distribution varied with the length of the bonding simulation. Two ratios between the rate of bonding steps to movement steps were used for a system with 5 % cure and $\phi = 0.7$. The longer simulation had $p_{bonding} = 0.001$, or 0.1 % probability of attempting to bond at each simulation step. The shorter simulation had $p_{bonding} = 0.1$, or 10 % probability of attempting to bond. It is worth noting that there is a very low chance of actually forming a bond during a bonding step, as the selected epoxy and amine are likely to be situated far apart from each other, so the ratio of bond formation to equilibration is still relatively low in both cases.

The resulting molecular weight distributions are compared in Figure 3.2a, in terms of number average molecular weight M_n, weight average molecular weight M_w, and centrifugal average molecular weight M_z (defined in Section 1.3.1). The resultant M_ns were equal within experimental error between the two simulations, and M_w and M_z showed small but significant differences. The simulations with more bonding steps compared to movement steps produced larger molecules. This is expected, because there is less time to equilibrate between each bond formation, so reactions are more likely to form between epoxy and curative segments that are already part of larger molecules.

However, the difference in molecular weight distributions between the two simulations was deemed small enough to warrant taking advantage of the much faster computation times of the higher bonding probability option (hours rather than days or weeks, depending on the system). In an attempt to produce consistent molecular weight distributions, the ratio of accepted reaction and equilibration steps for all simulations was approximately maintained by changing $p_{bonding}$ from from 0.1 in systems with $\phi = 0.7$ to 0.067 in systems with $\phi = 0.8$ to 0.033 in systems with $\phi = 0.9$. This was necessary because systems with higher overall volume fraction have more excluded volume, so therefore more movement steps are rejected and they equilibrate slower.

The molecular weight distributions produced by the bonding simulations with various volume fractions and final cure extents are shown in Figure 3.2. In all cases, the average molecular weight increased with cure extent, as expected. The rate of increase is observed to speed up at higher cure extent, particularly for M_z, which is biased towards the presence of larger molecules. This makes sense as there is a higher probability of reacting segments that are already part of larger molecules, implying an exponential rate of increase in molecular weight.

The molecular weight distributions are approximately consistent between systems with the same amount of cure but different overall volume fractions. There is a slight trend towards a larger average molecular weight in the higher volume fraction systems. This is likely to be because more closely-packed molecules are within reaction distance of each other more frequently, so the effective rate of reaction compared to equilibration movement is increased. This is particularly evident in the traces for M_z, which is more biased by the presence of a few very large molecules than the other averages. However, any differences observed were within the experimental uncertainty quantified by the standard deviation between repeats, so all molecular weights distributions were classed as equivalent for systems with the same amount of cure.

Comparisons between the molecular weight distributions produced by simulation and those predicted using the theoretical Stockmayer model for gelation [134] (see Section 1.3.1) are given in Table 3.1 for each final cure extent. The molecular weights produced by simulation are significantly larger than those predicted by theory. This could be due to an oversimplification of the theory, but is likely to be an effect of not fully equilibrating the system between each bonding step. Therefore, the molecular weight distributions used during these simulations are unlikely to be perfect representations of experimental systems with the same overall cure extent. However, the trends are in the correct direction.

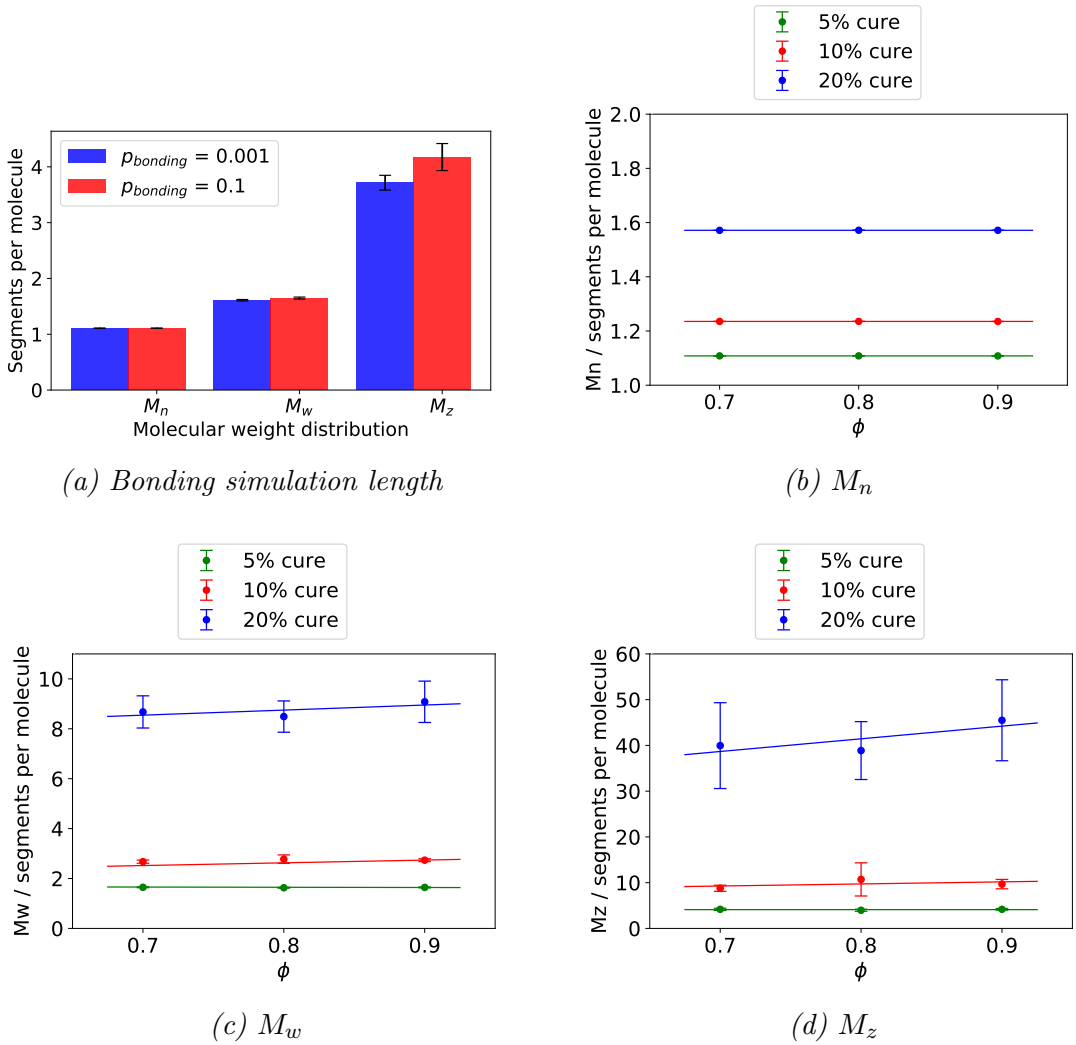

(a) Bonding simulation length

(b) M_n

(c) M_w

(d) M_z

Figure 3.2: Molecular weight distributions created by the bonding simulation using the BFM. (a) shows a comparison between the molecular weight distributions of simulations with different probabilities of bonding to movement steps. The blue bars represent a long cure where only 0.1 % of the steps attempt to form bonds, whereas the red bars represent a shorter cure where 10 % of the steps attempt to form bonds. The other plots show the molecular weight distributions formed for systems with various overall volume fractions and cure extents.

3.3.2 Energies

Total interaction energy was also calculated for systems with $\phi = 0.7$ and various cure extents of 5 %, 10 % and 20 %. Two combinations of nearest neighbour

Cure extent	M_n		M_w		M_z	
	Theory	Simulation	Theory	Simulation	Theory	Simulation
5 %	1.1065	1.1082 ± 0.0001	1.56	1.64 ± 0.01	3.3	4.1 ± 0.1
10 %	1.2332	1.2353 ± 0.0001	2.33	2.73 ± 0.05	6	10 ± 1
20 %	1.5383	1.5715 ± 0.0002	4.6	8.7 ± 0.3	12	41 ± 4

Table 3.1: Number, weight and centrifugal average molecular weights for the cluster distributions in the simulations compared to theoretical predictions made using Stockmayer's model for gelation[134].

interaction energies were used, one with attractive intraspecies and repulsive interspecies ($\epsilon_{EE} = \epsilon_{TT} = -1$, $\epsilon_{ET} = 1$), and one with repulsive intraspecies and attractive interspecies interactions ($\epsilon_{EE} = \epsilon_{TT} = 1$, $\epsilon_{ET} = -1$), where energy values are given throughout this chapter in reduced units of k_BT. The resultant total energies are shown in Figure 3.3.

Due to the high volume fraction of epoxy compared to thermoplastic, the epoxy-epoxy interactions dominate in all cases, so the sign of the total energy follows that of ϵ_{EE}. The absolute value of the total energy is 2–3 orders of magnitude higher in the cases with repulsive interspecies interactions (Figure 3.3a) than those with attractive interspecies interactions (Figure 3.3b). This implies that the former has large regions of each species and a small amount of interface, in order to maximise the number of favourable attractive interactions and minimise the number of unfavourable repulsive ones. The latter case tries to increase the amount of favourable interface by having smaller regions of each species, but due to the mismatch between the volume fractions of the components and the requirement to maintain connectivity causing some areas of high local

density, many unfavourable intraspecies interactions remain. This means that here there is more of a balance between the number of attractive and repulsive nearest neighbour interactions, so the absolute value of the total energy is smaller.

In both cases, the magnitude of the total energy reduces linearly with increasing cure extent. This is almost entirely due to a reduction in the total number of nearest neighbour interactions in the system, where bonds are formed between segments that could otherwise have interacted with each other. The lack of deviation from the linear trend provides little evidence that changing the cure extent affects the sizes of the regions of each component, or equivalently the lengthscale of the concentration fluctuations.

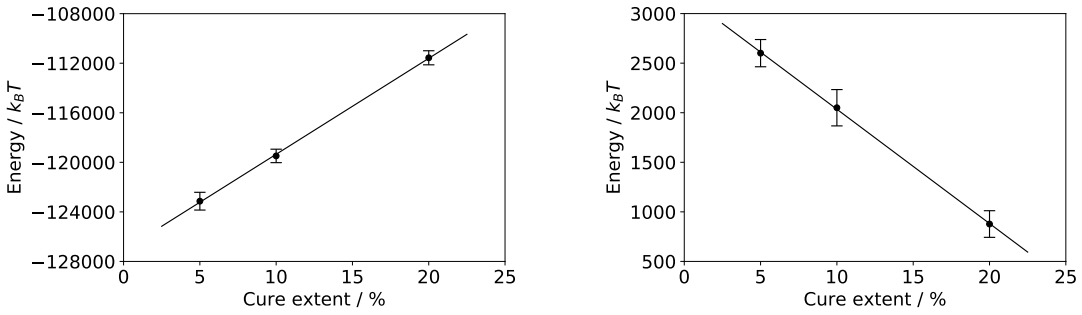

(a) $\epsilon_{EE} = \epsilon_{TT} = -1$, $\epsilon_{ET} = 1$ *(b)* $\epsilon_{EE} = \epsilon_{TT} = 1$, $\epsilon_{ET} = -1$

Figure 3.3: Plots of total energy against cure extent in systems with (a) attractive intraspecies and repulsive interspecies interactions, and (b) repulsive intraspecies and attractive interspecies interactions.

3.3.3 Radii of gyration

The average radius of gyration (R_g) of the linear thermoplastic polymer also gives some insight into the structure of the blend.

Figure 3.4 shows the effect of changing the values of the nearest neighbour interaction energies within the system on R_g. As the intraspecies interactions be-

come more repulsive and the interspecies interactions become more attractive, the average R_g increases significantly. This suggests that the thermoplastic molecules are spreading out in order to seek more interspecies epoxy contacts, so that the sizes of the regions of each component are reduced. This result is in line with the implications of the total energy calculations. Due to the large scale of the R_g axis in Figure 3.4, it is difficult to determine the effect of changing the cure extent on radius of gyration. Expanded versions are shown in Figure 3.5 for systems with volume fraction $\phi = 0.7$ and each set of nearest neighbour interactions.

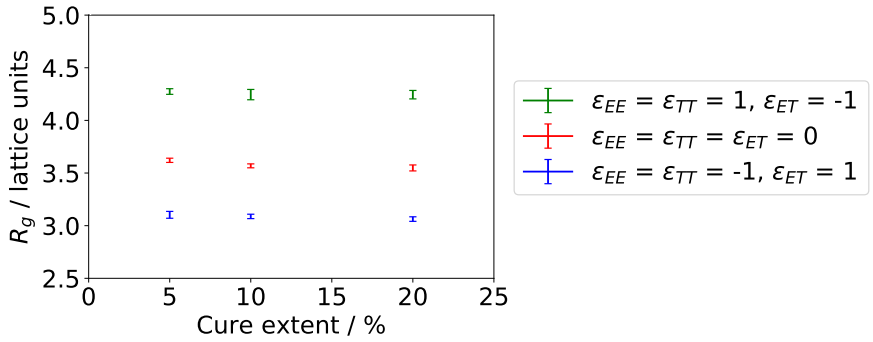

Figure 3.4: Effect of changing the energetic interactions between segments on radius of gyration for linear thermoplastic polymers in systems with energetic interactions. Green represents repulsive intraspecies and attractive interspecies interactions, red represents no interaction energies, and blue represents attractive intraspecies and repulsive interspecies interactions. The volume fractions of the systems used here were $\phi = 0.7$.

It can be seen from Figure 3.5 that increasing the cure extent causes a small but significant decrease in R_g. This is because there is more widespread connectivity within the epoxy component, which causes the epoxy component to cluster together and decreases the conformational entropy of mixing. The thermoplastic molecules are excluded, so can no longer easily spread out as easily into the epoxy component, and have reduced R_gs. This effect is most pronounced in the case with no interaction energies (Figure 3.5b) as this system is purely controlled by entropy. Where energetic interactions are present, (Figures 3.5a and 3.5c) any

changes to the entropy are countered by the dominating effects of energy, and the impact of changing the cure extent is reduced.

The last case studied here is the effect on R_g of changing the overall volume fraction for purely entropic systems with no interaction energies, shown in Figure 3.6.

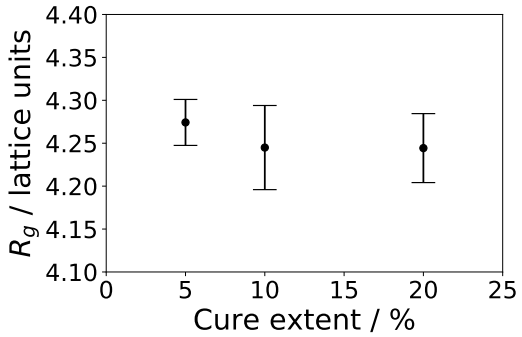

(a) $\epsilon_{EE} = \epsilon_{TT} = 1$, $\epsilon_{ET} = -1$

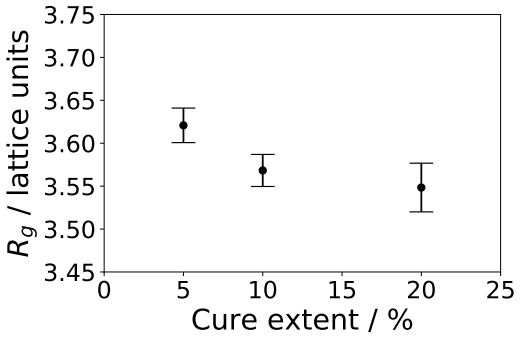

(b) $\epsilon_{EE} = \epsilon_{TT} = \epsilon_{ET} = 0$

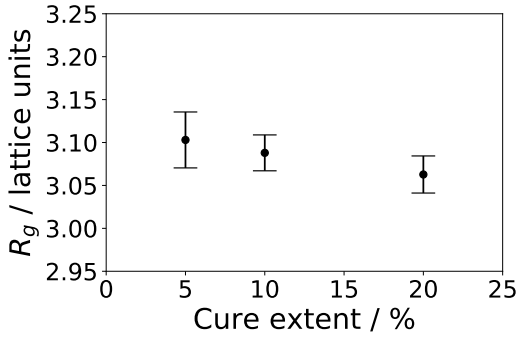

(c) $\epsilon_{EE} = \epsilon_{TT} = -1$, $\epsilon_{ET} = 1$

Figure 3.5: Close ups of the data series in Figure 3.4. Effect of changing the cure extent on radius of gyration for linear thermoplastic polymers in systems with various energetic interactions. (a) has repulsive intraspecies and attractive interspecies interactions, (b) has no interaction energies, and (c) has attractive intraspecies and repulsive interspecies interactions. The plots shown here are for systems with volume fractions of 0.7, but the trends are the same for the other tested volume fractions of 0.8 and 0.9. All graphs are plotted on the same scale, but the Rg axis is shifted for each.

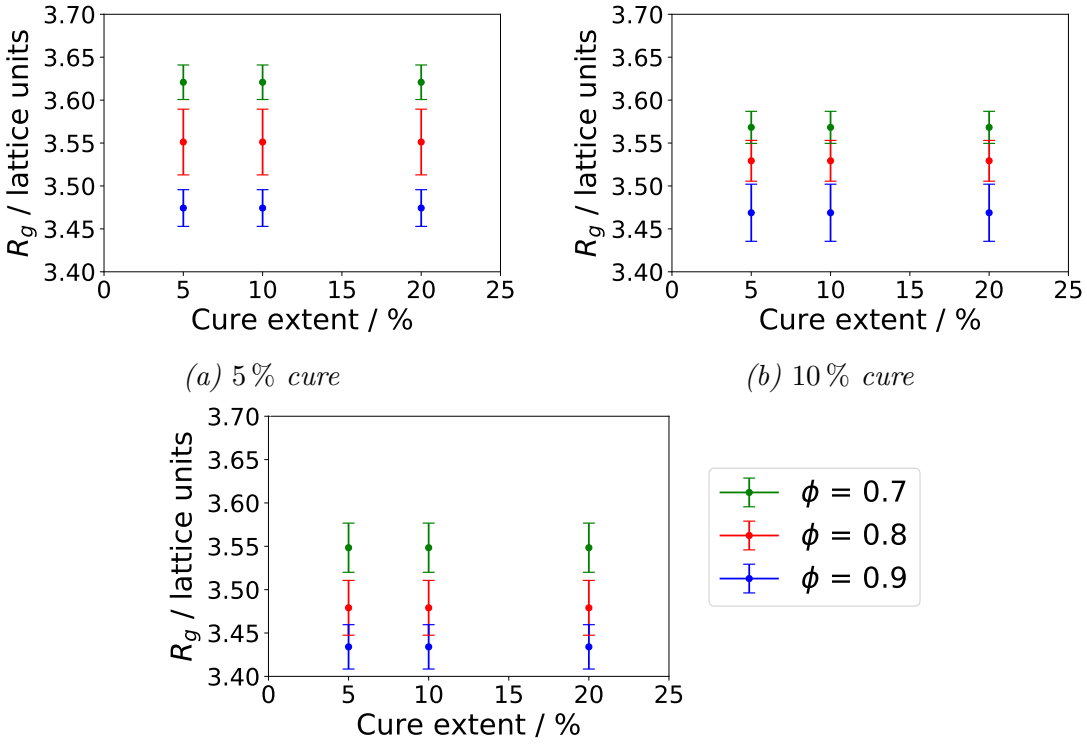

(a) 5 % cure

(b) 10 % cure

(c) 20 % cure

Figure 3.6: Effect of changing the overall volume fraction from 0.7 to 0.8 to 0.9 on radius of gyration for linear thermoplastic polymers in systems with no energetic interactions and various cure extents All graphs have the same scales.

It is clear for all cure extents that as volume fraction is increased from $\phi = 0.7$ to $\phi = 0.8$ to $\phi = 0.9$, the average R_g of the thermoplastic component decreases. This is expected, because the molecules are more spatially restricted and have less free volume in which to expand into. In corroboration with this, the average length of the bond vectors in the system decreases from 2.56 to 2.52 to 2.49 lattice units with increasing volume fraction from $\phi = 0.7$ to $\phi = 0.8$ to $\phi = 0.9$.

Increasing the overall volume fraction has a smaller impact on systems with higher cure extent. Here, the entropic effects of bonding have already reduced the values of R_g for the lower volume fraction systems with $\phi = 0.7$, and the radii of gyration cannot reduce much further in the higher volume fraction cases due to the spatial restrictions on the bond vectors already in place.

3.3.4 Radial distribution functions

Radial distribution functions offer the clearest picture of morphology, because they directly measure how the concentrations of each species vary with distance. RDFs were calculated for all the systems previously mentioned, with cure extents of 5 %, 10 % and 20 %, and overall volume fractions of $\phi = 0.7$, 0.8 and 0.9. In the $\phi = 0.7$ case, several combinations of interaction energies were also tested.

Three types of RDF were calculated for each system. $g_{EE}(r)$ shows how the average concentration of epoxy segments varies with distance from other epoxy segments, $g_{TT}(r)$ shows how the average concentration of thermoplastic segments varies with distance from other thermoplastic segments, and $g_{ET}(r) = g_{TE}(r)$ shows how the average concentration of epoxy segments varies with distance from thermoplastic segments or vice versa.

We will first examine the effect of changing the interaction energies on the RDFs between each pair of components, shown in Figure 3.7. Increasing the favourableness of the intraspecies interactions (decreasing ϵ_{EE} and ϵ_{TT}) and decreasing the favourableness of the interspecies interactions (increasing ϵ_{ET}) would intuitively cause larger regions rich in each species to form. This behaviour is indeed evident from the peaks in $g_{EE}(r)$ and $g_{TT}(r)$, and the trough in $g_{ET}(r)$ at short distances. For the systems with zero interaction energies and also with attractive interpecies interactions, all RDFs are relatively flat at distances above 7 lattice units, suggesting that only small composition inhomogeneities are present. For the systems with repulsive interspecies interactions, $g_{EE}(r)$ and $g_{TT}(r)$ are much greater than one for distances up to 13 lattice units, and then lower than one for distances of 13–26 lattice units. The opposite is true for $g_{ET}(r)$. Taken together, these indicate more long range order and larger structural inhomogeneities than the systems with other types of nearest neighbour interaction energies. The zero energy system behaves more similarly to that with attractive interspecies

interactions than that with repulsive interspecies interactions, because entropies of mixing are always positive for incompressible systems and tend to enhance homogeneity.

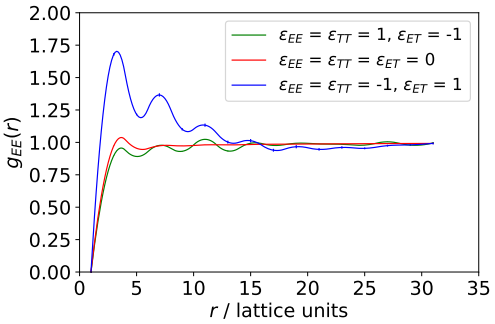

(a) Epoxy-epoxy

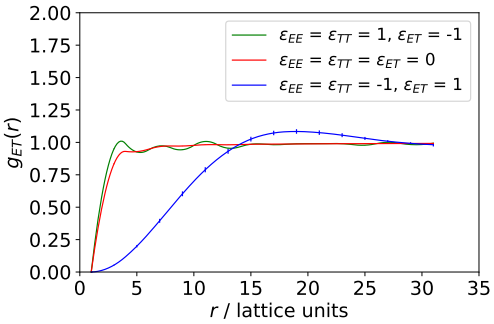

(b) Epoxy-thermoplastic

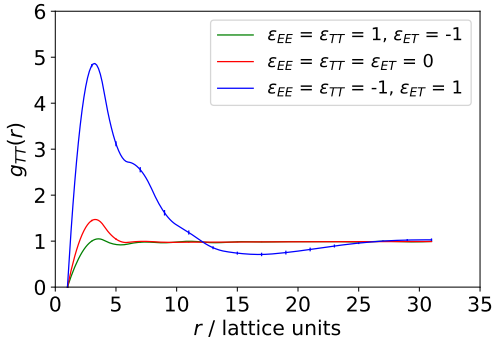

(c) Thermoplastic-thermoplastic

Figure 3.7: Epoxy-epoxy, epoxy-thermoplastic and thermoplastic-thermoplastic radial distribution functions for three combinations of nearest neighbour interaction energies. Repulsive intraspecies and attractive interspecies interactions are shown in green, zero energetic interactions are shown in red, and attractive intraspecies and repulsive interspecies interactions are shown in blue. All simulations shown here were carried out at a volume fraction of $\phi = 0.7$ and a cure extent of 5 %, but similar trends were evident for systems with 10 % and 20 % cure extent.

We will now consider each combination of interaction energies in more detail. The first case to be examined is the one shown in shown in Figure 3.8, with attractive intraspecies and repulsive interspecies interactions ($\epsilon_{EE} = \epsilon_{TT} = -1$, $\epsilon_{ET} = 1$). Figure 3.8a shows the relationship between the different types of RDF

in a system with an overall volume fraction of $\phi = 0.7$ and a cure extent of 5 %, although the traces are similar in shape for all cure extents. As mentioned above, $g_{ET}(r)$ is depleted within distances 13 lattice units and augmented between 13 and 16 lattice units, indicating the formation of relatively large regions of each component of approximately 13 lattice units in diameter. This result is corroborated by the large peak in $g_{TT}(r)$ at short lengthscales of up to 13 lattice units, and the trough at longer lengthscales. $g_{EE}(r)$ is also increased at short distances, suggesting clustering, but as the average concentration is already high due to the large amount of epoxy in the system, the peak is not as pronounced as in the thermoplastic case.

Figures 3.8b, 3.8c and 3.8d show how $g_{EE}(r)$, $g_{ET}(r)$ and $g_{TT}(r)$ change with cure extent. For more highly cured systems, $g_{EE}(r)$ and $g_{TT}(r)$ are slightly lower at short distances. Also, the depletion region in $g_{ET}(r)$ becomes slightly smaller, implying better mixing. This is counter-intuitive, because the entropy of mixing is lower for systems with higher molecular weight, so drives separation. However, as the behaviour of this system is dominated by energetic interactions rather than entropy, the explanation for the increased mixing also lies with energy. As the extent of cure increases, the number of bonds in the epoxy component increases. Directly bonded segments do not energetically interact with each other, so the number of attractive epoxy-epoxy interactions is reduced, resulting in less energetic drive towards demixing, and a more homogeneous system.

The next case to be investigated (shown in Figure 3.9) is one with no interaction energies, where all effects are purely entropic. The RDFs are very flat here, suggesting mostly random homogeneous mixing, which would be intuitively expected for a system without energetic interactions. There are, however, still peaks in $g_{EE}(r)$ and $g_{TT}(r)$ at short distances, due to geometric constraints caused by connectivity within molecules forcing small clusters to occur. This time, chang-

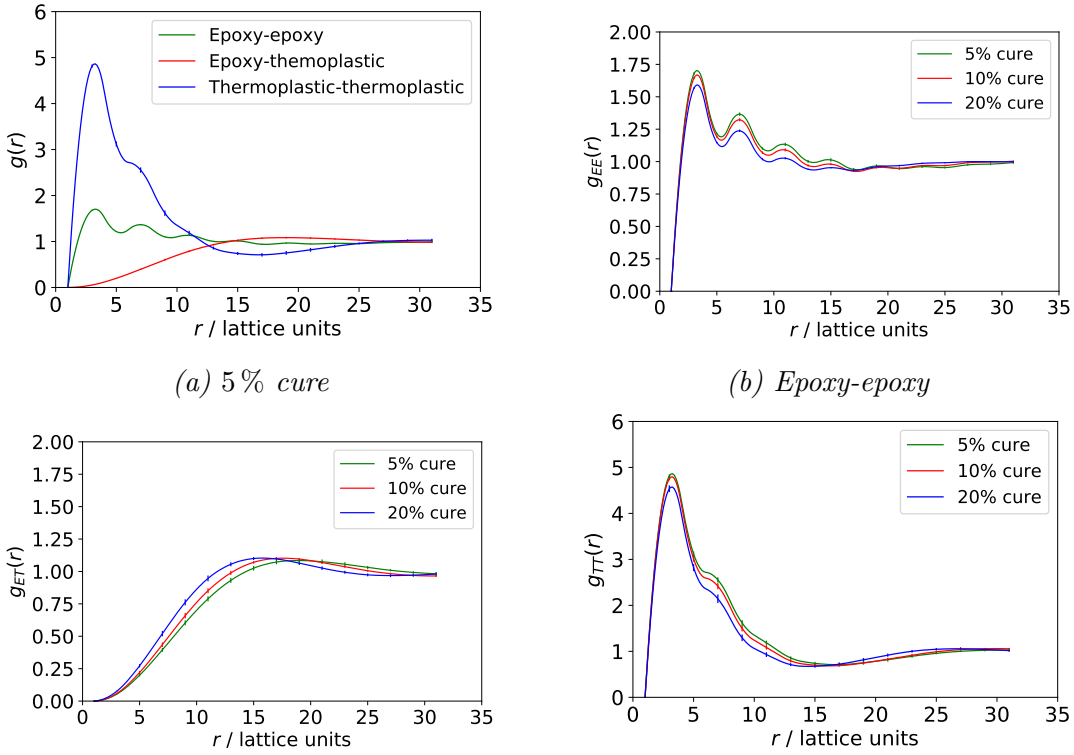

(a) 5 % cure

(b) Epoxy-epoxy

(c) Epoxy-thermoplastic

(d) Thermoplastic-thermoplastic

Figure 3.8: RDFs for systems with attractive intraspecies and repulsive interspecies interactions, $\epsilon_{EE} = \epsilon_{TT} = -1$, $\epsilon_{ET} = 1$. (a) shows the relationship between the RDFs of all pairs of components for a system with a constant cure extent of 5 %. (b), (c) and (d) show the impact of changing the cure extent on the epoxy-epoxy, epoxy-thermoplastic and thermoplastic-thermoplastic RDFs respectively. All systems shown here have an overall volume fraction of $\phi = 0.7$.

ing the cure extent has an intuitive effect on the RDFs; as the epoxy component increases in molecular weight, the decreased entropy of mixing causes inhomogeneities to become more distinct. This is evidenced by a slight increase in $g_{EE}(r)$ and $g_{TT}(r)$ and a slight depletion in $g_{ET}(r)$ at short distances.

The final combination of interaction energies studied was one with respulsive intraspecies interactions and attractive interspecies interactions ($\epsilon_{EE} = \epsilon_{TT} = 1$, $\epsilon_{ET} = -1$), shown in Figure 3.10. The RDFs here are still very flat, which is expected because the system is driven towards mixing by both the energetics

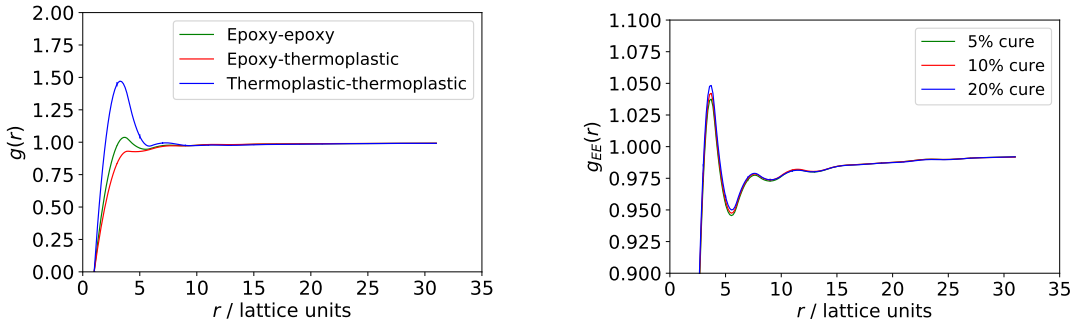

(a) 5 % cure

(b) Epoxy-epoxy

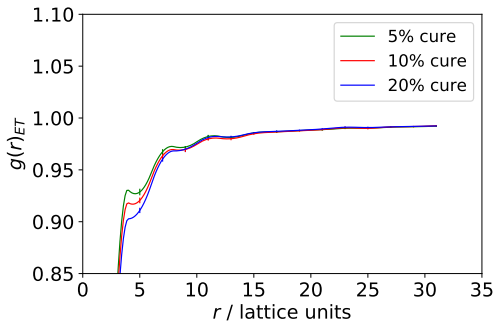

(c) Epoxy-thermoplastic

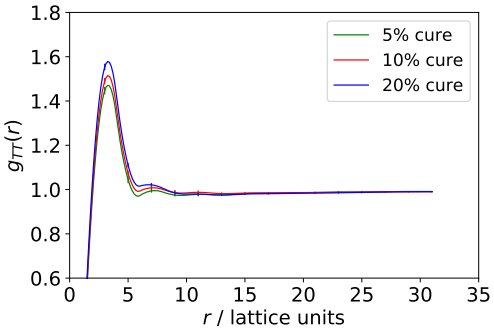

(d) Thermoplastic-thermoplastic

Figure 3.9: RDFs for systems with no energetic interactions. (a) shows the relationship between the RDFs of all pairs of components for a system with a constant cure extent of 5 %. (b), (c) and (d) show the impact of changing the cure extent on the epoxy-epoxy, epoxy-thermoplastic and thermoplastic-thermoplastic RDFs respectively. All systems shown here have an overall volume fraction of $\phi = 0.7$.

and entropics. Although there is generally a well mixed morphology, there are still small-scale inhomogeneities caused by molecular connectivity and solvation shells. This short distance peak is higher in $g_{TT}(r)$ than $g_{EE}(r)$ because the thermoplastic molecules are generally larger, causing clustering and enhancing the local concentration. Also, there are fewer thermoplastic segments overall, so any inhomogeneities have a more pronounced effect on the height of the peak. Altering the cure extent does not have much effect on morphology, because energetic effects dominate over entropic ones. Therefore, increasing molecular connectivity only enhances inhomogeneity very slightly.

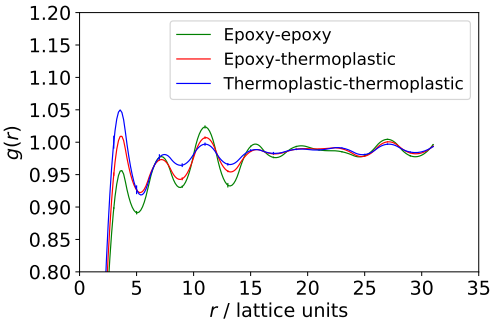

(a) 5 % cure

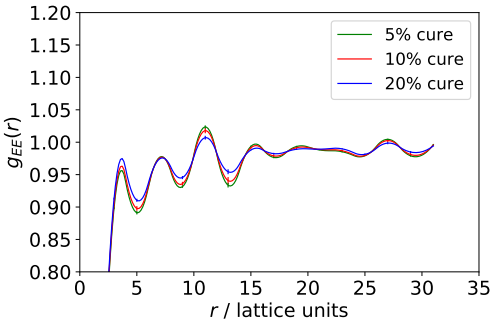

(b) Epoxy-epoxy

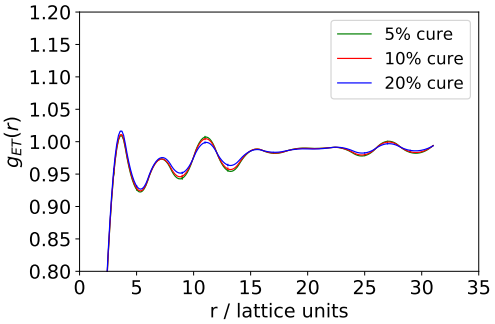

(c) Epoxy-thermoplastic

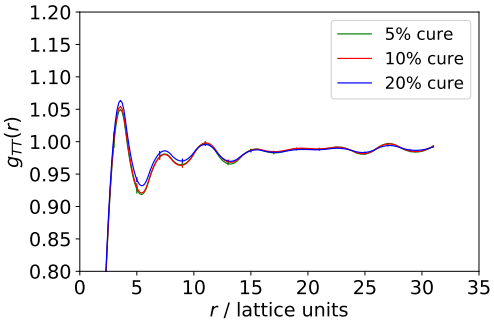

(d) Thermoplastic-thermoplastic

Figure 3.10: RDFs for systems with repulsive intraspecies and attractive interspecies interactions, $\epsilon_{EE} = \epsilon_{TT} = 1$, $\epsilon_{ET} = -1$. (a) shows the relationship between the RDFs of all pairs of components for a system with a constant cure extent of 5 %. (b), (c) and (d) show the impact of changing the cure extent on the epoxy-epoxy, epoxy-thermoplastic and thermoplastic-thermoplastic RDFs respectively. All systems shown here have an overall volume fraction of $\phi = 0.7$.

The final comparison that will be considered is the difference between systems with varying overall volume fraction and otherwise equal parameters, shown in Figure 3.11. Increasing the volume fraction enhances the correlations between segments, so that all RDFs for the $\phi = 0.9$ and $\phi = 0.8$ systems have greater variation at long distances than for $\phi = 0.7$. For all types of RDF, increasing the volume fraction also causes a decrease in the size of the initial peak, corresponding to the first shell of nearest neighbours around each segment. This is because the overall concentration of each species is higher, but geometric constraints spatially restrict the number of segments that can fit closely together. Therefore, the ratios between the concentrations in the nearest neighbour shell and the overall average

concentrations are lower.

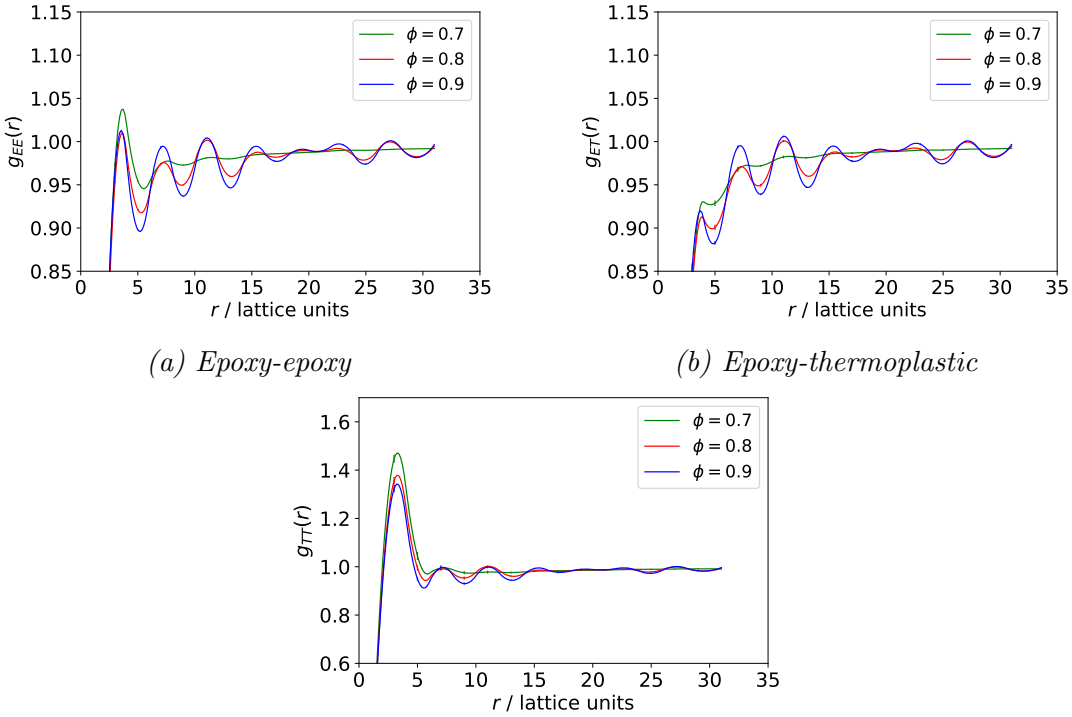

(a) Epoxy-epoxy

(b) Epoxy-thermoplastic

(c) Thermoplastic-thermoplastic

Figure 3.11: The effect of changing the overall volume fraction from $\phi = 0.7$ (green) to $\phi = 0.8$ (red) to $\phi = 0.9$ (blue) on the epoxy-epoxy, epoxy-thermoplastic and thermoplastic-thermoplastic RDFs. All systems shown here have no energetic interactions and a cure extent of 5 %.

3.4 Conclusions and further work

In this chapter, a Monte Carlo model based on the bond fluctuation model has been developed to investigate concentration fluctuations in blends of branched epoxy and linear thermoplastic molecules. The effects of changing the cure extent, the nearest neighbour energetic interactions and the overall volume fraction of the system have been investigated. Calculations for molecular weight distributions within the epoxy components, total interaction energies, radii of gyration

of the thermoplastic molecules, and radial distribution functions for all pairs of components have been carried out.

The epoxy molecular weight distributions varied significantly between the simulation values and theoretical calculations using the Stockmayer model for gelation,[134] even though the trends were in the right direction. This can be partially explained by the invalidity of using Monte Carlo methods for strictly non-equilibrium processes like irreversible bonding. It is possible that by using a larger simulation box and allowing more equilibration moves between each bonding step, distributions closer to the theoretical predictions could be gained. A truer representation of the range of molecular weights in an experimental system could also be obtained by running the bonding simulation in the presence of nearest neighbour energetic interactions, and adjusting the relative reactivity rates of the primary and secondary hydrogen on each amine.

The simulations produced sensible results for the total interaction energies, radii of gyration and radial distribution functions. Structure factors were calculated, but not shown here as they contain the same information as the radial distribution functions in a less approachable way. They would, however, allow comparison between the model and experimental results measured by small-angle neutron scattering if the initial conditions were chosen appropriately. This allows the three structure factors ($S_{EE}(q)$, $S_{ET}(q)$ and $S_{TT}(q)$) to be combined into a single trace using Equation 3.6, giving the scattering intensity ($I(q)$) expected at each q value during experimental measurement.[184] b_E and b_T denote the scattering lengths of the epoxy and thermoplastic segments respectively.

$$I(q) = b_E^2 S_{EE}(q) + b_T^2 S_{TT}(q) + 2 b_E b_T S_{ET}(q) \tag{3.6}$$

It is worth noting that these comparisons would only be valid for systems exhibiting upper critical solution temperature behaviour (see Section 1.2.4.1),

because the compressibility effects required to study systems with lower critical solution temperature behaviour are not included in the model. It may be possible to extend the model to encompass these compressibility effects by allowing the number of molecules to vary on a lattice of constant size, but no reliable way of adding branched molecules to an already dense system has yet been found.

Chapter 4

Design and measurement of a model experimental system

4.1 Introduction

The work in this chapter takes a detour from the more theoretically-based computational methodologies of the previous chapters, in order to demonstrate that using complementary techniques can offer a fuller understanding.

4.1.1 Small angle neutron scattering

One of the most commonly used experimental techniques to investigate the morphology of polymer blends is small angle neutron scattering, or SANS. Scattering techniques are more appropriate for determining structural properties than direct measurement methods, such as microscopy, because they are quantitative and average over many particles in the material, so give more representative results.[185] However, scattering is often used in conjunction with microscopy in

order to corroborate the findings and give a more complete picture.[186]

Neutron scattering has several advantages over more traditional methods such as X-ray or light scattering. Firstly, a major benefit lies in the fact that neutrons are scattered by atomic nuclei rather than electrons as in X-ray scattering. X-ray scattering intensity is directly related to electron density, so heavy atoms which contain many electrons appear clearly, but there is negligible scattering from light atoms with few electrons such as hydrogen. Unfortunately most polymers are hydrocarbons with only a few atoms other than carbon or hydrogen present in their structures. Due to the lack of heavy atoms and the similarity between the chemistries in all components of a polymer blend, it can be difficult to gain enough contrast to distinguish the phases in X-ray measurements. Light scattering depends on polarisability,[187] which is related to refractive index, and is in turn dependent on the size and structures of the constituent monomers of each polymer. Therefore the amount of contrast in a light scattering experiment is again highly dependent on the differences between the chemical structures of the polymers.[188]

Neutron scattering offers a simple solution to the lack of contrast between components, due to the fact that the neutron-nucleus interaction (characterised by the 'scattering length' of the nucleus) varies quite haphazardly across the periodic table. In particular, hydrogen and deuterium have very different scattering lengths, so by replacing (or labelling) the hydrogen atoms in one component of the blend with deuterium, good contrast between even chemically similar components can be observed.[184]

Another variation between the different types of scattering lies in the size of the structures that can be studied. Scattering techniques are most effective when the wavelength of the radiation is approximately equal to the lengthscales of the structures of interest.[185] Visible light has a wavelength of approximately 400–

700 nm, so only structures larger than 100 nm can be probed.[187] Both X-rays and neutrons have much smaller wavelengths and are able to probe structures within the 1-600 nm range.[186,187] Therefore, although all scattering techniques can be used to investigate phase separation, neutron scattering is by far the best for studying concentration fluctuations in the single phase region of the phase diagram, as it offers good contrast and and probes appropriate lengthscales.

The 'small angle' part of small angle neutron scattering refers to the angle θ between the incident and scattered wave. This is related to the wavevector change $\boldsymbol{q}$ of the scattered radiation by Equation 4.1, where λ is the wavelength of the radiation. The magnitude of $\boldsymbol{q}$ describes the wavenumber q of the radiation, which is related to distance in real space by $d = 2\pi/q$. The relationship between q and θ is shown pictorially in Figure 4.1.[184]

$$|\boldsymbol{q}| = q = \frac{4\pi}{\lambda}\sin(\theta/2) \tag{4.1}$$

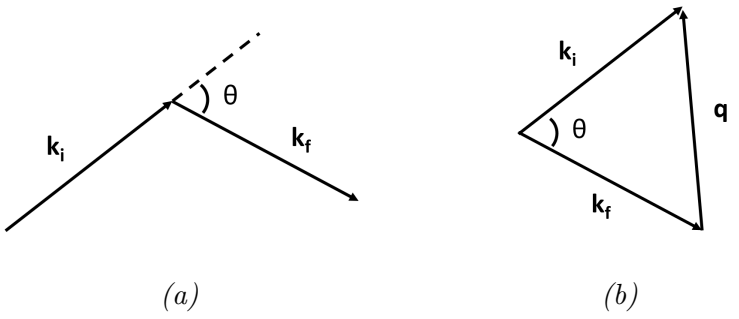

(a) *(b)*

Figure 4.1: Schematic showing the relationship between the wavevector change $\boldsymbol{q}$ *of the scattered light and the scattering angle* θ*.* $\boldsymbol{k_i}$ *and* $\boldsymbol{k_f}$ *refer to the wavevectors of the initial and final scattered radiation beam. Figure (a) shows the real space positions of the vectors, and (b) shows them shifted to demonstrate the value of* $\boldsymbol{q}$ *more clearly.*

In SANS measurements, the value of θ is controlled as the angle between the sample and detector relative to the incident neutron beam (practically altered by changing the distance between the sample and detector), and the q–range

is determined from this using Equation 4.1. In order to probe the mesoscopic length scales required for studying phase separation, the value of q and therefore the value of θ must be minimised. A practical lower limit on θ is imposed by a requirement to protect the detector from the large amount of unscattered neutrons experienced at $\theta = 0$.[184]

4.1.2 The Random Phase Approximation

The Random Phase Approximation (RPA) is a mean field theory developed by de Gennes[29] that describes the q dependence of the scattering of interacting, slightly inhomogeneous polymer mixtures, and allows the χ interaction parameter from the Flory-Huggins model to be obtained experimentally.

In the RPA, the structure factor $S(q)$ for a blend of components A and B is given by Equation 4.2. It is a combination of the ideal chain structure factors for each component ($S_A(q)$ and $S_B(q)$), biased by their volume fractions (ϕ_A and ϕ_B). A term involving the χ parameter is included to account for interactions between the components.

$$\frac{1}{S(q)} = \frac{1}{\phi_A S_A(q)} + \frac{1}{\phi_B S_B(q)} - 2\chi \tag{4.2}$$

The ideal chain structure factors for each species are given by Equation 4.3, where N_i is the number of segments in a molecule of polymer species i, and $g_{Di}(q)$ is the Debye scattering function for that species (i.e. the radial distribution function for a non-interacting polymer chain of N_i segments). $g_{Di}(q)$ is given by Equation 4.4, where R_{gi} is the radius of gyration for a chain of species i, and q is the wavenumber of the radiation used for scattering.

$$S_i(q) = N_i g_{Di}(q) \tag{4.3}$$

$$g_{Di}(q) = \frac{2}{R_{gi}^2 q^2}\left[R_{gi}^2 q^2 - 1 + e^{-R_{gi}^2 q^2}\right] \tag{4.4}$$

In the low q limit where $R_{gi}^2 q^2$ tends to zero, a Taylor expansion of the exponential in Equation 4.4 can be carried out, such that $g_{Di}(q)_{q\to 0} = 1 - R_{gi}^2 q^2/3$. The ideal chain structure factors are then given by Equation 4.5.

$$S_i(q)_{q\to 0} = N_i\left(1 - \frac{R_{gi}^2 q^2}{3}\right) \tag{4.5}$$

Substituting Equation 4.5 for each component A and B into Equation 4.2 gives the structure factor for the interacting blend in the low q limit as Equation 4.6.

$$\frac{1}{S(q)_{q\to 0}} = \frac{1}{\phi_A N_A(1 - \frac{R_{gA}^2 q^2}{3})} + \frac{1}{\phi_B N_B(1 - \frac{R_{gB}^2 q^2}{3})} - 2\chi \tag{4.6}$$

Further Taylor expansions can then be carried out for the $(1 - R_{gi}^2 q^2/3)^{-1}$ terms in the low q limit where $R_{gi}^2 q^2$ tends to zero, to give $(1 + R_{gi}^2 q^2/3)$ in each case. Simplifying the expression gives then Equation 4.7.

$$\frac{1}{S(q)_{q\to 0}} = \frac{1}{\phi_A N_A} + \frac{1}{\phi_B N_B} - 2\chi + \frac{1}{3}\left(\frac{R_{gA}^2}{\phi_A N_A} + \frac{R_{gB}^2}{\phi_B N_B}\right) q^2 \tag{4.7}$$

This implies that in the low q regime, a plot of $1/S(q)$ against q^2 should produce a linear trend with a $1/S(0)$ intercept given by Equation 4.8.

$$\frac{1}{S(0)} = \frac{1}{\phi_A N_A} + \frac{1}{\phi_B N_B} - 2\chi \tag{4.8}$$

If the degree of polymerisation and volume fraction of each component are known, this methodology therefore allows χ interaction parameters to be determined from neutron scattering experiments.

4.1.3 Aim

As described in Chapter 1, aerospace resins are created by mixing together epoxy monomers and thermoplastics and curing under a temperature ramp, usually with a diamine curative. During the curing process, the molecular weight of the epoxy component increases, raising the free energy of mixing and causing the system to undergo reaction-induced phase separation. Shifts in phase behaviour can also be caused by temperature changes, such as those in the curing temperature ramp. Therefore, it can be difficult to differentiate between the competing effects of changing temperature and cure extent on the phase separation process.

The work in this chapter develops a model system capable of separating the effects of temperature and cure. Cure extent can be controlled independently of temperature by restricting the amount of either the epoxy or curative available to the system. Once the epoxy has been cured to the full extent allowed by the stoichiometry in each sample, the temperature can then be altered without changing the chemistry of the system. For accurate results, a well-behaved system was required that cured without unwanted side-reactions such as etherification, and did not undergo any chemical changes on heating.

The aim of this work was develop a model system for studying the competing effects of cure extent and temperature on concentration fluctuations using small angle neutron scattering, and to make estimates of the χ interaction parameters for each blend. These results are important, as it is hoped that the resultant structure factors could later be compared to those simulated using the model outlined in Chapter 3, in order to test the model's predictions of concentration fluctuations. The model must be run in equilibrium at fixed temperatures and cure extents, so the experimental system should be measured in the same conditions. χ interaction parameters extracted from the experimental data would allow calibration of the intersegment energetic interactions in the model.

4.2 Materials and methods

Firstly, the materials and characterisation methods used during this part of the work will be detailed, and descriptions of the experimental procedures will be given.

4.2.1 Materials

Bisphenol A diglycidyl ether (DGEBA with an epoxide equivalent weight of 172) was purchased under the brand name of Tactix 123 from Huntsman. Hexamethylenediamine (HMDA) was purchased from Sigma Aldrich. Deuterated poly(ether sulfone-D8) with an M_n of 4000 g mol^{-1} and M_w of 6000 g mol^{-1} was purchased from Polymer Source, Inc. Isophorone diamine (IPDA) was purchased under the brand name of Aradur 42 B2 from Huntsman. PES/PEES polymer was sourced internally from Solvay. 4,4'-Dichlorodiphenyl sulfone (DCDPS), bisphenol S, sulfolane, methanol and potassium carbonate were purchased from Sigma Aldrich. J-B Kwik Weld epoxy glue was purchased from J-B Weld, and 0.1 mm thick, 99.5 % pure aluminium foil of EN-AW 1050 A (Al 99,5) alloy and H0 (soft) temper was purchased from Aluxfoil Bázis Ltd. All materials were used as supplied.

4.2.2 Characterisation

NMR analysis was carried out by Intertek by measuring ^{1}H spectra on an Eclipse +500 instrument at 80 °C with d_6-DMSO used as the solvent. GPC analysis was carried out by Sheffield Analytical and Scientific Services using a 650 mm PLgel 5 µm Mixed-C column with a chloroform solvent, and a PLgel 3 µm Mixed-E column with a tetrahydrofuran (THF) solvent. Microscopy was undertaken using

a Zeiss Axio Imager M2m. DSC was performed using a Mettler Toledo DSC3+ instrument, under a temperature ramp of $10\,^{\circ}\mathrm{C\,min^{-1}}$ unless otherwise stated. Rheology was carried out using an Ares-G2 rheometer, under a frequency sweep from $0.628\,\mathrm{rad\,s^{-1}}$ to $628\,\mathrm{rad\,s^{-1}}$ with a constant shear strain of 10 %. SANS was performed using the D33 massive dynamic q-range small-angle diffractometer at the Institut Laue-Langevin in monochromatic mode.

4.2.3 Synthesis of poly(ether sulfone)

Non-deuterated poly(ether sulfone) was synthesised with a similar molecular weight to the deuterated version used for SANS, in order for initial tests to be carried on the system without purchasing large amounts of very expensive deuterated material.

65 g of 4,4'-dichlorodiphenyl sulfone (DCDPS) was weighed into a 500 ml 3 necked round-bottom flask with side arms. 50.756 g of bisphenol S was weighed into a 120 ml glass jar, then transferred to the round-bottom flask through the central arm with a powder funnel. The glass jar and powder funnel were rinsed into the round-bottom flask with approximately 50 ml of sulfolane, and a further 150 ml of sulfolane was added. A metal paddle stirrer was inserted into the round-bottom flask via the central arm, and stirred by hand to break up agglomerates. The contents of the flask were then left to stir overnight at room temperature using the paddle stirrer powered by compressed air, while applying nitrogen through one of the side arms.

28.852 g of sieved, oven-dried potassium carbonate was weighed into an oven-dried 120 ml glass jar. This was then slowly added to the round-bottom flask over a 10 min period through a side-arm powder funnel, while stirring fast to avoid clumping. Residual potassium carbonate was rinsed from the glass jar and powder funnel into the round-bottom flask with approximately 50 ml of sulfolane.

The round-bottom flask was transferred to a Julabo SL-12 oil bath, and stirring and nitrogen flow were reapplied. The oil bath was heated to 180 °C for 30 min, then 210 °C for 1 h and finally 230 °C for 4 h to allow the monomers to polymerise. The round-bottom flask was then removed from the oil bath and clamped on a cork ring to cool.

After cooling enough to handle, the contents of the round-bottom flask were precipitated in 3.5 l of hot water in a 5 l glass beaker, using a Silverson L5M high shear mixer with a large hole head. The fine particles and most of the water were then decanted, and the beaker refilled to 3.5 l with hot water. The contents were macerated for another 20 minutes using a medium hole Silverson head. The precipitate was then passed through a Bücher funnel with Whatman grade 3 filter paper into a 4 l Bücher flask under vacuum to remove the water.

The precipitated polymer was washed once with 3.5 l of cold water and 2 ml of acetic acid with a medium sized Silverson head and filtered using the Bücher funnel and grade 3 filter paper, then washed and filtered a further 4 times with cold water in the same manner, the final time using a fine hole Silverson head. After filtering the last time, the filter funnel was filled with 400 ml of methanol to wash the polymer. This was filtered through, and vacuum was applied to remove the last of the methanol. The resulting polymer was added to a 500 ml glass jar and the top covered in 2 layers of foil with holes poked through. This was placed in a vacuum oven at 85 °C for two days, turning every hour to dry the polymer.

The resulting polymer was submitted for NMR analysis. It was determined to consist of 100% poly(ether sulfone) groups with chlorine end groups as expected. The molecular weight was 5452 g mol^{-1} and there was 1.16 wt.% of residual sulfolane solvent.

4.2.4 Solubility tests

The solubility of poly(ether sulfone) thermoplastic (PES) was measured in both pure DGEBA epoxy monomer and a partially cured mixture of DGEBA epoxy monomer with one hexamethylenediamine (HMDA) molecule per 20 DGEBA molecules. This was carried out to ensure solubility of the thermoplastic for SANS measurements, and to determine the thermoplastic concentration and temperatures required for these measurements.

1 g of PES was added to a 60 ml glass jar, and 19 g of DGEBA monomer or partially cured DGEBA was added to give 5 wt.% of PES. This was placed in an oil bath and stirred using a compressed air powered metal stirrer. The mixture was left to stir for one hour at 60 °C to see if the PES dissolved. If not, the temperature was raised by 10 °C and the mixture left to stir for a further hour. This process was repeated until the PES dissolved, at which point further PES was added to raise the concentration by 5 wt.%, and the mixture left to stir at the same temperature for another hour.

This method was iterated until 20 wt.% of PES (the preferred concentration of the deuterated component in SANS measurements) was dissolved at 90 °C. The solution was then left to cool. The PES did not precipitate out as the temperature was reduced.

4.2.5 Curing of DGEBA with hexamethylenediamine

In order to make measurements at varying levels of epoxy cure, DGEBA was reacted with HMDA curative with a limited amount of curative and a large epoxy excess. The curing reaction was carried out in the following manner.

DGEBA was weighed into glass jars, one for each sample and one additional

jar of approximately 20 g for grinding with HMDA and adjusting concentrations. These solid samples were melted in an oil bath or oven at 60 °C until liquid, and then left to cool to become viscous. Equal masses of HMDA and viscous DEGBA were weighed into a mortar, usually with approximately 3 g of each. They were then ground to a paste with a pestle until a small, well-distributed particle size could be seen under the microscope, working quickly to ensure the DGEBA and curative did not start reacting while being ground. This mixture was then added to the jars of melted DGEBA to give the required ratio of HMDA to DGEBA in each, bearing in mind that the paste also contained some DGEBA. Additional DGEBA was added to the jars to adjust the ratio if necessary. The DGEBA/HMDA was then placed in an oil bath at 60 °C and stirred using a compressed air powered metal stirrer for 2 h to cure.

4.2.6 Storage tests

Storage tests were carried out on equivalent systems to those measured by SANS, in order to determine how long and under what conditions the samples could be stored prior to the SANS measurements.

Two 60 g batches each of partially cured DGEBA with a 20:1 and a 40:1 ratio of DGEBA to HMDA were prepared according to the method in Section 4.2.5 in 250 ml glass jars.

Using the first batch of each cure ratio, two subsamples were prepared, one containing 10 wt.%, and one 20 wt.% of non-deuterated PES. For the 10 wt.% samples, 2 g of PES was weighed into 60 ml glass jars, and 18 g of partially cured DGEBA was added. These were then stirred in an oil bath at 90 °C for 1 h until the PES had dissolved. The same process was repeated for each of the 20 wt.% samples, except this time using 4 g of PES and 16 g of partially cured DGEBA.

Samples were prepared for storage by weighing approximately 2 g of each material into 8 ml glass vials, placing under nitrogen to expel excess air and sealing the caps with parafilm. 6 samples were made for each batch of partially cured DGEBA, and 3 for each mixture of partially cured DEGBA with added PES.

The samples were then placed in their designated storage conditions: ambient, desiccator and −28 °C freezer. Two repeats were carried out for each batch of partially cured DGEBA in each storage condition, and one for each sample with dissolved PES in each storage condition.

Glass transition temperatures were measured by DSC for each of the samples to determine if any changes had taken place in the systems. DSC measurements were made for all samples before storage and after 66 days in their designated storage conditions. A measurement was also taken for one of the samples of each batch of partially cured DGEBA in ambient conditions after 10 days.

4.2.7 Design of SANS sample holders

Considerable thought was put into the design of the sample holders for the SANS measurements. In order to measure at a range of temperatures, the samples had to be inserted into a metal adaptor that was then placed in a heating block, shown in Figure 4.2.

The initial idea was to use quartz cells as the sample holders, but this was impossible due to the opening being too small to insert the viscous samples. Instead aluminium sample holders were made by the workshop at the University of Sheffield, as aluminium tends to induce only weak scattering by neutrons. The bottom layers of the sample holders were made out of single 2.75 mm thick pieces of aluminium, with small wells cut into them to contain the samples. After sample

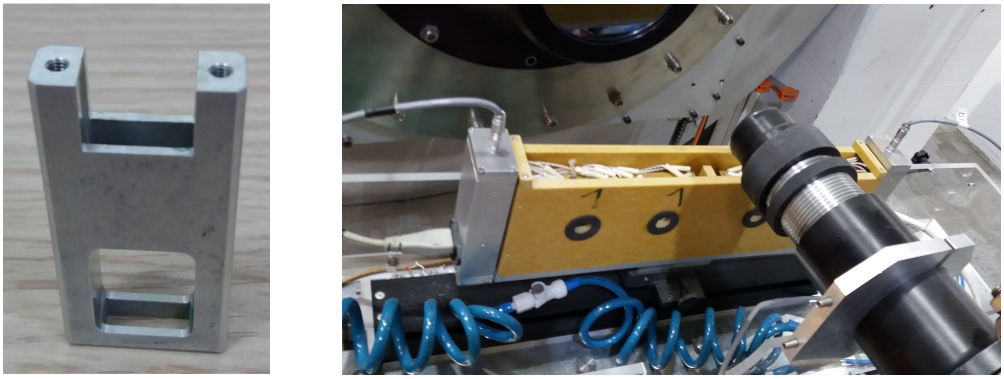

(a) Adaptor *(b) Heating block*

Figure 4.2: Photos of the (a) the adaptor the sample holders were placed inside and (b) the heating block used for the SANS measurements, with four sample wells in two independently controlled temperature regions.

insertion, a 0.5 mm thick top layer of aluminium would be glued in place to seal the samples inside the holder. However, a trial run of an empty sample holder in the neutron beam showed strong scattering, likely from polycrystalline structures in the aluminium, which would have obscured the results from the samples.

Therefore, the bottom layer of the sample holder was trimmed to leave a piece with a hole all the way through, and a layer of 0.1 mm thick, 99.5 % pure aluminium foil was attached to the base instead, using J-B Kwik Weld epoxy glue applied with a paintbrush. After sample insertion, another layer of foil was glued onto the top of the holder to seal in the sample. Once this glue had cured, a further layer of glue was applied around the edges of the sample holder to contain any leaks. Photos showing the sample holder before the top layer of foil had been glued in place are shown in Figure 4.3. The dimensions of the sample well were 17.6 mm by 8.8 mm by 2 mm.

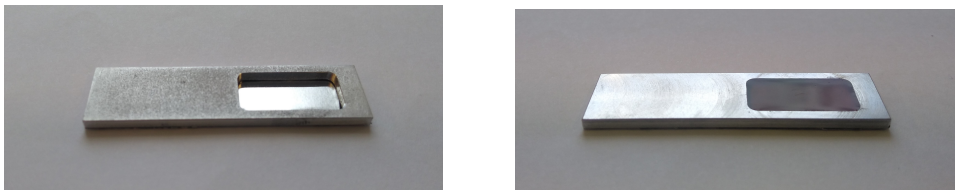

(a) Before sample insertion *(b) After sample insertion*

Figure 4.3: Photos of the final design of the sample holders used for the SANS experiments. The pictures were taken before the top layer of foil was glued in place to seal the samples inside.

4.2.8 Preparation of samples for SANS

Samples containing blends of partially cured DGEBA in 80:1, 40:1, 20:1 and 10:1 stoichiometric ratios of DGEBA to HMDA curative, and 20 wt.% of deuterated PES, were prepared for SANS measurements.

20 g of each ratio of partially cured DGEBA were made in 60 ml glass jars according to the procedure detailed in Section 4.2.5. These were then stored in the freezer for 3 weeks until the deuterated PES was delivered.

The partially cured DGEBA samples were removed from the freezer and heated to 60 °C in an oven to reduce their viscosity. For each of the four DEGBA to curative ratios, 0.13 g of deuterated PES was weighed into a small aluminium dish and 0.52 g of partially cured DGEBA was added. These samples were mixed by hand using small aluminium nails and placed in the oven at 90 °C for 1 h to dissolve. Incomplete dissolution was observed, so the oven temperature was raised to 100 °C for a further 30 min to ensure the PES was fully dissolved. Dissolution was tested for by checking by eye that the samples were transparent, and by running a DSC to ensure that only one T_g was present for the mixed phase.

The samples were moved to a vacuum oven at 100 °C and degassed to remove air bubbles for approximately 30 min until no further air bubbles were expelled. The samples were then transferred to the aluminium SANS sample holders using a

metal spatula, periodically returning to the 90 °C oven to reduce their viscosities. The sample holders were placed into the vacuum oven to degas again, before being sealed by attaching the top layer of foil and leaving the glue to cure in the fridge overnight. The samples were shipped to the Institut Laue-Langevin in dry ice and stored in a −20 °C freezer for 7 days before measurement.

4.2.9 SANS measurements

The scattering from the blends of partially cured DGEBA and deuterated PES was measured using small angle neutron scattering (SANS). Measurements were performed using the D33 small-angle diffractometer at the Institut Laue-Langevin. A wavelength filter of 5 Å and two detector distances were used, allowing a q range from 0.04 $Å^{-1}$ to 0.57 $Å^{-1}$ to be measured. Data was collected for 30 min at a detector distance of 12.8 m and 15 min at a detector distance of 5 m to ensure good counting statistics. The path length of the beam within the samples was approximately 2 mm, and the diameter of the beam was 7.7 mm.

A heating block with two independent Eurotherm temperature controllers was used (see Figure 4.2b). The four samples were split into two sets (10:1 and 20:1 epoxy to amine ratios, and 40:1 and 80:1 epoxy to amine ratios), with each set placed in a separately heated region. The first set was heated through the entire cycle detailed below, with one measurement taken for each sample at each temperature, and the process was then repeated for the second set of samples. Each sample was measured at temperatures of 60 °C, 80 °C, 100 °C, 120 °C and 140 °C before reducing the temperature back to 60 °C and taking a final repeat measurement to check whether the system had changed from its initial state.

4.3 Results and discussion

In this section, the development and characterisation of the model system designed for small-angle neutron scattering measurements will be discussed, as well as the results from these experiments.

4.3.1 Development of a model experimental system

In order to work with as simple a model system as possible, difunctional DGEBA was chosen as the epoxy monomer, so that any branching was controlled by the curative. Hexamethylenediamine (HMDA) was chosen as the preferred curative, due its ability to cure epoxy resins at low temperatures without unwanted side-reactions such as etherification, and its availability in a deuterated form for SANS experiments. HMDA is not a curative used in aerospace as it results in materials without adequate temperature resistance, but it is frequently used in the automotive industry and is representative enough for a model system. The thermoplastic of choice was either a PES/PEES copolymer, used as a toughener most aerospace applications, or PES as a chemically simpler substitute. In order to measure concentration fluctuations within the blends, it was imperative that the chosen thermoplastic was soluble in the epoxy component at the temperatures measured during SANS.

In Section 4.1.3, it was stated that the level of cure in the system would be controlled by limiting the quantity of either the epoxy or the diamine curative. A prerequisite of the chosen system was that it would not undergo further reaction with temperature once cured to the prescribed extent. Epoxy groups are generally more reactive than amine groups and can undergo self-reaction, although usually only at high temperatures. Therefore, an amine excess was preferred to epoxy, as the remaining unreacted material would be less likely to experience any undesired

or unexpected further reaction.

4.3.1.1 Amine excess

As stated above, HMDA was the desired curative for this system, due to the ability to buy it in deuterated form. HMDA is a crystalline solid at room temperature, with a documented melting point of approximately 42 °C and boiling point of 205 °C.[189] Measurements of concentration fluctuations or phase behaviour require the material to be in liquid form, so the first step was to melt the HMDA. This was attempted by placing a few grams of crystalline HMDA into an 8 ml glass vial and submerging partway in an oil bath set to 60 °C.

Unfortunately, although the HMDA melted to a liquid, it remained cloudy instead of turning clear, and a crust of crystalline material appeared around the top rim of the vial (see Figure 4.4). Two possible causes of the cloudiness were suspected. Firstly, HMDA is hygroscopic and absorbs moisture from the atmosphere, so the cloudiness may have been due to incorporated water droplets. Secondly, although the quoted boiling point of HMDA is 205 °C, there is evidence in the literature that it undergoes sublimation, which is sometimes used as a purification method.[190] This would explain both the cloudiness and the solid crust as recrystallised sublimated material.

In order to determine the cause of HMDA's poor melting behaviour, the material was analysed using differential scanning calorimetry (DSC) under a temperature ramp of 10 °C min^{-1}. The resulting trace can be seen in Figure 4.5. An endothermic melting peak is evident at the expected temperature of approximately 45 °C, but no boiling peak is present. Instead there is a shallow, broad endothermic peak at around 100 °C which is likely to be due to evaporation of absorbed water, and another endothermic peak at roughly 180 °C which has the

Figure 4.4: Photo of HMDA after melting in an oil bath at 60 °C*. The material remained cloudy and formed a solid crust around the rim of the vial.*

characteristic shape for sublimation.[191] To try and mitigate these problems, a new batch of HMDA was purchased, as the previous batch had been stored in ambient conditions for several years and may have expired. The DSC trace for the new batch is also shown in Figure 4.5, and it can be seen that although the melting peak is sharper and there appears to be no absorbed moisture, sublimation is still observed. On melting a sample of this batch in an oil bath, the material remained cloudy, even when raised above 100 °C to eliminate any absorbed water. Lastly, HMDA was melted under a nitrogen atmosphere to prevent moisture absorption, but as this still produced cloudy results, the attempt to use HMDA as the excess material in the experiment was abandoned.

As the problems with using HMDA as an excess material revolved around an inability to melt it without unwanted side-effects, there was a proposal to instead use a diamine that is already liquid at room temperature: isophorone diamine, or IPDA, which also reacts with DGEBA at low temperatures of around 60 °C. Unfortunately, even 5 wt.% of PES/PEES thermoplastic polymer was found to be insoluble in IPDA at all temperatures up to 160 °C (see Figure 4.6), so IPDA was deemed unsuitable for purpose.

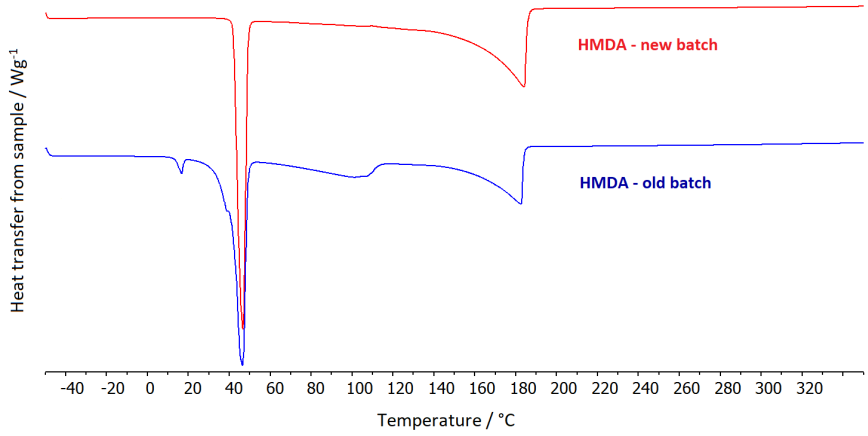

Figure 4.5: DSC traces of HMDA at a heating rate of $10\,^{\circ}\mathrm{C\,min^{-1}}$*. The blue trace shows a batch of HMDA that had been in storage for several years and the red trace shows a new batch purchased from Sigma Aldrich for this experiment.*

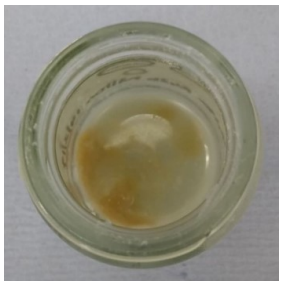

Figure 4.6: Photo of 5% of PES/PEES thermoplastic polymer mixed with IPDA. The thermoplastic was insoluble in IPDA at all temperatures tested up to $160\,^{\circ}\mathrm{C}$*, and instead clumped together.*

4.3.1.2 Epoxy excess

As attempts to use an amine excess in the model system had proved unsuccessful, an epoxy excess was instead chosen by default. It was not possible to purchase a deuterated version of DGEBA, and using HMDA as the limiting reactant meant that there would not be enough of it present to show sufficient contrast between the thermoplastic and partially cured epoxy phases in SANS measurements. Therefore, the only remaining option was to use a deuterated thermoplastic. A PES polymer with an M_n of $4000\,\mathrm{g\,mol^{-1}}$ and an M_w of $6000\,\mathrm{g\,mol^{-1}}$ was chosen. The low molecular weight increased the likelihood of dissolution in epoxy, and

allowed closer comparison with simulation, where the size of the polymers in the system is limited by computational efficiency.

For the model system to be useful for investigating concentration fluctuations, the PES had to be soluble in the partially cured epoxy component, and the system was required to be chemically stable before and during measurement. Deuterated materials are very expensive, so in order to run tests on the system, a non-deuterated PES with similar molecular weight to the deuterated version was synthesised according to the procedure in Section 4.2.3. This polymer had chlorine end groups and an M_n of $5452\,\mathrm{g\,mol^{-1}}$.

Solubility tests (detailed in Section 4.2.4) were carried out with the non-deuterated PES in pure DGEBA and partially cured epoxy with a 20:1 stoichiometric ratio of DGEBA to HMDA. In both cases, 20 wt.% of PES was observed to dissolve at temperatures of above 90 °C, which was sufficient in terms of deuterated material for SANS measurements. After cooling the mixtures to room temperature, the PES remained dissolved, as shown in Figure 4.7.

Figure 4.7: Photo of 20 wt.% *PES dissolved in pure DGEBA (left) and partially cured epoxy with a 20:1 stoichiometric ratio of DGEBA to HMDA (right). In both cases, the PES became soluble at* 90 °C*, and remained dissolved after cooling to room temperature.*

Next, the reactivity of the thermoplastic with unreacted epoxy groups was tested. It was unclear from the material data sheet whether the end groups of the detuerated PES were mostly chlorine or OD (hydroxyl OH groups where the

hydrogen is replaced with deuterium). From experience, it is known that chlorine does not react with epoxy groups, but that hydroxyl, and therefore OD, groups do. The end groups of the PES could have been determined by NMR, but this would have been expensive (as it would have to be purchased externally) and would have used up some of the valuable deuterated material, so the worst case scenario that the end groups were reactive OD was assumed instead.

Even if this were the case, the stoichiometry-controlled low cure extent suggests that reactive end groups would simply cause a chain extension of the PES rather than an incorporation of thermoplastic into a branched network. However, to ensure consistency between measurements, it was preferred that the PES molecules remained independent. Therefore, the reactivity of epoxy with hydroxyl groups (assumed to be the comparable to that of OD) was tested by mixing 20 wt.% of bisphenol S (the hydroxyl capped monomer of PES) with DGEBA, and running DSCs with heating rates of both $1\,^{\circ}\mathrm{C\,min^{-1}}$ and $10\,^{\circ}\mathrm{C\,min^{-1}}$. Both of these traces, shown in Figure 4.8, display an exothermic peak which can be safely assumed to represent the reaction of epoxy and hydroxyl groups. These peaks have an onset of approximately 150 °C, so to ensure the thermoplastic PES did not react with the epoxy in the model system, an upper temperature limit of 140 °C was adopted for measurements, as no reaction was observed below this temperature.

Once the model system had been chosen, a procedure for preparing samples was developed. A detailed description of this can be seen in Section 4.2, but a brief overview will be given here. DGEBA was melted to a liquid and left to cool to room temperature to become more viscous. Equal masses of HMDA and DGEBA were ground together to a paste in a pestle and mortar, and a subsample of this was added to pure DGEBA to give the correct stoichiometric ratio. The system was cured for 2 h at 60 °C, and PES could then be added as necessary by

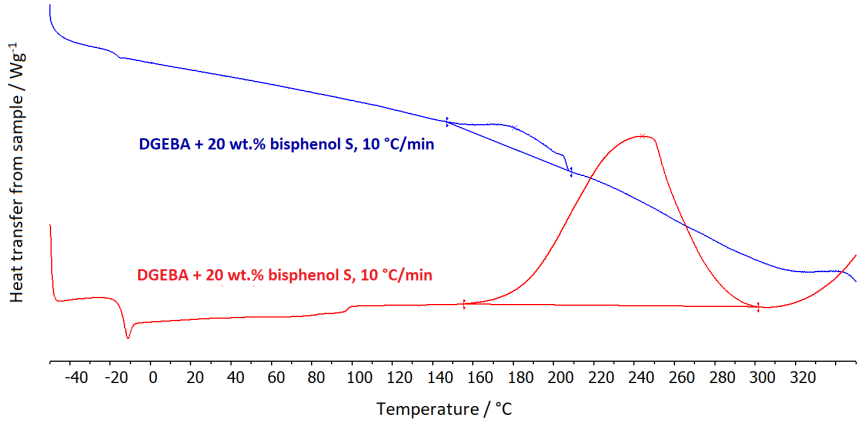

Figure 4.8: DSC traces for 20 wt.% *of bisphenol S in DGEBA at heating rates of* $1\,^{\circ}\mathrm{C\,min^{-1}}$ *(blue) and* $10\,^{\circ}\mathrm{C\,min^{-1}}$ *(red). An exothermic reaction peak for the epoxy and hydroxyl groups onsets at roughly* 150 °C *in both cases. The beginning of the epoxy self-reaction peak can also be seen at approximately* 320 °C *for the sample with the* $10\,^{\circ}\mathrm{C\,min^{-1}}$ *heating rate.*

dissolving at 90–100 °C.

It was noticed that after approximately 2 weeks of storing partially cured epoxy samples at room temperature, the viscosity increased significantly so that the materials appeared solid. These solid samples were found to be soluble in dichloromethane, and upon heating to 160 °C, they became rubbery. These observations suggest that the materials had not gelled, but that a slow chemical reaction had taken place that raised the glass transition temperatures (T_g) of the samples to above room temperature over the course of a few weeks.

The nature of this reaction could not be determined. DSCs traces of two partially cured epoxy samples with 40:1 DGEBA to HMDA stoichiometic ratios were measured immediately after preparation, and are given in Figure 4.9. The first exothermic peak observed is the epoxy self-reaction at above 320 °C, so these traces show no evidence of a reaction that could take place at room temperature. Near-infrared spectroscopy was also performed on one of these samples before and after storage to see if there had been any change in the presence of reactive

groups (see Figure 4.10), but any differences between the spectra were smaller than the expected 5 % measurement uncertainty.

One possibility was that the changes in the sample could be due to further cure caused by an epoxy-self reaction, catalysed by tertiary amines in the reacted HMDA. Tertiary amines can act as a Lewis acids, which cure epoxy resins by catalytically induced ionic polymerisation,[192]. However, the DSC and near-infrared traces show little evidence of this. In the interest of developing a working system before the deadline of the neutron beamline date, a decision was made to mitigate the effects of any undesired reactions rather than trying to explain them.

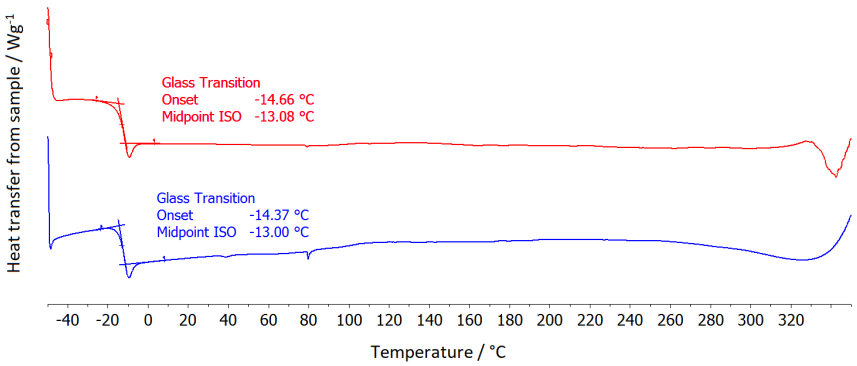

Figure 4.9: DSC traces of two partially cured epoxy samples with 40:1 DGEBA to HMDA stoichiometic ratios, measured immediately after preparation. The onset of the glass transition in both cases is approximately −14 °C, and the epoxy self-reaction is the lowest temperature exothermic peak with an onset of approximately 320 °C. The sharp dip at the end of the red trace is likely to be an instrument artefact.

Storage tests

Storage tests were carried out to find out whether and under what conditions the material for SANS measurements could be stored inertly. Samples were prepared with 40:1 and 20:1 stoichiometric ratios of DGEBA to HMDA, with 0 %, 10 %

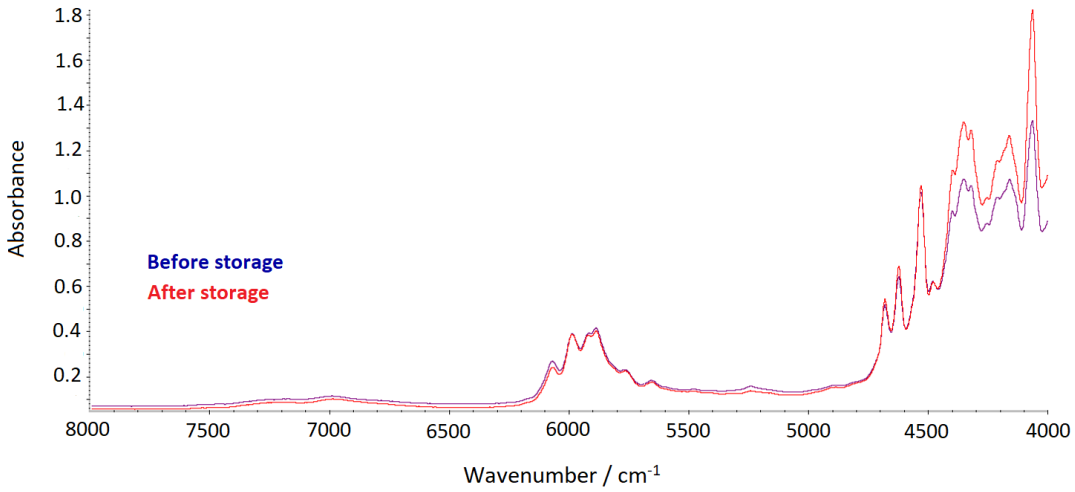

Figure 4.10: Near-infrared spectra of partially cured epoxy samples with a 40:1 stoichiometric ratio of DGEBA to HMDA before (blue) and after (red) storage. Little difference can be seen between the traces, apart from at the the low wavenumber end where more uncertainty is expected due to baseline corrections.

and 20 % of added PES. Repeat batches and subsamples were made for all formulations without PES. The detailed methodology used for running these tests can be found in Section 4.2.6. DSC traces were measured for each of the samples immediately after preparation, and after 66 days in the following conditions: in a freezer at −28 °C, under ambient conditions, and in a desiccator at room temperature. For some of the samples without PES, a measurement was also taken after 10 days in ambient conditions. The temperatures of the glass transition onsets for each of the samples are given in Table 4.1.

It is clear that all samples were relatively stable when stored in the freezer, but significant increases in T_g were observed for the samples stored at room temperature, both under ambient conditions and in the desiccator. Therefore, it was determined that material for the SANS experiments could be made in advance, as long as the samples were stored in a freezer after preparation.

It was observed that the samples with a 20:1 DGEBA to HMDA ratio had a

Stoichiometric DGEBA:HMDA ratio	PES %	Batch	Repeat	Onset temperature of glass transition/ °C				
				Before storage	After storage (66 days unless stated otherwise)			
					Freezer	10 days ambient	Ambient	Desiccator
40:1	0	1	1	-20.15	-20.09	-17.09	-17.06	-17.61
			2		-20.47	-	-16.52	-16.00
		2	1	-19.77	-19.46	-16.80	-16.40	-15.96
			2		-19.87	-	-16.83	-15.64
	10	1	1	-17.29	-16.54	-	-10.82	-11.32
	20	1	1	-12.42	-12.04	-	-7.57	-6.88
20:1	0	1	1	-18.63	-18.26	-14.07	5.97	-
			2		-18.33	-	2.05	-
		2	1	-17.65	-17.90	-12.73	0.60	-
			2		-17.64	-	-1.89	-
	10	1	1	-15.64	-15.60	-	5.58	-
	20	1	1	-9.66	-7.52	-	4.87	-

Table 4.1: T_gs measured during storage tests of partially cured epoxy with and without PES. The measurement error on the DSC is approximately $\pm 1\,^{\circ}\mathrm{C}$. *Measurements were taken immediately after preparation and after* 66 days *storage in various conditions (in a* $-28\,^{\circ}\mathrm{C}$ *freezer, under ambient conditions, and in a desiccator at room temerpature). DSCs were also measured for four samples after* 10 days *in ambient conditions. Values of T_g are not given for the desiccator samples with a 20:1 DGEBA to HMDA ratio, as the traces were too flat to allow the glass transition to be analysed.*

slightly higher initial T_gs than the samples with a 40:1 ratio. This is expected, because they should have a higher cure extent and larger molecules which require more energy to move (see Section 1.3.2). A larger increase in T_g was seen when adding PES thermoplastic, which was expected for the same reason. Only one distinct T_g was observed for each sample, suggesting complete miscibility of the epoxy and thermoplastic components.

As a matter of interest, it is also apparent that there was a greater increase in the T_gs of the samples with the 20:1 DGEBA to HMDA ratios than the 40:1 ratios after storage under ambient conditions. Therefore, the more highly cured samples were less stable, which corroborates the theory that there could be an epoxy self-reaction catalysed by tertiary amines, as more of these would have been present in the samples with higher cure extents.

There was concern that whatever chemical changes taking place at room temperature would be accelerated by the high temperatures of the ramp in the SANS measurements, and alter the system during the experiment. Therefore, subsamples of the material prepared for the storage tests (and kept in the freezer) were placed in an oven and exposed to the full temperature ramp expected during the SANS measurements. All T_gs remained constant within experimental error for these measurements, so it was concluded that no significant chemical changes would take place in the samples during the SANS experiments.

4.3.2 Characterisation of the system

20 g of partially cured epoxy was prepared for the SANS samples in each of 80:1, 40:1, 20:1 and 10:1 stoichiometric ratios of DGEBA to HMDA, according to the method described in Section 4.2.8. Assuming complete reaction of the HMDA, which is expected as it was used as a limiting reactant, these ratios correspond to cure extents of 2.5 %, 5 %, 10 % and 20 % respectively. These low levels of

cure were used for two reasons. Firstly, the viscosity of epoxy resins is very high, especially after the addition of thermoplastic, and less cured material is easier to handle. Secondly, remaining well below the gel point of the material allows the system to remain in equilibrium with a small cluster size, which is simpler to simulate computationally so that comparisons between model and experiment can be made.

Although the overall cure extent is known, the sizes of the clusters and the resulting molecular weight distribution are unknown. These can be estimated theoretically (see Section 1.3.1), but such calculations ignore factors like steric hindrance, cure temperature and relative reactivity of amine hydrogens.

Therefore, an attempt to determine the molecular weight distribution of the partially cured epoxy samples via gel permeation chromatography was made.

4.3.2.1 Gel permeation chromatography

Gel permeation chromatography (GPC) is an analytical technique that measures the amount of material with each molecular weight within a sample. The analyte is dissolved in a solvent, filtered, and passed through a column packed with porous beads. The amount of material exiting the column is measured against time, with smaller particles spending more time captured within pores and therefore having a longer retention time. The characteristic directly measured by GPC is the hydrodynamic volume, but by calibrating the peaks against a known standard, these values can be converted to molecular weight.

In the case of our samples of DGEBA cured with a limited amount of HMDA, no appropriate calibration standard was available, and a non-optimal PMMA (poly(methyl methacrylate)) standard was used instead. However, as we know that all amine groups in the sample should have reacted, the peak with the longest

retention time and an apparent M_n of $178\,\mathrm{g\,mol^{-1}}$ can be assigned to sole DGEBA molecules, with a known molecular weight of $340\,\mathrm{g\,mol^{-1}}$. The peak with the next longest retention time and an apparent M_n of $1235\,\mathrm{g\,mol^{-1}}$ can be assigned to a cluster of one HMDA and four DGEBAs, with a known molecular weight of $1476\,\mathrm{g\,mol^{-1}}$. The peak with the third longest retention time and an apparent M_n of $2595\,\mathrm{g\,mol^{-1}}$ can be asssigned to a cluster of two HMDA and seven DGEBAs, with a known molecular weight of $2612\,\mathrm{g\,mol^{-1}}$. The area of each peak represents the number of molecules with that molecular weight.

The partially cured epoxy samples were found to be soluble in both chloroform and tetrahydrofuran (THF). GPC traces were first measured using a chloroform solvent, but only one peak, likely corresponding to sole DGEBA molecules, was present in each sample. This suggested that larger clusters were insoluble in chloroform and were therefore filtered out before measurement. In order to produce more useful data, the procedure was repeated in a THF solvent, and the resulting traces are given in Figure 4.11. Here, we can see two peaks in the samples with 2.5 %, 5 % and 10 % cure, with the relative areas of the peaks corresponding to clusters containing one HMDA to no HMDA molecules increasing with cure extent. In the sample with 20 % cure, we can also see a third peak, indicating the presence of clusters containing two HMDA molecules.

These results allow us to determine the relative quantities of each cluster size in the samples with different cure extents. It is possible that larger, insoluble clusters were also initially present and filtered out, but this seems unlikely given the relative sizes of the visible peaks. The calculated percentages of each cluster size present are shown in Table 4.2 (by number of molecules) and Table 4.3 (by weight). This data is also displayed graphically in Figure 4.12. The M_n and M_w for each of the samples are given in Table 4.4, and a plot of M_n against M_w is shown in Figure 4.13. Both M_n and M_w increase linearly with cure extent, and M_w has a higher rate of increase because the presence of large molecules has a

greater impact on M_w than M_n.

The values of the percentage of each cluster size in the system (shown in Table 4.2) were compared against theoretical predictions from the Stockmayer model of gelation, described in Section 1.3.1.[134] In general, the theoretical model makes reasonable predictions with the correct trends, although it underestimates number of molecules with low molecular weight and overestimates the number with high molecular weight, with larger discrepancies for the samples with higher cure extent. These inconsistencies may be partially explained by uncertainty in the GPC measurements and analysis, where some user interpretation was required to determine the beginning and end points of each peak. This was more subjective for the higher molecular weight peaks, which are more important for higher cure extent samples. Discrepancies may also be caused by errors in the theoretical approach, due to neglected variables such as steric hindrance, cure temperature, and relative reactivities of primary and secondary amine hydrogens. Stockmayer's model also includes approximations that mean it is only valid well below the gel point, so the predictions are likely to be more accurate at lower cure extents.

Number of HMDA molecules in cluster	Molecular weight of cluster / $g\,mol^{-1}$	Percentage by number of clusters of each size for each cure extent							
		2.5 % cure		5 % cure		10 % cure		20 % cure	
0	340	96.3	93.8	92.5	88.1	86.4	77.2	75.8	59.5
1	1476	3.7	5.6	7.5	9.9	13.6	15.6	17.6	19.0
2	2612	0	0.5	0	1.6	0	4.6	6.6	8.8

Table 4.2: Percentage by number of clusters of each size for each cure extent, measured by GPC (in the left column) and compared against theoretical predictions using Stockmayer's model for gelation (in the right column).[134]

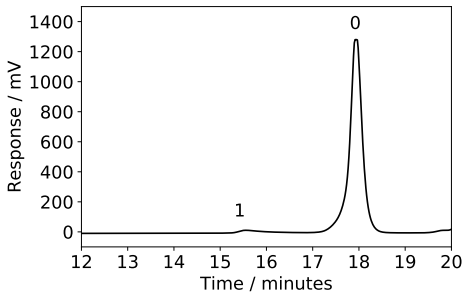

(a) 2.5 % cure

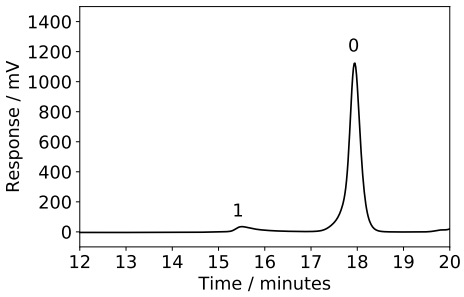

(b) 5 % cure

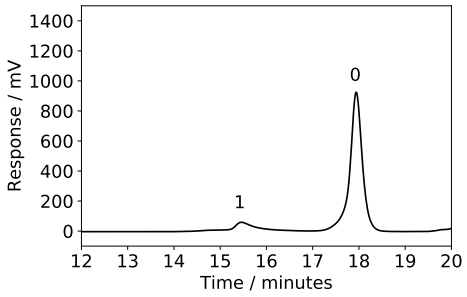

(c) 10 % cure

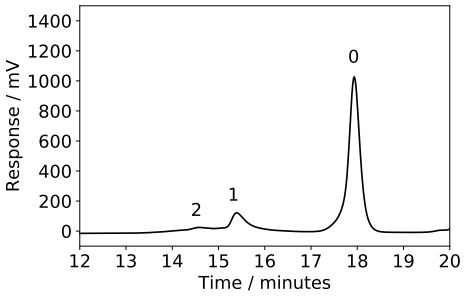

(d) 20 % cure

Figure 4.11: GPC traces for partially cured epoxy samples with each cure extent. Peaks are labelled by the number of HMDA molecules in the cluster size they represent.

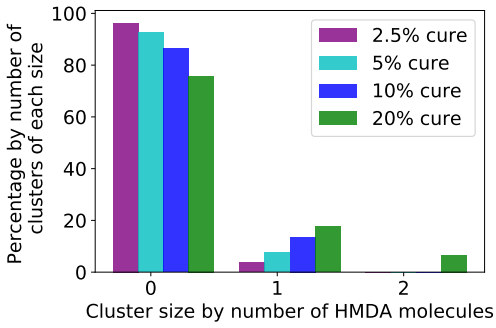

(a) Percentage by number of molecules

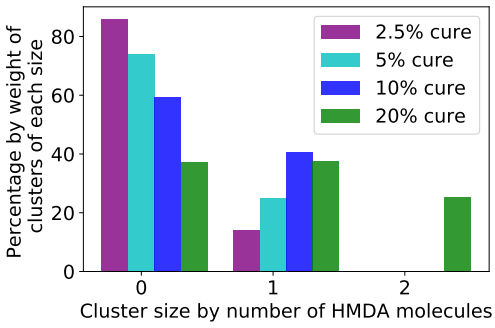

(b) Percentage by weight

Figure 4.12: Bar charts showing the percentage by (a) number of molecules and (b) weight of clusters of each size for cure extent, measured by GPC.

Number of HMDA molecules in cluster	Molecular weight of cluster / g mol^{-1}	Percentage by weight of clusters of each size for each cure extent			
		2.5 % cure	5 % cure	10 % cure	20 % cure
0	340	85.8	74.1	59.4	37.3
1	1476	14.2	25.9	40.6	37.5
2	2612	0	0	0	25.2

Table 4.3: Percentage by weight of clusters of each size for each cure extent, measured by GPC.

DGEBA:HMDA ratio	Cure extent	M_n / g mol^{-1}	M_w / g mol^{-1}
80:1	2.5 %	382	501
40:1	5 %	425	635
20:1	10 %	495	801
10:1	20 %	691	1339

Table 4.4: Number and weight average molecular weights for the cluster distributions in samples with each DGEBA to HMDA ratio and cure extent, measured by GPC.

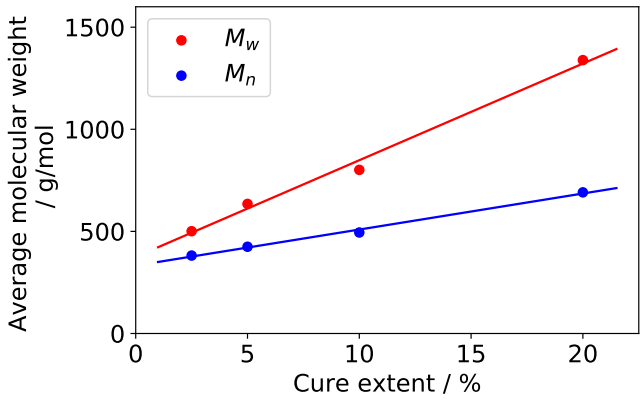

Figure 4.13: Number and weight average molecular weights for the cluster distributions in samples with each cure extent, measured by GPC. Both M_n and M_w increase linearly with cure extent, with M_w exhibiting a higher rate of increase.

4.3.2.2 Rheology

In addition to GPC measurements, the viscosities of the partially cured epoxy samples were also characterised using rheology to allow comparison between the different cure extents. Pure uncured DGEBA, and samples with the previously mentioned 2.5 %, 5 %, 10 %, and 20 % cure extents were studied. A series of viscosity measurements was taken for each sample at 5 °C temperatures intervals, between limits imposed by the range of viscosities the rheometer was capable of measuring. A frequency sweep was used for each measurement, and the viscosities quoted are the mean values for the flat portion of the resulting traces.

The viscosities measured for each sample at each temperature can be seen in Figure 4.14, noting the logarithmic scale on the viscosity axis. Viscosity is observed to rise increasingly rapidly with cure extent, as would be expected because larger and more branched molecules require more energy to flow past each other. For all samples, viscosity decreases with temperature, which makes sense as more energy is being supplied to drive the cooperative motions that allow molecules to flow (see Section 1.3.2 for background information).

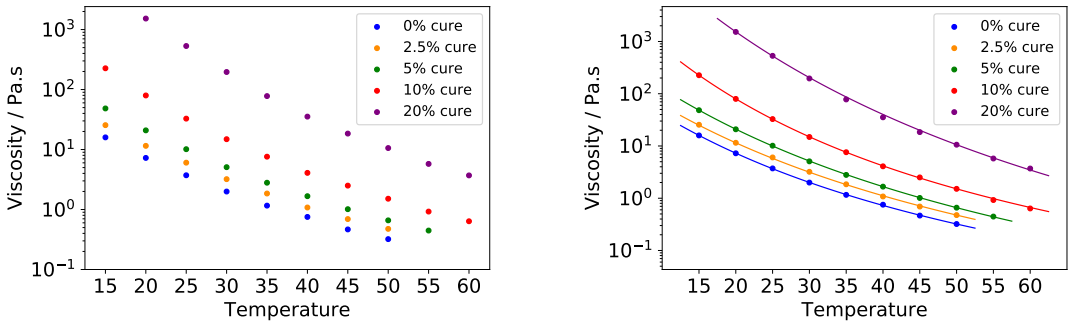

(a) Raw data *(b) Data with WLF-fitted curves*

Figure 4.14: Viscosity measurements at a range of temperatures for partially cured epoxy samples with various cure extents. Viscosity is presented on a logarithmic scale. (a) shows the raw data and (b) shows the fit with empirically determined WLF parameters.

A commonly-used expression to characterise viscosity curves is the Williams-Landel-Ferry (WLF) equation, given by Equation 4.9 where $\mu(T)$ is the viscosity at temperature T, and μ_r is the viscosity at a chosen reference temperature T_r. C_1 and C_2 are empirical parameters determined by curve fitting of experimental data. This equation allows viscosity to be predicted for any arbitrary temperature T for an amorphous material above its T_g.[193]

$$\mu(T) = \mu_r \exp\left(\frac{-C_1(T - T_r)}{C_2 + T - T_r}\right) \tag{4.9}$$

The WLF equation relies on the concept of time-temperature superposition (a principle which states that the viscosity behaviour of polymers is equivalent as a function of either time or temperature), which is only valid for homogeneous systems. In addition to allowing an indirect measure of the amount of cure in the system and giving an indication of the range of materials that can be easily worked with at each temperature, viscosity measurements can therefore also highlight compositional inhomogeneities (such as concentration fluctuations or phase separation) via deviations from the WLF curve.[194]

Curve fitting to the WLF expression was carried out by non-linear regression for each of the samples of partially cured epoxy, using a reference temperature of 50 °C in all cases. The calculated fit parameters are given in Table 4.5, and the resulting curves are shown in Figure 4.14b and 4.15. It is clear that the fits are generally very good and the data follows WLF behaviour. This suggests that the polymerised molecules within the partially cured material had mixed homogeneously with the unpolymerised epoxy monomers, and that there was no segregation by particle size.

In order to provide more useful data, similar experiments could be carried out after blending the PES thermoplastic with the partially cured epoxy. Here, checking for miscibility via deviations from the WLF equation fit would poten-

tially highlight concentration fluctuations within the blends. However, this was not possible in this work, as the high viscosities of the materials prevented measurements from being taken at a suitable range of temperatures without installing an oven onto the rheometer.

Fit parameter	Cure extent				
	0 %	2.5 %	5 %	10 %	20 %
μ_r / Pa s	0.321	0.476	0.660	1.51	10.6
C_1	7.7 ± 0.1	8.6 ± 0.3	9.5 ± 0.1	8.67±0.03	13.6 ± 0.6
C_2	104 ± 1	111 ± 3	112 ± 1	95.6 ± 0.2	112 ± 4

Table 4.5: WLF fit parameters determined by non-linear regression in OriginPro for samples of partially cured epoxy with various cure extents. A reference temperature of $T_r = 50\,^{\circ}\mathrm{C}$ was used for all samples.

4.3.3 SANS measurements

Once the model system had been chosen and characterised, samples were prepared for small-angle neutron scattering measurements using the procedure outlined in Section 4.2.8. The design of the sample holders developed for this work can be seen in Section 4.2.7.

Glass transition temperatures were measured for each of the samples of partially-cured DGEBA before and after storage to check that no changes had occurred. A further measurement was taken after heating the PES thermoplastic with the partially-cured DGEBA to ensure full dissolution with presence of only a single glass transition temperature. Results for these measurements are given in Table 4.6.

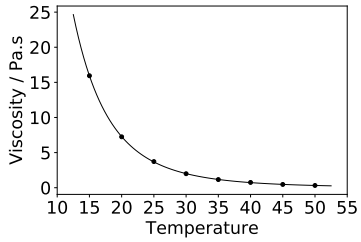

(a) 0 %, linear scale.

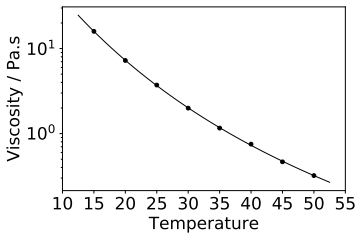

(b) 0 %, logarithmic scale.

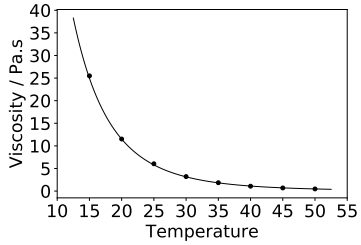

(c) 2.5 %, linear scale.

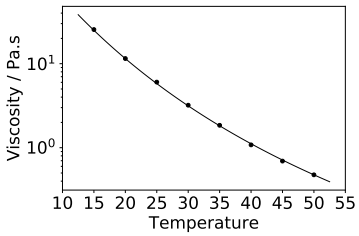

(d) 2.5 %, logarithmic scale.

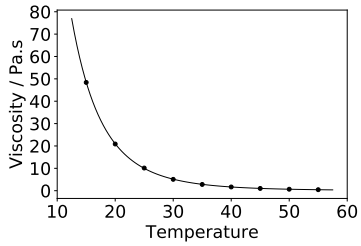

(e) 5 %, linear scale.

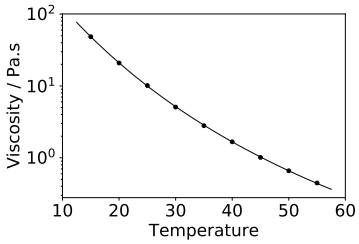

(f) 5 %, logarithmic scale.

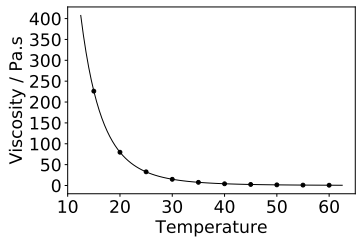

(g) 10 %, linear scale.

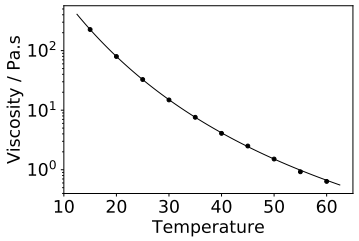

(h) 10 %, logarithmic scale.

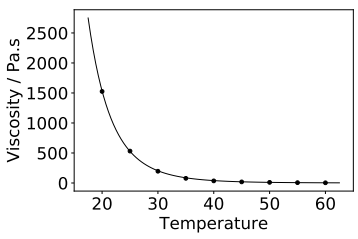

(i) 20 %, linear scale.

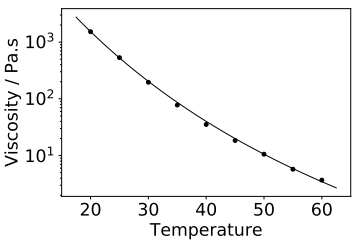

(j) 20 %, logarithmic scale.

Figure 4.15: WLF curve fits calculated by non-linear regression for samples with partially cured epoxy samples with cure extents of 0 %, 2.5 %, 5 %, 10 % and 20 %. Fits are shown on both a linear and logarithmic scale for each sample, with raw data represented by points and fitted curves by smooth lines.

Cure extent	Onset temperature of glass transition / °C		
	Partially-cured DGEBA		After dissolving PES
	Before storage	After storage	
2.5 %	-18.72	-18.29	-6.48
5 %	-17.62	-17.49	-5.36
10 %	-15.72	-15.64	-1.52
20 %	-11.27	-11.38	7.62

Table 4.6: Glass transition temperatures measured by DSC for the samples of partially-cured epoxy before and after 3 weeks *storage in a* −28 °C *freezer, and after dissolution of* 20 wt.% *deuteratured PES thermoplastic. Measurement uncertainties are approximately* ± 1 °C *in all cases.*

Details of the SANS measurement procedure can be found in Section 4.2.9. Scattering intensity was measured for a q range of 0.04 Å^{-1} to 0.57 Å^{-1}. Four samples were used, with cure extents of 2.5 %, 5 %, 10 % and 20 % respectively, each containing 20 wt.% of deuterated PES. Measurements were made at 60 °C, 80 °C, 100 °C, 120 °C and 140 °C, before taking a final measurement at 60 °C to determine whether the systems had changed from their initial states during heating.

The data was treated by subtracting the incoherent background, and then normalising between traces, using a reference at a high q value of approximately 0.4 Å^{-1} where the traces are relatively smooth and featureless. This normalisation was necessary because the design of the sample holders meant that it was impossible to prepare samples with consistent thickness and path length.

The general shapes of all the traces are similar, with a typical plot of scattering intensity $I(q)$ against q given by Figure 4.16. $I(q)$ decreases steeply with q at low q, then there is a peak at 0.02 Å^{-1}, and a shallow decrease of $I(q)$ with q at higher q values, which is expected for scattering from concentration fluctuations.

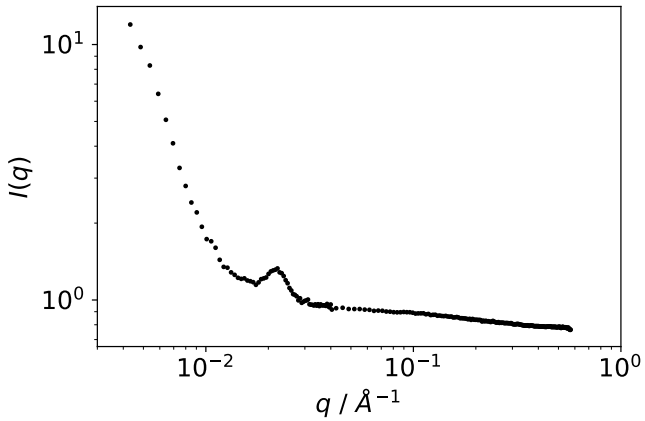

Figure 4.16: The general shape of the plots of scattering intensity $I(q)$ against q gained from SANS of a blend of partially cured epoxy and deuterated PES. The sample represented here was prepared with a 10:1 stoichiometric ratio of DEGBA to HMDA, corresponding to a cure extent of 20 %*, and was measured at* 60 °C*. Both axes are plotted on a logarithmic scale.*

4.3.3.1 Low *q* behaviour

First, the low q behaviour of the blends will be examined. Typical traces of $I(q)$ against q for the initial low q slope can be seen in Figure 4.17, where each plot shows a range of measurement temperatures with the same sample. Similar trends are seen for all cure extents. In all samples, it is clear that as temperature increases, scattering intensity decreases, suggesting that inhomogeneities within the material are becoming less distinct. This is indicative of blends exhibiting upper critical solution temperature (UCST) behaviour that become more miscible at higher temperatures (see Section 1.2.4.1). The final repeat measurements at 60 °C return to roughly the same intensity values as the initial 60 °C measurements, suggesting that this effect is an equilibrium behaviour and that no chemical changes are taking place within the samples.

This evidence of UCST-like behaviour was surprising, because other reports of phase separation in DGEBA/PES blends have shown a lower critical solution

temperature (LCST), where the blends become more miscible at low temperatures and phase separated at higher ones.[43,127] However, the previous studies used significantly different systems to this one, with much higher molecular weight PES (M_n ranging from 14 700 g mol^{-1} to 23 800 g mol^{-1} as opposed to the 4000 g mol^{-1} here) and diamine curatives with different chemical structures. In particular, the presence of high molecular weight polymers would be expected to increase the prevalence of LCST-like behaviour due to compressibility effects.[10]

It was expected that the materials used in this study would exhibit behaviour according to the Random Phase Approximation (RPA) for slightly inhomogeneous blends, as described in Section 4.1.2. The RPA states that at zero q, the structure factor $S(0)$ can be given by Equation 4.10, where ϕ_A and ϕ_B are the volume fractions of each component, N_A and N_B are their degrees of polymerisation and χ is the Flory-Huggins interaction parameter.

$$\frac{1}{S(0)} = \frac{1}{\phi_A N_A} + \frac{1}{\phi_B N_B} - 2\chi \tag{4.10}$$

Scattering intensity $I(q)$ is directly proportional to the structure factor $S(q)$, so extrapolating a Zimm plot of $1/I(q)$ against q^2 as a straight line to the limit of $q^2 = 0$ allows the χ interaction parameter to be determined from the $1/I(0)$ intercept. By evaluating systems with a range of temperatures and cure extents, as used in this experiment, the temperature and composition dependence of the χ parameter can also be investigated. Zimm plots for all of the experimental samples can be seen in Figure 4.18. One graph is given for each cure extent, with measurements at multiple temperatures plotted for each sample. Best fit straight lines are presented using a least-squares approach at low q.

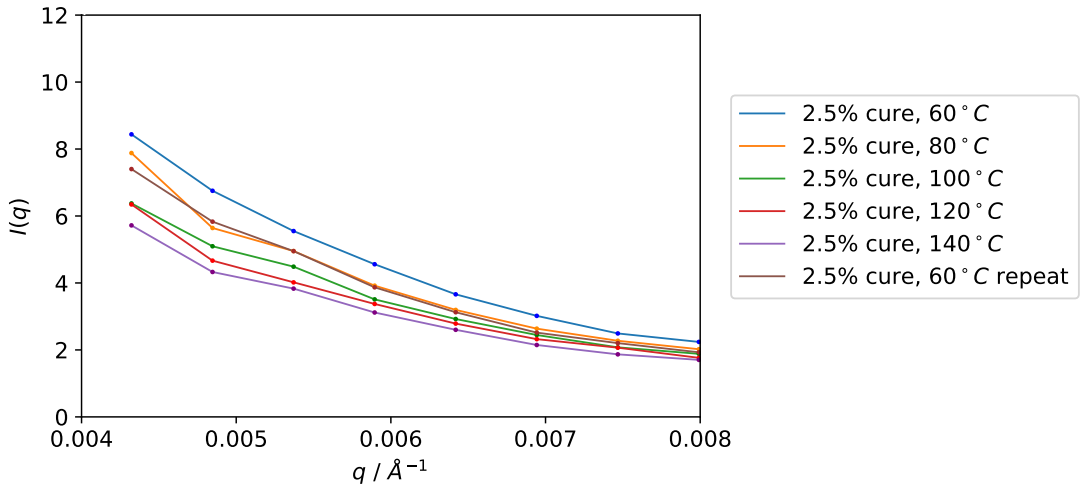

(a) 2.5 % cure.

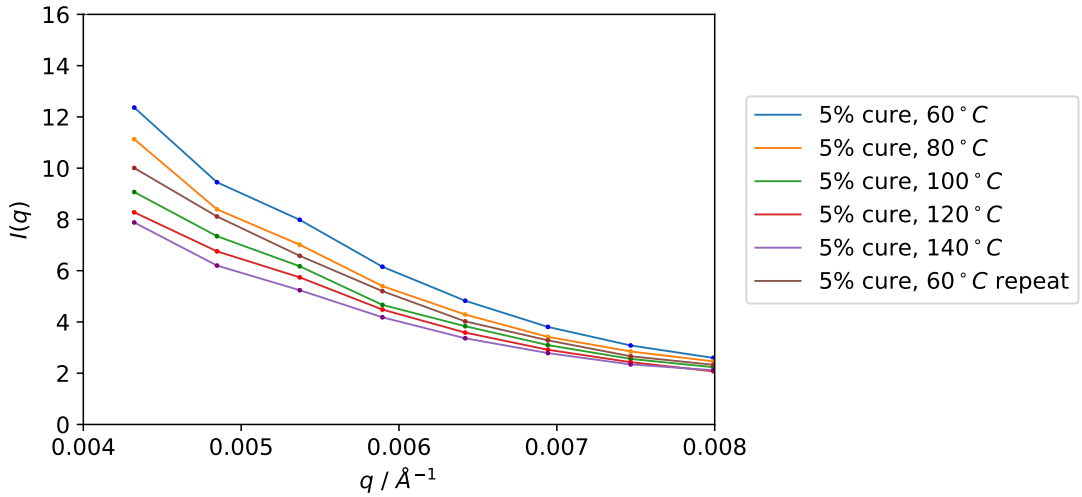

(b) 5 % cure.

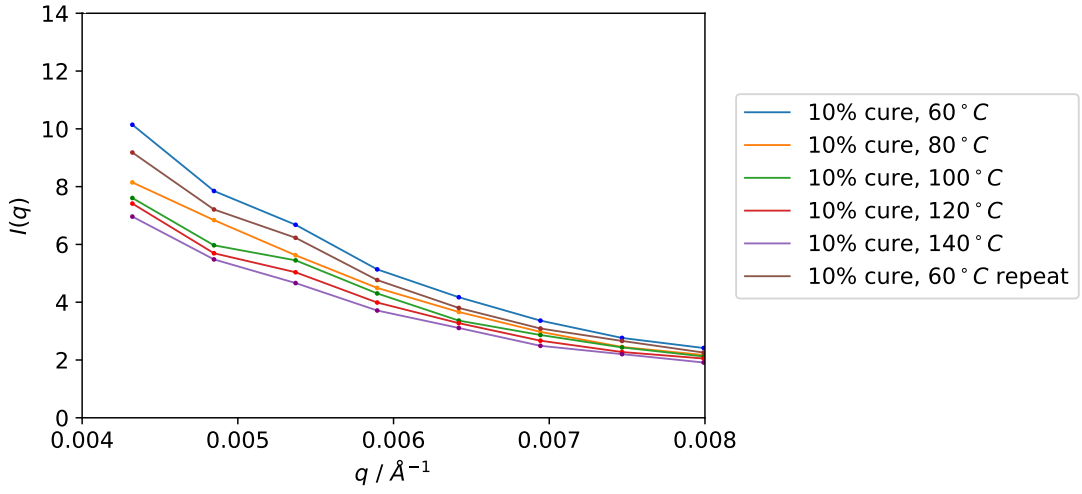

(c) 10 % cure.

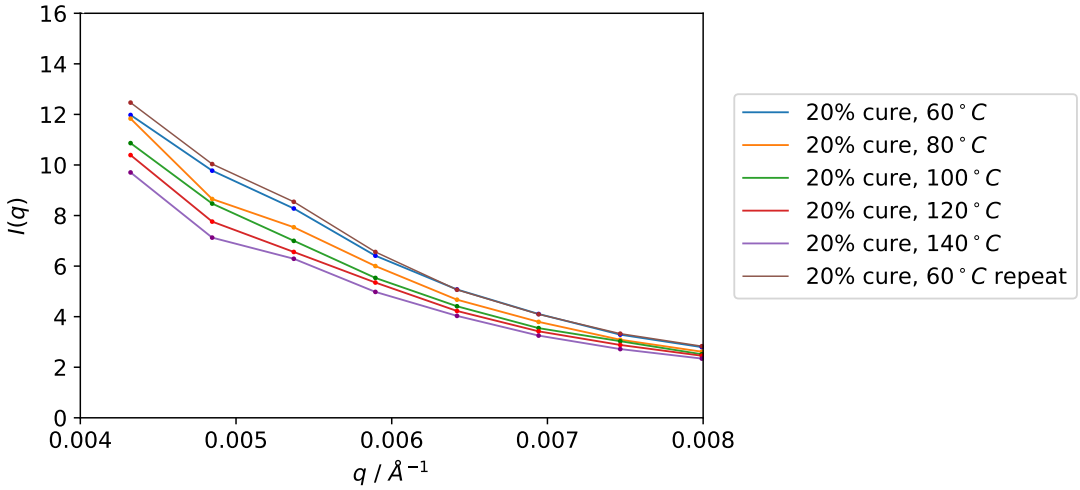

(d) 20 % cure.

Figure 4.17: $I(q)$ against q for polymer blends with a range of cure extents, focussing on the low q behaviour. Values are given for measurements at a range of increasing temperatures at 20 °C intervals between 60 °C and 140 °C, as well as a repeat measurement at 60 °C after completion of the temperature ramp. Data are given by points, and lines are drawn directly between these without fitting as a guide to the eye.

Unfortunately, in addition to the deviations from the straight line fits at the high q end of the graphs (expected because the RPA is only valid in the low q limit), there is also a deviation for the two measurements at lowest q. It is possible that this could be caused by the tail end of another peak in the trace at a q value lower than the experimental q_{min} of 0.04 Å^{-1}. In any case, the inconsistency with a linear trend at low q values makes any predictions of the $1/I(q)$ intercept invalid, so no meaningful χ parameters could be gained from this experiment. In order to make accurate estimates of χ, additional measurements at lower q values would be required in order to locate the linear regime and allow extrapolation of the fit to zero q.

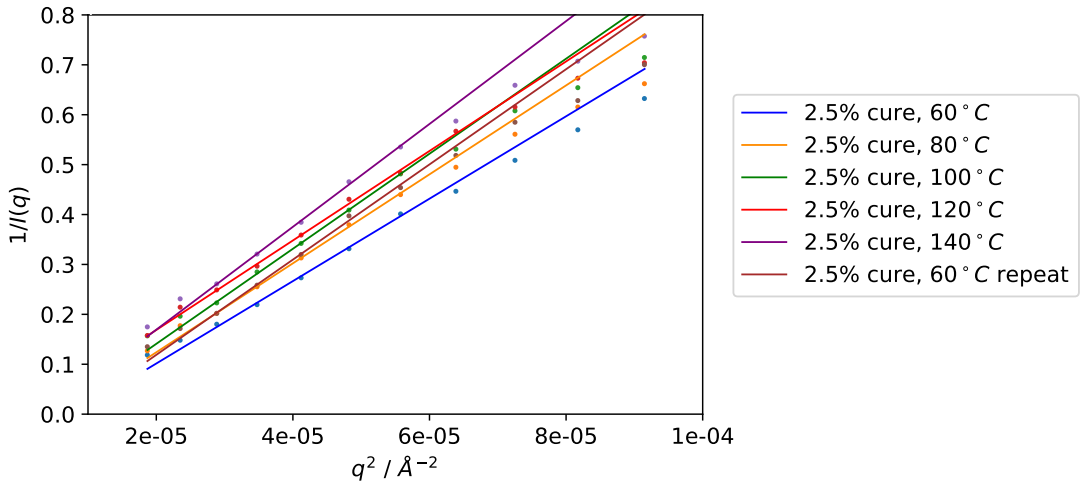

(a) 2.5 % cure.

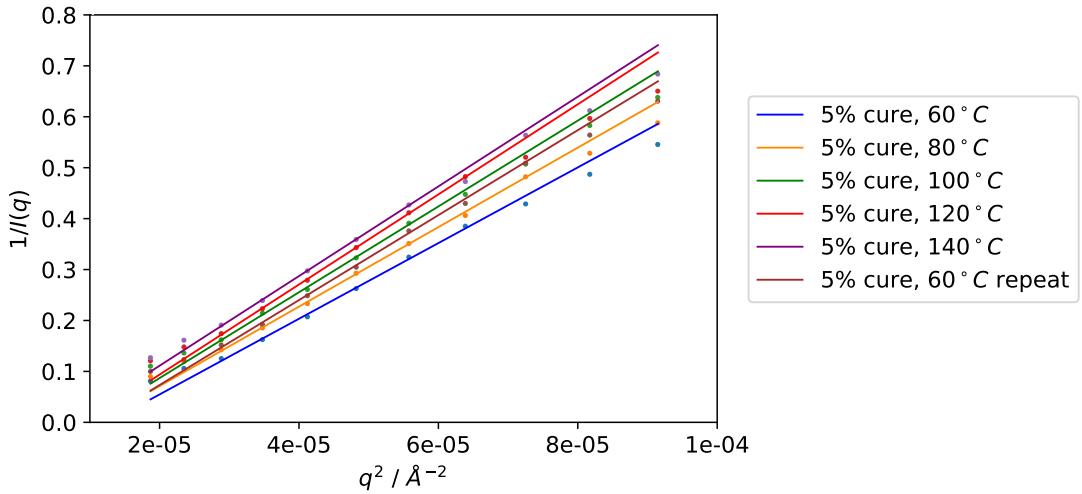

(b) 5 % cure.

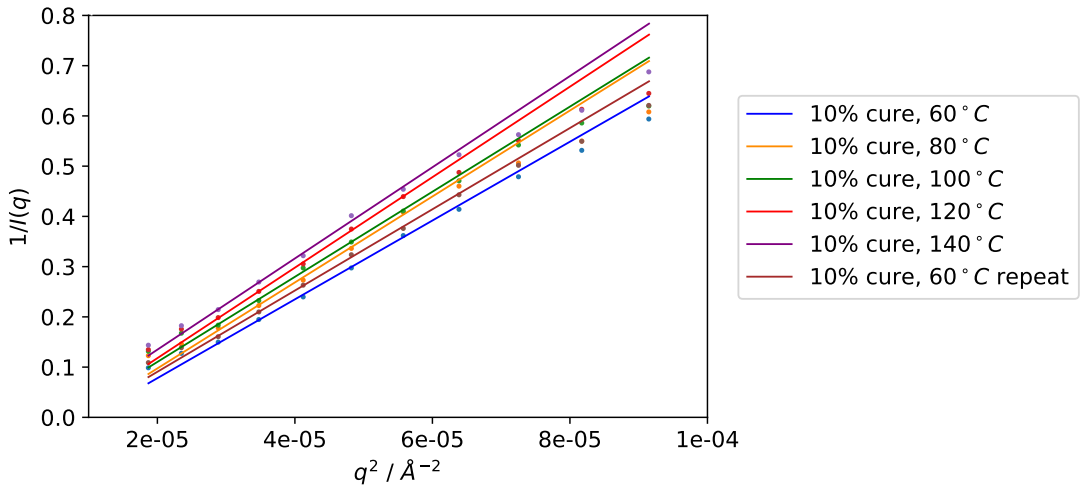

(c) 10 % cure.

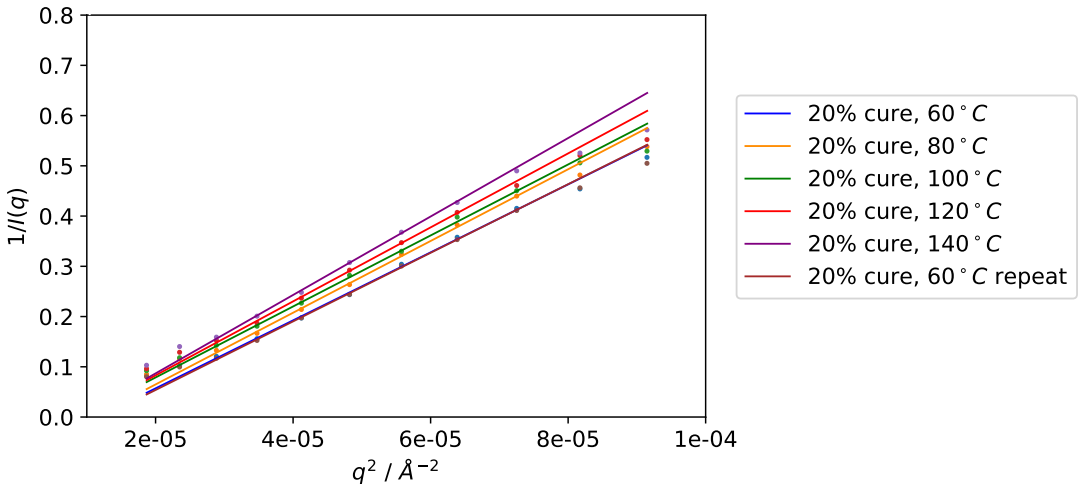

(d) 20 % cure.

Figure 4.18: Zimm plots of $1/I(q)$ against q^2 for samples with various cure extents at a range of temperatures.

4.3.3.2 Peak at $q = 0.02\,\text{Å}^{-1}$

In addition to the low q behaviour, the other interesting feature of the SANS traces is the peak at $0.02\,\text{Å}^{-1}$, present in all samples except for the highest temperature measurement (140 °C) of the sample with the lowest cure extent (2.5 %). Traces of $I(q)$ against q focussing on this peak are given in Figure 4.19.

In all traces, there is an overall increase in scattering intensity as temperature decreases, meaning that inhomogeneities become larger and more distinct at lower temperatures. The effect of changing the temperature is more pronounced in the lower cure samples. Due to the difference in lengthscales involved, this peak represents a distinct effect from the UCST-like behaviour observed at low q. As the peak occurs at approximately 30 nm, on the order of ten molecules, it is likely to be caused by molecular organisation or microphase separation, but the exact

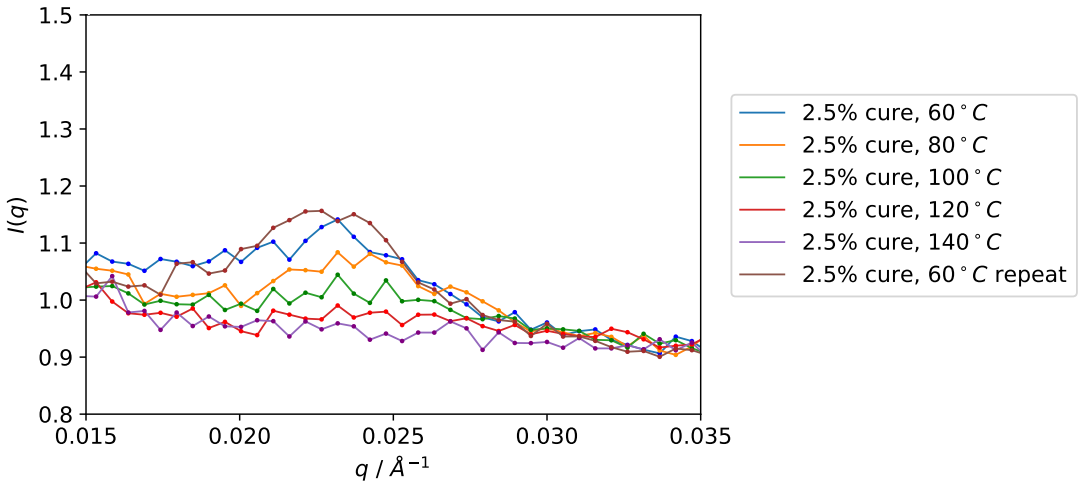

(a) 2.5 % cure.

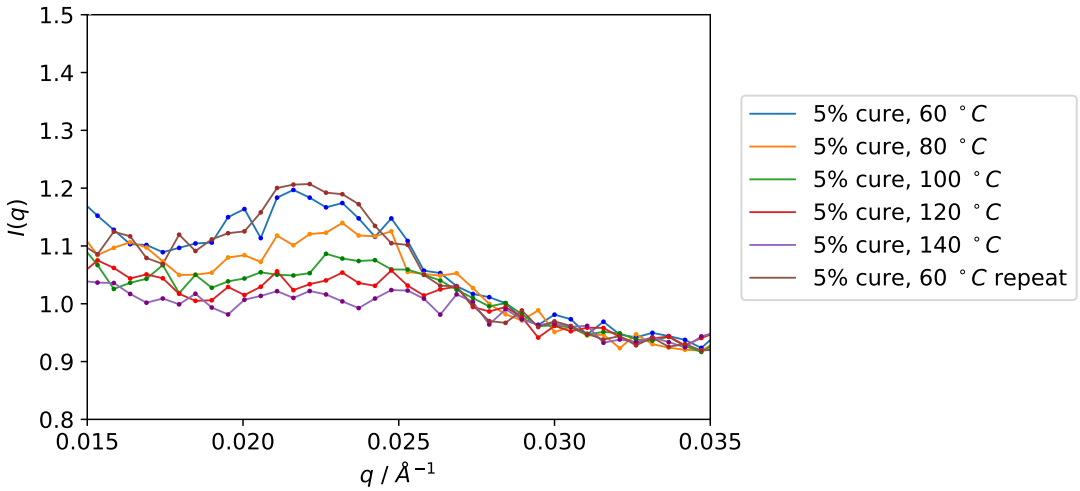

(b) 5 % cure.

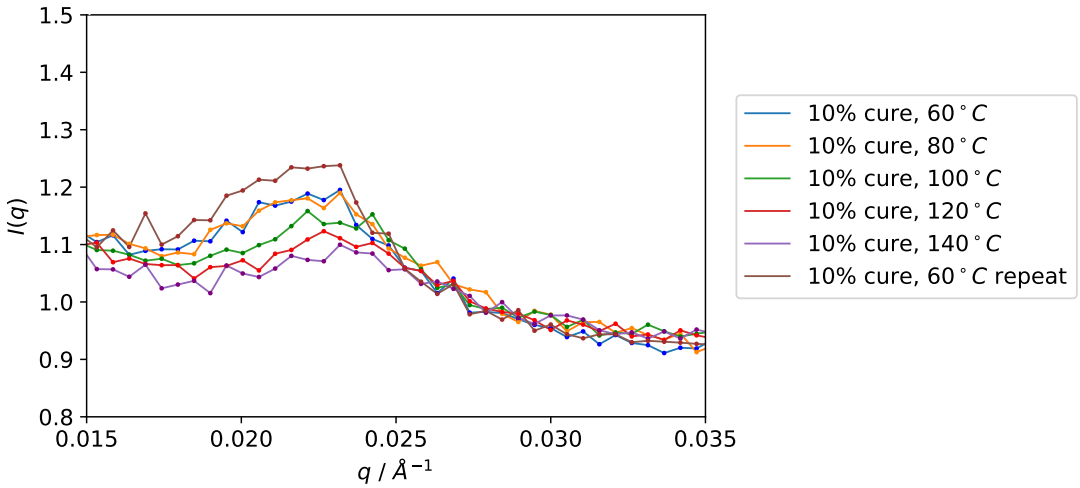

(c) 10 % cure.

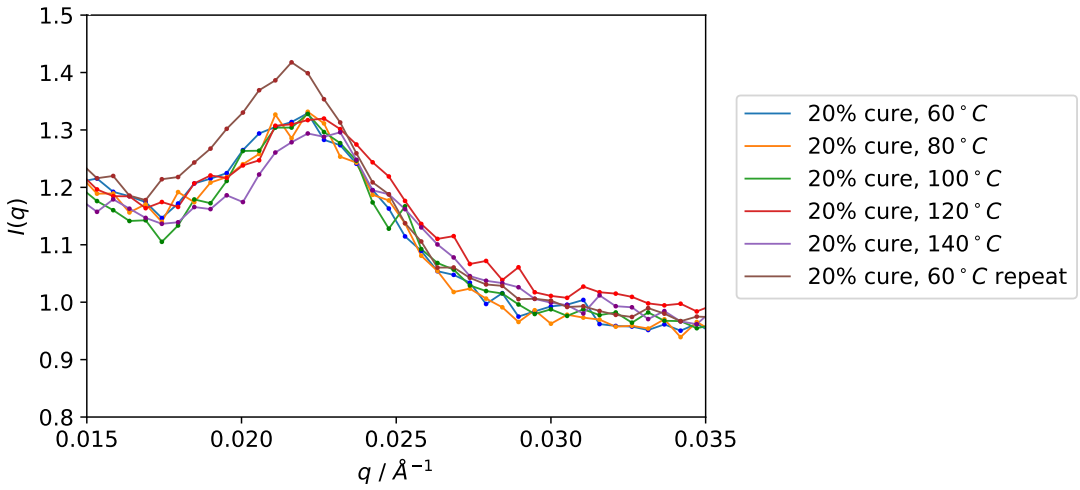

(d) 20 % cure.

Figure 4.19: Plots of $I(q)$ against q for polymer blends with a range of cure extents, focussing on the peak at $0.02\,\text{Å}^{-1}$. Values are given for measurements at a range of increasing temperatures at 20 °C intervals between 60 °C and 140 °C, as well as a repeat measurement at 60 °C after completion of the temperature ramp. Data are given by points, and lines are drawn directly between these without fitting as a guide to the eye.

origin remains unknown. The repeat measurement at 60 °C after the temperature ramp is approximately equivalent to the initial 60 °C measurement, implying that any structural changes are in equilibrium.

The same data, given as comparisons between different cure extents at constant temperature, is shown in Figure 4.20a (at 60 °C) and Figure 4.20b (at 140 °C). In both cases, more inhomogeneity is observed in the more highly cured samples. This is expected from the Flory-Huggins model, which states that the free energy of mixing increases with increasing degree of polymerisation (or equivalently increasing molecular weight). Both graphs in Figure 4.20 are plotted on the same scale, so it is evident that changing the cure extent has a larger impact on the amount of inhomogeneity at higher than lower temperature.

4.4 Conclusions and further work

In this chapter, a model epoxy resin and thermoplastic system has been developed. DGEBA was used as the epoxy, and by limiting the stoichiometric ratio of hexamethylenediamine curative to DGEBA monomer, the extent of cure in the epoxy component could be controlled. Poly(ether sulfone) was then added as the thermoplastic component, in deuterated form where necessary.

The partially cured epoxy component was characterised using rheology, and was found to follow WLF behaviour, implying good miscibility within the material. If an oven was installed onto the rheometer to allow measurements at higher temperatures, similar experiments could be performed after blending thermoplastic with the epoxy samples, to test for concentration fluctuations within the epoxy/thermoplastic blends. Viscosity in the partially cured epoxy material was also observed to increase rapidly with cure extent, implying the presence of larger molecules in the more highly cured material. The molecular weight distribution within the samples, and therefore the sizes of clusters formed by the curing polymerisation reaction, were also determined by gel permeation chromatography.

Storage tests were carried out on samples of partially cure epoxy, with and without added PES. All samples were stable for over two months in $-28\,^{\circ}\mathrm{C}$ freezer, allowing material to be prepared in advance and stored before measurement. However, a significant increase in T_g was observed for the samples stored at room temperature, suggesting that a slow chemical change was taking place, but the cause of this could not be determined.

Small-angle neutron scattering was carried out on the model system with samples at various temperatures and cure extents. The low q behaviour suggests that UCST-like behaviour was taking place in the system, and an intensity peak at approximately $q = 0.02\,\mathrm{\AA}^{-1}$ provides evidence for a molecular organisation

or microphase separation at a lengthscale of 30 nm, also exhibiting UCST-like behaviour. These results were inconsistent with previous studies on DGEBA/PES systems which observed LCST behaviour,[43,127] but these discrepancies are likely to be explained by the much higher thermoplastic molecular weight in the previous studies compared to the current work.

χ interaction parameters could not be determined from these SANS measurements because deviations were observed from the linear trends of Zimm plots at low q, meaning that the intercepts of $1/I(q)$ at zero q could not be evaluated accurately.

Further SANS measurements would allow greater insight to be gained from the model system. Measurements of the same samples could be taken at lower q to identify the cause of the deviations from the expected behaviour and make a better attempt at calculating the χ interaction parameter. The D11 instrument at the Institut Laue-Langevin would allow an order of magnitude reduction in q_{min} from $0.004\,\text{Å}^{-1}$ to $0.0001\,\text{Å}^{-1}$ to carry out these experiments.

The behaviour of the microscale phase separation observed at $0.02\,\text{Å}^{-1}$ (30 nm) could also be further elucidated by running *in situ* SANS measurements. Here, samples of the model system with a stoichiometric ratio of epoxy to curative would be cured in the beamline, so that the development of the peak with cure extent could observed in real time.

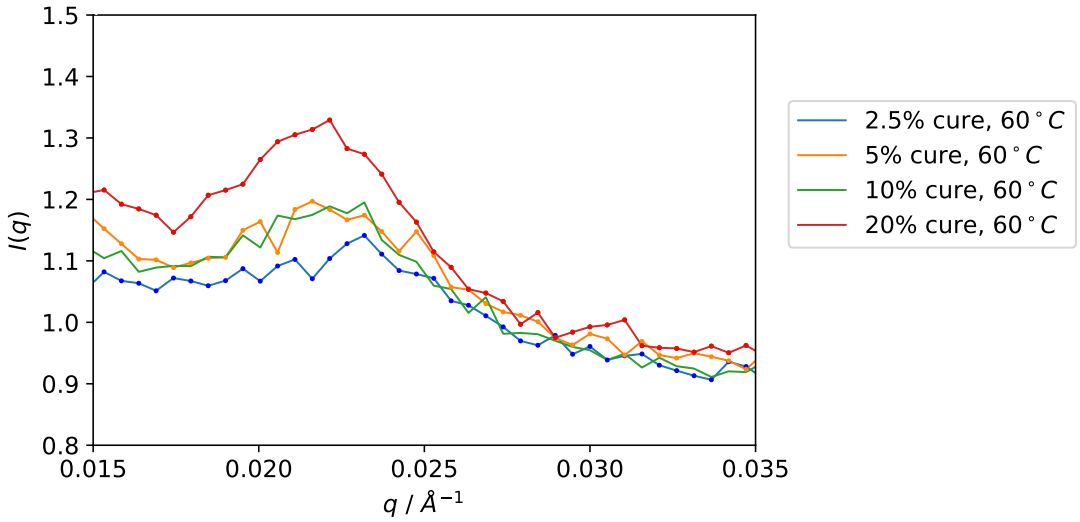

(a) 60 °C

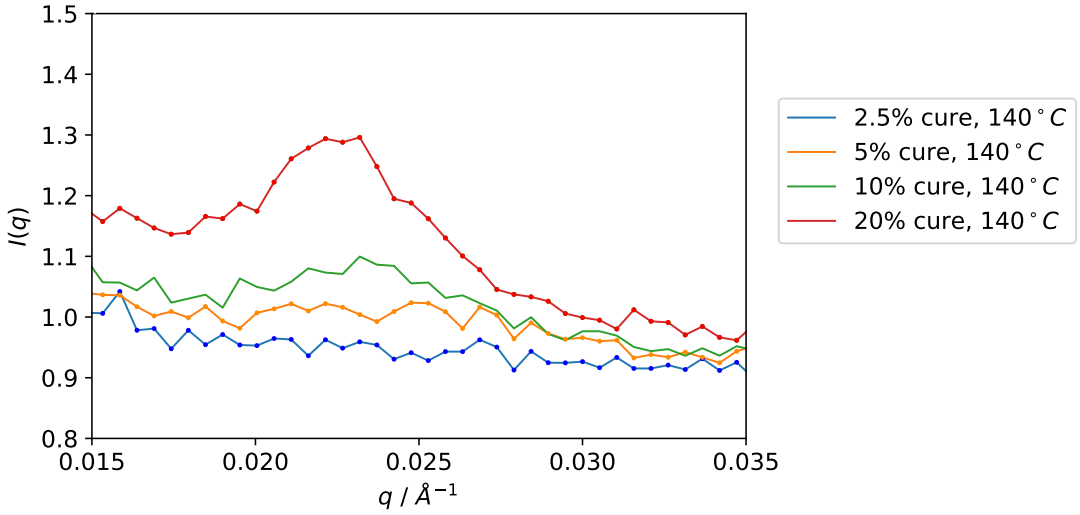

(b) 140 °C

Figure 4.20: Plots of $I(q)$ against q for polymer blends at the same temperature with a range of cure extents, focussing on the peak at 0.02 Å^{-1}. Comparison between samples with different cure extent are shown at temperatures of (a) 60 °C, and (b) 140 °C. Data are given by points, and lines are drawn directly between these without fitting as a guide to the eye.

Chapter 5

Conclusions and further work

This aim of this project was to further understanding of the phase behaviour in blends of branched and linear polymers, which are used extensively in structural aerospace materials.

Much of the phase behaviour of polymer blends is controlled by the free energy of mixing for its components. However, this can only be calculated theoretically for linear polymers or those with simple, regular architectures. In Chapter 2, a computational technique based on the hypothetical scanning simulation method[155,156] was developed to allow the entropy and free energy of randomly branched polymers (like those found in aerospace composites) to be determined. Calculations were carried out for small molecules with a range of architectures and interaction energies on 2D and 3D lattices.

This method allowed the intuitively-expected differences between the entropies and free energies of molecules with different architectures to be quantified, and intricate effects to be determined. This is impossible with more traditional methods such as the Flory-Huggins model, which does not account for any architectures other than linear, and therefore gives inaccurate results that are independent of

polymer shape. It was also shown that in the case of some branched molecules, polymerisation can cause a decrease in entropy. This contradicts the usual logic that more segments possess more degrees of freedom and therefore higher entropy, suggesting that classical models may not predict accurate trends in behaviour.

The model also allowed the local conditions of the polymer segments to be included in much more detail than the Flory-Huggins model, which treats the energy and entropy calculations completely separately according to mean-field assumptions. This meant that the interplay between the two could be highlighted as small deviations from the mean-field linear trend between energetic interactions and free energy. This was particularly evident when the energetic interactions were strong, so that the likely polymer conformations became biased from the random distribution predicted by the mean-field methodology towards those with more favourable energies.

The model currently only considers single polymers in an infinitely dilute solution of implicit solvent, so is not yet able to account for interactions between molecules or calculate free energies of mixing. Aerospace polymers contain a high density of branched material, and as both entropy and energy are expected to be strongly impacted by molecular packing, this is a fairly major shortcoming.

It is hoped that in the future, calculations for free energy could be carried out for multiple branched polymer molecules on the same lattice, as has been done previously for linear ones.[165,166] It is unlikely that the hypothetical scanning method could be used for this, as it relies on dynamic Monte Carlo moves to create a Boltzmann distributed ensemble of systems. An adapted version of the pivot algorithm[161] was used to create the ensemble of single molecules, but this would not work for systems with multiple polymers as it does not allow for effective translation of material across the lattice. No other suitable dynamic Monte Carlo moves[109] exist for branched molecules using the simple cubic lattice model with

one segment per lattice site, because they cannot be adapted to maintain the connectivity of polymer segments with functionalities higher than two.

Therefore a scanning simulation, which calculates entropy and free energy by constructing each polymer segment by segment on the lattice,[165] appears more promising. The problem here is likely to be a high attrition rate for even moderately dense systems. This would reduce computational efficiency such that only low density systems with little interaction between the polymers could be simulated. However, lattices containing a total volume fraction of up to $\phi = 0.63$ were previously studied using linear polymers,[165] and although the attrition rate is expected to be higher for branched polymers, this remains a viable option.

There is also a possibility of using the bond fluctuation model, which allows dynamic Monte Carlo moves of branched polymers, to prepare an ensemble for calculations. This has not been attempted, however, because it allows much more flexibility in the positions of the polymer segments, with 108 different potential bond vectors between neighbouring chain segments, rather than 6 in the simple cubic representation. This would cause a dramatic decrease in the efficiency of computing the probabilities for placing each polymer segment, and extend already long simulation times.

In Chapter 3, a coarse-grained Monte Carlo model based on this bond fluctuation technique was used to directly simulate concentration fluctuations in blends of branched and linear polymers. As concentration fluctuations are the precursor for phase separation, comparing their size allows the relative stabilities of different blends to be estimated. The aim was to develop a computational model that, with appropriate calibration, could be used to gain information about the phase behaviour of industrially-relevant blends with less experimental work.

In the model, thermoplastic polymers, epoxy monomers and curative molecules were placed on a 3D cubic lattice, and a bonding simulation was carried out to

replicate the curing reaction of difunctional epoxy monomers with tetrafunctional diamines. The amount of curative in the system was limited, so that the final epoxy cure was controlled to 5 %, 10 % and 20 %.

This produced a polydisperse distribution of molecular weights, as would occur during an experimental curing reaction. Unfortunately, the molecular weight distributions obtained (characterised by the averages M_n, M_w and M_z) were significantly different to those predicted by the theoretical Stockmayer model.[134] Reasons for this could be insufficient equilibration between each bonding step, and the technical invalidity of Monte Carlo simulations for studying systems undergoing non-equilibrium effects like irreversible bonding reactions, even when all moves are physically possible. In the future, attempts could be made to improve the accuracy of the resulting molecular weights by altering the bonding probabilities and energetic interactions until distributions approximating those of theoretical predictions or experimental results (measured by gel permeation chromatography) are reached.

Nevertheless, the trends in molecular weight were correlated correctly with cure extent, so simulations of concentration fluctuations were carried out for systems with each of the cure extents mentioned above, and a range of different interaction energy combinations and overall densities. Total interactions energies, radii of gyration and radial distribution functions were calculated in each case. These were shown to follow the expected trends, establishing the model's validity for studying concentration fluctuations in blends that exhibit upper critical solution behaviour. Structure factors, although not shown here, were also calculated from the radial distribution functions. These would allow comparison between simulation and experimental results measured by small-angle neutron scattering, if suitable parameters for thermoplastic length, epoxy molecular weight distribution and interaction energies were chosen.

Finally, in Chapter 4, model experimental system was designed for investigating concentration fluctuations in blends similar to those that could be studied using the the computational model designed in Chapter 3. The simulation needs to be run in equilibrium conditions of fixed temperature and low cure extent, so the experimental system should also be able to be measured under these conditions. In addition, this method allows the competing effects of temperature and cure extent on phase behaviour to be isolated and compared. χ interaction parameters can also often be gained from neutron scattering experiments, which would be useful for calibrating the energetic interactions in the simulations, and providing a basis for effective validation of the model.

The chosen experimental system consisted of partially cured DGEBA epoxy resin and poly(ether sulfone) thermoplastic, where the cure extent was controlled to 2.5 %, 5 %, 10 % and 20 % by limiting the amount of hexamethylenediamine curative.

This is a good model system because it cures quickly at low temperatures without unwanted side reactions, and allows for at least 20 wt.% of thermoplastic to be dissolved. Storage tests were carried out, showing all samples to be stable over a period of two months in a $-28\,^{\circ}\mathrm{C}$ freezer, but increases in glass transition temperatures were observed during room temperature storage. This suggests that the samples underwent a slow chemical reaction at room temperature, but the cause of this was not determined. The samples were, however, found to be chemically stable for several hours at raised temperatures of up to $140\,^{\circ}\mathrm{C}$.

The molecular weight distributions within the partially cured epoxy components were measured using gel permeation chromatography, and found to compare favourably to theoretical predictions using the Stockmayer model for gelation,[134], although some deviation was observed. The viscosities of the epoxy components were also measured at a range of temperatures, and observed to increase ex-

ponentially with cure extent, and decrease with temperature. By and large, the epoxy components followed time-temperature superposition behaviour, suggesting good miscibility between the unreacted monomers and reacted clusters. Williams-Landel-Ferry parameters were calculated for each cure extent.

Small-angle neutron scattering (SANS) was carried out on blends of the partially cured epoxy samples with 20 wt.% dissolved deuterated poly(ether sulfone). The four different cure extents mentioned above were tested, each at a range of five temperatures between 60 °C and 140 °C. A final repeat measurement at 60 °C suggested that no non-equilibrium chemical changes took place in the samples during the heating cycle. This procedure allowed the normally convoluted effects of the curing reaction and temperature changes to be isolated.

A decreasing slope in scattering intensity $I(q)$ with wavenumber q was observed at low q values of under $0.02\,\text{Å}^{-1}$ in all samples. The intensity decreased with temperature, which suggested the blends exhibited upper critical solution temperature behaviour, with better miscibility at higher temperatures. An attempt to extract χ interaction parameters for the blends was made by extrapolating Zimm plots to zero q. However, deviation from the expected linear trend was observed at the lowest q values of approximately $0.004\,\text{Å}^{-1}$, so reliable extrapolations could not be obtained, and the intercepts and χ values could not be accurately determined. Another SANS experiment is planned to probe the same systems at q values an order of magnitude lower, in an attempt to determine the cause of these deviations and allow the χ interaction parameters to be calculated.

An intensity peak was also observed at a q value of about $0.02\,\text{Å}^{-1}$, corresponding to a real space lengthscale of roughly 30 nm. It is suspected that this may represent some sort of molecular organisation or microscale phase separation, although the exact cause remains unknown. An attempt to further elucidate this behaviour will hopefully be made by measuring *in situ* curing of the system in

the beamline. This would allow the development of the peak to be observed over the full course of the curing reaction, rather than only at the four discrete points during the early stages of the cure cycle measured here.

Bibliography

[1] J. Matsui. Polymer matrix composites (PMC) in aerospace. *Advanced Composite Materials*, 4(3):197–208, 1995.

[2] C. Soutis. Fibre reinforced composites in aircraft construction. *Progress in Aerospace Sciences*, 41(2):143–151, 2005.

[3] T. Morimoto, S. Kobayashi, Y. Nagao, and Y. Iwahori. A new cost/weight trade-off method for airframe material decisions based on variable fuel price. *Cogent Engineering*, 4(1):1285483, 2017.

[4] N. Shama Roa, T.G.A. Simha, K.P. Rao, and G.V.V. Ravi Kumar. Carbon composites are becoming competitive and cost effective, 2018. URL https://www.infosys.com/engineering-services/white-papers/documents/carbon-composites-cost-effective.pdf. [Online; accessed 6 August 2019].

[5] G. Williams, R. Trask, and I. Bond. A self-healing carbon fibre reinforced polymer for aerospace applications. *Composites Part A: Applied Science and Manufacturing*, 38(6):1525–1532, 2007.

[6] I. Hamerton and L. Mooring. The use of thermosets in aerospace applications. In *Thermosets: Structure Properties and Applications*, pages 189–227. Woodhead Publishing, 2012.

[7] B. Griffiths. Boeing sets pace for composite usage in large civil aircraft. *CompositesWorld*, 2017. URL https://www.compositesworld.com/articles/boeing-sets-pace-for-composite-usage-in-large-civil-aircraft. [Online; accessed 16 August 2019].

[8] F. Tanasa and M. Zanoaga. Fiber-reinforced polymer composites as structural materials for aeronautics. In *Proceedings of the International Conference of Scientific Paper, AFASES*, 2013.

[9] J. Sloan. Boeing offers insight on 787 composites lessons. *CompositesWorld*, 2014. URL https://www.compositesworld.com/blog/post/despite-787-boeing-not-sold-on-composites. [Online; accessed 12 August 2019].

[10] J.M.G. Cowie and V. Arrighi. *Polymers: Chemistry and Physics of Modern Materials, Third Edition*. CRC Press, 2007.

[11] F.W. Billmeyer. *Textbook of Polymer Science, Third Edition*. Wiley, 1984.

[12] W. Bolton. *Engineering Materials 2*. Newnes, 1987.

[13] M.F. Ashby and D.R.H. Jones. *Engineering Materials 1: An Introduction to Properties, Applications and Design, Fourth Edition*. Butterworth-Heinemann, 2012.

[14] D.V. Rosato, D.V. Rosato, and M.V. Rosato. *Plastic Product Material and Process Selection Handbook*. Elsevier, 2004.

[15] Victrex plc. Materials Properties Guide. URL www.victrex.com/~/media/literature/en/material-properties-guide_us-4-20.pdf. [Online; accessed 17 August 2019].

[16] G. Hou. Using Thermoplastic Composites for Aerospace Applications. *Aerospace and Defense Technology*, 2017. URL https://www.aerodefensetech.com/component/content/article/adt/features/articles/27952. [Online; accessed 17 August 2019].

[17] L.H. Baekeland. The Synthesis, Constitution, and Uses of Bakelite. *Journal of Industrial and Engineering Chemistry*, 1(3):149–161, 1909.

[18] A. Kausar. Role of Thermosetting Polymer in Structural Composite. *American Journal of Polymer Science & Engineering*, 5(1):1–12, 2017.

[19] A. Chatterjee. Thermal degradation analysis of thermoset resins. *Journal of Applied Polymer Science*, 114(3):1417–1425, 2009.

[20] R.J. Young and P.A. Lovell. *Introduction to Polymers, Third Edition*. CRC Press, 2011.

[21] S.R. Rosen. *Thermoforming: Improving Process Performance*. Society of Manufacturing Engineers, 2002.

[22] R.A.L. Jones. *Soft Condensed Matter*. Oxford University Press, 2002.

[23] H.S. Kaufman and J.J. Falcetta. *Introduction to Polymer Science and Technology*. Wiley, 1977.

[24] A.Y. Ghasemi, M.and Singapati, M. Tsianou, and P. Alexandridis. Dissolution of semicrystalline polymer fibers: Numerical modeling and parametric analysis. *AIChE Journal*, 63(4):1368–1383, 2017.

[25] D.I. Bower. *An Introduction to Polymer Physics*. Cambridge University Press, 2002.

[26] M.S. Green and A.V. Tobolsky. A New Approach to the Theory of Relaxing Polymeric Media. *The Journal of Chemical Physics*, 14(2):80–92, 1946.

[27] A.S. Lodge. A network theory of flow birefringence and stress in concentrated polymer solutions. *Transactions of the Faraday Society*, 52:120–130, 1956.

[28] M. Doi and S.F. Edwards. *The Theory of Polymer Dynamics*. Oxford University Press, 1986.

[29] P.-G. De Gennes. *Scaling Concepts in Polymer Physics*. Cornell University Press, 1979.

[30] F Bueche. Viscosity, Self-Diffusion, and Allied Effects in Solid Polymers. *The Journal of Chemical Physics*, 20(12):1959–1964, 1952.

[31] J.N. Spencer, G.M. Bodner, and L.H. Rickard. *Chemistry: Structure and Dynamics, Fifth Edition*. John Wiley & Sons Inc., 2012.

[32] J. Happian-Smith. *An Introduction to Modern Vehicle Design*. Butterworth-Heinemann, 2001.

[33] S.K. De and J.R. White. *Rubber Technologist's Handbook*. Rapra Technology Limited, 2001.

[34] M. Doi. *Introduction to Polymer Physics*. Oxford University Press, 1996.

[35] R.J. Spontak and N.P. Patel. Thermoplastic elastomers: fundamentals and applications. *Current Opinion in Colloid & Interface Science*, 5(5-6):333–340, 2000.

[36] E. Wittenberg, A. Meyer, S. Eggers, and V. Abetz. Hydrogen bonding and thermoplastic elastomers–a nice couple with temperature-adjustable mechanical properties. *Soft Matter*, 14:2701–2711, 2018.

[37] L.K. Massey. *The Effect of UV Light and Weather on Plastics and Elastomers, Second Edition*. William Andrew, Inc., 2007.

[38] J. Hicks. *Welded Joint Design, Third Edition*. Abington Publishing, 1999.

[39] H. Morris. Why is it so cold on a plane? *The Telegraph*, 2017. URL https://www.telegraph.co.uk/travel/travel-truths/why-are-planes-so-cold/. [Online; accessed 10 July 2019].

[40] X.-K. Zhu and J.A. Joyce. Review of fracture toughness (G, K, J, CTOD, CTOA) testing and standardization. *Engineering Fracture Mechanics*, 85: 1–46, 2012.

[41] K.-C. Teng and F.-C. Chang. Single-phase and multiple-phase thermoplastic/thermoset polyblends: 2. Morphologies and mechanical properties of phenoxy/epoxy blends. *Polymer*, 37(12):2385–2394, 1996.

[42] C.B. Bucknall and A.H. Gilbert. Toughening tetrafunctional epoxy resins using polyetherimide. *Polymer*, 30(2):213–217, 1989.

[43] C.B. Bucknall and I.K. Partridge. Phase separation in epoxy resins containing polyethersulphone. *Polymer*, 24(5):639–644, 1983.

[44] L.B. Bourne, F.J.M. Milner, and K.B. Alberman. Health Problems of Epoxy Resins and Amine-curing Agents. *British Journal of Industrial Medicine*, 16(2):81–97, 1959.

[45] F.C. Campbell. *Manufacturing Processes for Advanced Composites*. Elsevier, 2004.

[46] S.R. White and H.T. Hahn. Cure Cycle Optimization for the Reduction of Processing-Induced Residual Stresses in Composite Materials. *Journal of Composite Materials*, 27(14):1352–1378, 1993.

[47] Y.-T. Tsai, S.-Y. Lin, J.-W. Tong, W.-C. Chen, W.-T. Chen, and C-M Shu. Incompatible hazard investigation of a cycloaliphatic epoxy resin using green analytical method. *Journal of Thermal Analysis and Calorimetry*, 122 (3):1135–1141, 2015.

[48] J. Hodges, B. Yates, M.I. Darby, G.H. Wostenholm, J.F. Clemmet, and T.F. Keates. Residual stresses and the optimum cure cycle for an epoxy resin. *Journal of Materials Science*, 24(6):1984–1990, 1989.

[49] H. Ishida and T. Agag. *Handbook of Benzoxazine Resins*. Elsevier, 2011.

[50] A.P. Mouritz. *Introduction to aerospace materials*. Woodhead Publishing, 2012.

[51] Solvay. Advanced composite materials for aerospace. URL https://www.solvay.com/sites/g/files/srpend221/files/2018-07/Composite%20-%20Aerospace%20Brochure.pdf. [Online; accessed 18 August 2019].

[52] G. Fischer. *High temperature and toughened bismaleimide composite materials for aeronautics*. PhD thesis, Université de Lyon, 2015.

[53] X. Wang and J.K. Gillham. Competitive primary amine/epoxy and secondary amine/epoxy reactions: Effect on the isothermal time-to-vitrify. *Journal of Applied Polymer Science*, 43(12):2267–2277, 1991.

[54] S.J. Tucker. *Study of 3,3' vs. 4,4' DDS Isomer Curatives on Physical Properties and Phenyl Ring Motions of DGEBA Epoxy via Molecular Dynamics, Deuterium NMR, and Dielectric Spectroscopy*. PhD thesis, University of Southern Mississippi, 2010.

[55] G. Ognibene, S. Mannino, M.E. Fragalà, and G. Cicala. Trifunctional Epoxy Resin Composites Modified by Soluble Electrospun Veils: Effect on the Viscoelastic and Morphological Properties. *Materials*, 11(3):405, 2018.

[56] S. Bondzic, J. Hodgkin, J. Krstina, and J. Mardel. Chemistry of thermal ageing in aerospace epoxy composites. *Journal of Applied Polymer Science*, 100(3):2210–2219, 2006.

[57] L. Xu and J.R. Schlup. Etherification versus amine addition during epoxy resin/amine cure: An *in situ* study using near-infrared spectroscopy. *Journal of Applied Polymer Science*, 67(5):895–901, 1998.

[58] I. Blanco, G. Cicala, O. Motta, and A. Recca. Influence of a selected hardener on the phase separation in epoxy/thermoplastic polymer blends. *Journal of Applied Polymer Science*, 94(1):361–371, 2004.

[59] A.C. Grillet, J. Galy, J.P. Pascault, and I. Bardin. Effects of the structure of the aromatic curing agent on the cure kinetics of epoxy networks. *Polymer*, 30(11):2094–2103, 1989.

[60] O. Hara. Curing agents for epoxy resin. *Three Bond Technical News*, 32 (20):1–10, 1990.

[61] P. Boisse. *Advances in Composites Manufacturing and Process Design*. Woodhead Publishing, 2015.

[62] Conversations with the Solvay team at the Wilton Centre, UK. Personal communication.

[63] B.A. Howell and Y.G. Daniel. The impact of sulfur oxidation level on flame retardancy. *Journal of Fire Sciences*, 36(6):518–534, 2018.

[64] I. Blanco, L. Oliveri, G. Cicala, and A. Recca. Effects of novel reactive toughening agent on thermal stability of epoxy resin. *Journal of Thermal Analysis and Calorimetry*, 108(2):685–693, 2012.

[65] V.S. Sastri. *Plastics in Medical Devices: Properties, Requirements, and Applications, Second Edition*. William Andrew, 2014.

[66] J.H. Hodgkin, G.P. Simon, and R.J. Varley. Thermoplastic toughening of epoxy resins: a critical review. *Polymers for Advanced Technologies*, 9(1): 3–10, 1998.

[67] A.R. Offringa. Thermoplastic composites–rapid processing applications. *Composites Part A: Applied Science and Manufacturing*, 27(4):329–336, 1996.

[68] I.M. Klotz and R.M. Rosenberg. *Chemical Thermodynamics: Basic Concepts and Methods, Seventh Edition*. Wiley, 2010.

[69] R.K. Pathria. *Statistical Mechanics, Second Edition*. Butterworth-Heinemann, 1996.

[70] D. Chandler. *Introduction to Modern Statistical Mechanics*. Oxford University Press, 1987.

[71] P.J. Flory. *Principles of Polymer Chemistry*. Cornell University Press, 1953.

[72] J.H. Hildebrand. The Term 'Regular Solution'. *Nature*, 168:868, 1951.

[73] F. Schmid. Theory and Simulation of Multiphase Polymer Systems. In *Handbook of Multiphase Polymer Systems*, pages 31–80. Wiley, 2011.

[74] M Müller and K Binder. Computer Simulation of Asymmetric Polymer Mixtures. *Macromolecules*, 28(6):1825–1834, 1995.

[75] M. Rubinstein, R.H. Colby, et al. *Polymer Physics*. Oxford University Press, 2003.

[76] W.J.C. Orr. The free energies of solutions of single and multiple molecules. *Transactions of the Faraday Society*, 40:320–332, 1944.

[77] E.A. Guggenheim. Statistical thermodynamics of mixtures with non-zero energies of mixing. *Proceedings of the Royal Society A: Mathematical, Physical and Engineering Sciences*, 183(993):213–227, 1944.

[78] P.J. Flory, R.A. Orwoll, and A. Vrij. Statistical Thermodynamics of Chain Molecule Liquids. I. An Equation of State for Normal Paraffin Hydrocarbons. *Journal of the American Chemical Society*, 86(17):3507–3514, 1964.

[79] P.J. Flory, R.A. Orwoll, and A. Vrij. Statistical Thermodynamics of Chain Molecule Liquids. II. Liquid Mixtures of Normal Paraffin Hydrocarbons. *Journal of the American Chemical Society*, 86(17):3515–3520, 1964.

[80] P.J. Flory. Statistical Thermodynamics of Liquid Mixtures. *Journal of the American Chemical Society*, 87(9):1833–1838, 1965.

[81] D. Patterson. Free Volume and Polymer Solubility. A Qualitative View. *Macromolecules*, 2(6):672–677, 1969.

[82] D. Patterson and G. Delmas. Corresponding states theories and liquid models. *Discussions of the Faraday Society*, 49:98–105, 1970.

[83] I. Prigogine. Molecular Theory of Solutions. 1957.

[84] I.C. Sanchez and R.H. Lacombe. Theory of liquid–liquid and liquid–vapour equilibria. *Nature*, 252(5482):381–383, 1974.

[85] I.C. Sanchez and R.H. Lacombe. An elementary molecular theory of classical fluids. Pure fluids. *The Journal of Physical Chemistry*, 80(21):2352–2362, 1976.

[86] R.H. Lacombe and I.C. Sanchez. Statistical thermodynamics of fluid mixtures. *The Journal of Physical Chemistry*, 80(23):2568–2580, 1976.

[87] I.C. Sanchez. Statistical Thermodynamics of Polymer Blends. In *Polymer Blends*, pages 115–140. Academic Press, 2012.

[88] S. Coveney. *Fundamentals of Phase Separation in Polymer Blend Thin Films*. Springer, 2015.

[89] B.A. Miller-Chou and J.L. Koenig. A review of polymer dissolution. *Progress in Polymer Science*, 28(8):1223–1270, 2003.

[90] J.H. Hildebrand and R.L. Scott. *The Solubility of Nonelectrolytes, Third Edition*. 1964.

[91] A. Martin and J. Carstensen. Extended Solubility Approach: Solubility Parameters for Crystalline Solid Compounds. *Journal of Pharmaceutical Sciences*, 70(2):170–172, 1981.

[92] L. Robeson. Historical Perspective of Advances in the Science and Technology of Polymer Blends. *Polymers*, 6(5):1251–1265, 2014.

[93] R.P. White, J.E.G. Lipson, and J.S. Higgins. New Correlations in Polymer Blend Miscibility. *Macromolecules*, 45(2):1076–1084, 2012.

[94] E.B. Smith. *Basic Physical Chemistry: The Route to Understanding, Revised Edition*. Imperial College Press, 2013.

[95] C.M. Hansen. *The Three Dimensional Solubility Parameter and Solvent Diffusion Coefficient*, volume 14. 1967.

[96] P.C. Painter, J.F. Graf, and M.M. Coleman. Effect of hydrogen bonding on the enthalpy of mixing and the composition dependence of the glass transition temperature in polymer blends. *Macromolecules*, 24(20):5630–5638, 1991.

[97] M.M. Coleman, J.F. Graf, and P.C. Painter. *Specific Interactions and the Miscibility of Polymer Blends*. Technomic Publishing Company Inc., 1991.

[98] L.H. Sperling. *Introduction to Physical Polymer Science, Fourth Edition*. Wiley-Interscience, 2005.

[99] M.G. Bawendi and K.F. Freed. A lattice model for self-and mutually avoiding semiflexible polymer chains. *The Journal of Chemical Physics*, 86(6): 3720–3730, 1987.

[100] M.G. Bawendi and K.F. Freed. Systematic corrections to Flory–Huggins (t)heory: Polymer–solvent–void systems and binary blend–void systems. *The Journal of Chemical Physics*, 88(4):2741–2756, 1988.

[101] A.M. Nemirovsky and M.D. Coutinho-Filho. From dilute to dense self-avoiding walks on hypercubic lattices. *Journal of Statistical Physics*, 53 (5-6):1139–1153, 1988.

[102] A.M. Nemirovsky and M.D. Coutinho-Filho. Packing flexible polymer chains on a lattice. *Physical Review A*, 39(6):3120, 1989.

[103] S.F. Edwards. The statistical mechanics of polymers with excluded volume. *Proceedings of the Physical Society*, 85(4):613–624, 1965.

[104] J. van Male. *Self-consistent-field theory for chain molecules: extensions, computational aspects, and applications*. 2003.

[105] K.F. Freed and J. Dudowicz. Lattice cluster theory for pedestrians: The incompressible limit and the miscibility of polyolefin blends. *Macromolecules*, 31(19):6681–6690, 1998.

[106] J. Dudowicz, K.F. Freed, and J.F Douglas. New patterns of polymer blend miscibility associated with monomer shape and size asymmetry. *The Journal of Chemical Physics*, 116(22):9983–9996, 2002.

[107] M.P. Allen and D.J. Tildesley. *Computer Simulation of Liquids*. Oxford University Press, 2017.

[108] D. Frenkel and B. Smit. *Understanding Molecular Simulation: From Algorithms to Applications*.

[109] A.D. Sokal. Monte Carlo Methods for the Self-Avoiding Walk. In *Monte Carlo and Molecular Dynamics Simulations in Polymer Science*, pages 47–124. Wiley, 1995.

[110] K. Binder and A. Milchev. Off-lattice Monte Carlo methods for coarse-grained models of polymeric materials and selected applications. *Journal of Computer-Aided Materials Design*, 9(1):33–74, 2002.

[111] P. Español and P.B. Warren. Perspective: Dissipative particle dynamics. *The Journal of Chemical Physics*, 146(15):150901, 2017.

[112] R.D. Groot and T.J. Madden. Dynamic simulation of diblock copolymer microphase separation. *The Journal of Chemical Physics*, 108(20):8713–8724, 1998.

[113] K.E. Novik and P.V. Coveney. Spinodal decomposition of off-critical quenches with a viscous phase using dissipative particle dynamics in two and three spatial dimensions. *Physical Review E*, 61(1):435–448, 2000.

[114] M. Laradji and M.J.A¿ Hore. Nanospheres in phase-separating multicomponent fluids: A three-dimensional dissipative particle dynamics simulation. *The Journal of chemical physics*, 121(21):10641–10647, 2004.

[115] A Sariban and K Binder. Phase Separation of Polymer Mixtures in the Presence of Solvent. *Macromolecules*, 21(3):711–726, 1988.

[116] A. Sariban and K. Binder. Monte carlo simulation of a lattice model for ternary polymer mixtures. *Colloid and Polymer Science*, 266(5):389–397, 1988.

[117] K. Binder. Simulations of phase transitions in macromolecular systems. *Computer Physics Communications*, 147(1-2):22–33, 2002.

[118] G.A. Mannella, V. La Carrubba, and V. Brucato. Measurement of cloud point temperature in polymer solutions. *Review of Scientific Instruments*, 84(7):075118, 2013.

[119] M. Tambasco, J.E.G. Lipson, and J.S. Higgins. Blend Miscibility and the Flory- Huggins Interaction Parameter: A Critical Examination. *Macromolecules*, 39(14):4860–4868, 2006.

[120] P.W. Atkins, J. de Paula, and J. Keeler. *Atkins' Physical Chemistry, Eleventh Edition*. Oxford University Press, 2018.

[121] I.C. Sanchez and MT Stone. Statistical Thermodynamics of Polymer Solutions and Blends. In *Polymer Blends: Formulation*, pages 15–53. 2000.

[122] L.M. Robeson. *Polymer Blends: A Comprehensive Review*. Hanser, 2007.

[123] J. Dudowicz, K.F. Freed, and J.F. Douglas. Concentration fluctuations in miscible polymer blends: Influence of temperature and chain rigidity. *The Journal of Chemical Physics*, 140(19):194901, 2014.

[124] V.I. Kalikmanov. Classical nucleation theory. In *Nucleation Theory*, pages 17–41. Springer, 2013.

[125] C.S. Kiang, D. Stauffer, G.H. Walker, O.P. Puri, J.D.Jr. Wise, and E.M. Patterson. A Reexamination of Homogeneous Nucleation Theory. *Journal of the Atmospheric Sciences*, 28(7):1222–1232, 1971.

[126] D. Lee, J.-Y. Huh, D. Jeong, J. Shin, A. Yun, and J. Kim. Physical, mathematical, and numerical derivations of the Cahn–Hilliard equation. *Computational Materials Science*, 81:216–225, 2014.

[127] K. Yamanaka and T. Inoue. Structure development in epoxy resin modified with poly (ether sulphone). *Polymer*, 30(4):662–667, 1989.

[128] P. Sollich. Predicting phase equilibria in polydisperse systems. *Journal of Physics: Condensed Matter*, 14(3):R79–R117, 2001.

[129] K.-C. Teng and F.-C. Chang. Single-phase and multiple-phase thermoplastic/thermoset polyblends: 1. Kinetics and mechanisms of phenoxy/epoxy blends. *Polymer*, 34(20):4291–4299, 1993.

[130] T.D. Ignatova, L.F. Kosyanchuk, T.T. Todosiychuk, and A.E. Nesterov. Reaction-Induced Phase Separation and Structure Formation in Polymer Blends. *Composite Interfaces*, 18(3):185–236, 2011.

[131] D. Stauffer, A. Coniglio, and M. Adam. Gelation and critical phenomena. In *Polymer Networks*, pages 103–158. Springer, 1982.

[132] S. Mortimer, A.J. Ryan, and J.L. Stanford. Rheological Behavior and Gel-Point Determination for a Model Lewis Acid-Initiated Chain Growth Epoxy Resin. *Macromolecules*, 34(9):2973–2980, 2001.

[133] P.J. Flory. Molecular Size Distribution in Three Dimensional Polymers. I. Gelation. *Journal of the American Chemical Society*, 63(11):3083–3090, 1941.

[134] W.H. Stockmayer. Theory of Molecular Size Distribution and Gel Formation in Branched-Chain Polymers. *The Journal of Chemical Physics*, 11(2): 45–55, 1943.

[135] W.H. Stockmayer. Theory of Molecular Size Distribution and Gel Formation in Branched Polymers. II. General Cross Linking. *The Journal of Chemical Physics*, 12(4):125–131, 1944.

[136] Y. Ishii, A.J. Ryan, and N. Clarke. Phase diagram prediction for a blend of Poly(2,6-dimethyl-1,4-phenylene ether)(ppe)/epoxy resin during reaction induced phase separation. *Polymer*, 44(13):3641–3647, 2003.

[137] J.W. Essam. Percolation theory. *Reports on Progress in Physics*, 43(7): 833–912, 1980.

[138] N. Clarke, T.C.B. McLeish, and S.D. Jenkins. Phase Behavior of Linear/Branched Polymer Blends. *Macromolecules*, 28(13):4650–4659, 1995.

[139] R. Koningsveld and A.J. Staverman. Liquid–liquid phase separation in multicomponent polymer solutions. II. The critical state. *Journal of Polymer Science Part A-2: Polymer Physics*, 6(2):325–347, 1968.

[140] K. Šolc. Cloud-Point Curves of Polymers with Logarithmic-Normal Distribution of Molecular Weight. *Macromolecules*, 8(6):819–827, 1975.

[141] K. Binder and H.L. Frisch. Phase stability of weakly crosslinked interpenetrating polymer networks. *The Journal of Chemical Physics*, 81(4): 2126–2136, 1984.

[142] I.C. Henderson and N. Clarke. Reaction-induced phase separation of pseudo-interpenetrating polymer networks in polydisperse polymer blends: A simulation study. *The Journal of Chemical Physics*, 123(14):144903, 2005.

[143] W. Brostow, R. Chiu, I.M. Kalogeras, and A. Vassilikou-Dova. Prediction of glass transition temperatures: Binary blends and copolymers. *Materials Letters*, 62(17-18):3152–3155, 2008.

[144] T.G. Fox. Influence of Diluent and of Copolymer Composition on the Glass Temperature of a Polymer System. *Bulletin of the American Physical Society*, 1:123, 1952.

[145] M. Gordon and J.S. Taylor. Ideal copolymers and the second-order transitions of synthetic rubbers. I. Non-crystalline copolymers. *Journal of Applied Chemistry*, 2(9):493–500, 1952.

[146] T.K. Kwei. The Effect of Hydrogen Bonding on the Glass Transition Temperatures of Polymer Mixtures. *Journal of Polymer Science: Polymer Letters Edition*, 22(6):307–313, 1984.

[147] M.E.J. Newman and G.T. Barkema. *Monte Carlo Methods in Statistical Physics*. Oxford University Press, 1999.

[148] M. Müller and W. Paul. Measuring the chemical potential of polymer solutions and melts in computer simulations. *The Journal of Chemical Physics*, 100(1):719–724, 1994.

[149] R.P. White and H. Meirovitch. Calculation of the entropy of random coil polymers with the hypothetical scanning Monte Carlo method. *The Journal of Chemical Physics*, 123(21):214908, 2005.

[150] B. Widom. Some Topics in the Theory of Fluids. *The Journal of Chemical Physics*, 39(11):2808–2812, 1963.

[151] K.G. Honnell and R. Hall, C.K .and Dickman. On the pressure equation for chain molecules. *The Journal of Chemical Physics*, 87(1):664–674, 1987.

[152] R. Dickman and C.K Hall. High density Monte Carlo simulations of chain molecules: Bulk equation of state and density profile near walls. *The Journal of Chemical Physics*, 89(5):3168–3174, 1988.

[153] K.G. Honnell and C.K. Hall. A new equation of state for athermal chains. *The Journal of Chemical Physics*, 90(3):1841–1855, 1989.

[154] S.K. Kumar, I. Szleifer, and A.Z. Panagiotopoulos. Determination of the Chemical Potentials of Polymeric Systems from Monte Carlo Simulations. *Physical Review Letters*, 66(22):2935–2938, 1991.

[155] H. Meirovitch. Scanning method as an unbiased simulation technique and its application to the study of self-attracting random walks. *Physical Review A*, 32(6):3699–3708, 1985.

[156] H. Meirovitch. Computer simulation of the free energy of polymer chains with excluded volume and with finite interactions. *Physical Review A*, 32 (6):3709–3715, 1985.

[157] H. Meirovitch, D.H. Kitson, and A.T. Hagler. Computer Simulation of the Entropy of Polypeptides Using the Local States Method: Application to Cyclo-(Ala-Pro-D-Phe)$_2$ in Vacuum and in the Crystal. *Journal of the American Chemical Society*, 114(13):5386–5399, 1992.

[158] H. Meirovitch. Improved Computer Simulation Method for Estimating the Entropy of Macromolecules with Hard-Core Potential. *Macromolecules*, 16 (10):1628–1631, 1983.

[159] R.P. White and H. Meirovitch. Lower and upper bounds for the absolute free energy by the hypothetical scanning Monte Carlo method: Application to liquid argon and water. *The Journal of Chemical Physics*, 121(22):10889–10904, 2004.

[160] H. Meirovitch and H.A. Scheraga. Computer simulation of the entropy of continuum chain models: The two-dimensional freely jointed chain of hard disks. *The Journal of Chemical Physics*, 84(11):6369–6375, 1986.

[161] N. Madras and A.D. Sokal. The pivot algorithm: A highly efficient Monte Carlo method for the self-avoiding walk. *Journal of Statistical Physics*, 50 (1-2):109–186, 1988.

[162] A.R. Conway, I.G. Enting, and A.J. Guttmann. Algebraic techniques for enumerating self-avoiding walks on the square lattice. *Journal of Physics A: Mathematical and General*, 26(7):1519–1534, 1993.

[163] N. Clisby, R. Liang, and G. Slade. Self-avoiding walk enumeration via the lace expansion. *Journal of Physics A: Mathematical and Theoretical*, 40 (36):10973–11017, 2007.

[164] A.F.M. Barton. *CRC Handbook of Solubility Parameters and Other Cohesion Parameters, Second Edition*. CRC Press, 1991.

[165] H. Meirovitch. Entropy, pressure, and chemical potential of multiple chain systems from computer simulation. I. Application of the scanning method. *The Journal of Chemical Physics*, 97(8):5803–5815, 1992.

[166] H. Meirovitch. Entropy, pressure, and chemical potential of multiple chain systems from computer simulation. II. Application of the metropolis and the hypothetical scanning methods. *The Journal of Chemical Physics*, 97 (8):5816–5823, 1992.

[167] T. Pakula. Cooperative Relaxations in Condensed Macromolecular Systems. 1. A Model for Computer Simulation. *Macromolecules*, 20(3):679–682, 1987.

[168] T. Pakula and S. Geyler. Cooperative Relaxations in Condensed Macromolecular Systems. 2. computer Simulation of Self-Diffusion of Linear Chains. *Macromolecules*, 20(11):2909–2914, 1987.

[169] M.L. Mansfield. Monte carlo studies of polymer chain dimensions in the melt. *The Journal of Chemical Physics*, 77(3):1554–1559, 1982.

[170] J. Reiter. Monte Carlo Simulations of Linear and Cyclic Chains on Cubic and Quadratic Lattices. *Macromolecules*, 23(16):3811–3816, 1990.

[171] I. Carmesin and K. Kremer. The bond fluctuation method: a new effective algorithm for the dynamics of polymers in all spatial dimensions. *Macromolecules*, 21(9):2819–2823, 1988.

[172] J. Molina-Mateo, J.M. Meseguer-Dueñas, and J.L. Gómez-Ribelles. On the role of inter-and intra-molecular potentials in the simulation of vitrification with the bond fluctuation model. *Polymer*, 46(18):7463–7472, 2005.

[173] J.J. Freire. Influence of chain topology and bond potential on the glass transition of polymer chains simulated with the bond fluctuation model. *Journal of Physics: Condensed Matter*, 20(28):285102, 2008.

[174] J. Baschnagel and K. Binder. Structural aspects of a three-dimensional lattice model for the glass transition of polymer melts: a monte carlo simulation. *Physica A: Statistical Mechanics and its Applications*, 204(1-4): 47–75, 1994.

[175] R. Malik, C.K. Hall, and J. Genzer. Effect of Protein-like Copolymers Composition on the Phase Separation Dynamics of a Polymer Blend: A Monte Carlo Simulation. *Macromolecules*, 46(10):4207–4214, 2013.

[176] J.S. Shaffer. Effects of chain topology on polymer dynamics: Bulk melts. *The Journal of Chemical Physics*, 101(5):4205–4213, 1994.

[177] X. He, J. Nagel, D. Lehmann, and G. Heinrich. Interface Structure between Immiscible Reactive Polymers under Transreaction: a Monte Carlo Simulation. *Macromolecular Theory and Simulations*, 14(5):305–311, 2005.

[178] H.P. Wittmann and K. Kremer. Vectorized version of the bond fluctuation method for lattice polymers. *Computer Physics Communications*, 61(3): 309–330, 1990.

[179] J.K. Johnson, A.Z. Panagiotopoulos, and K.E. Gubbins. Reactive canonical Monte Carlo: A new simulation technique for reacting or associating fluids. *Molecular Physics*, 81(3):717–733, 1994.

[180] M. Fixman. Radius of Gyration of Polymer Chains. *The Journal of Chemical Physics*, 36(2):306–310, 1962.

[181] L. Bai and D. Breen. Calculating Center of Mass in an Unbounded 2D Environment. *Journal of Graphics Tools*, 13(4):53–60, 2008.

[182] A. Filipponi. The radial distribution function probed by x-ray absorption spectroscopy. *Journal of Physics: Condensed Matter*, 6(41):8415–8427, 1994.

[183] K. Zhang. On the Concept of Static Structure Factor. *arXiv:1606.03610*, 2016.

[184] J.S. Higgins and H.C. Benoît. *Polymers and Neutron Scattering*. Oxford University Press, 1994.

[185] L. Cipelletti and D.J. Trappe, V. Pine. Scattering Techniques. In *Fluids, Colloids and Soft Materials: An Introduction to Soft Matter Physics*, pages 131–148. Wiley, 2016.

[186] B. Hammouda. A tutorial on small-angle neutron scattering from polymers. *National Institute of Standards and Technology*, 1995.

[187] T.P. Russell. *Scattering studies from polymer blends*. PhD thesis, University of Massachusetts Amherst, 1978.

[188] J. Liu and M. Ueda. High refractive index polymers: fundamental research and practical applications. *Journal of Materials Chemistry*, 19(47):8907–8919, 2009.

[189] Sigma Aldrich. Hexamethylenediamine Safety Data Sheet. URL https://www.sigmaaldrich.com/catalog/product/aldrich/h11696?lang=en&region=GB&gclid=EAIaIQobChMIyrHTmI_f5AIVxrTtCh0gGw16EAAYASAAEgKL2vD_BwE. [Online; accessed 10 September 2019].

[190] T. Kagiya, M. Izu, T. Matsuda, and K. Fukui. Synthesis of Polyamides by the Polyaddition of Bissuccinimides with Diamines. *Journal of Polymer Science Part A-1: Polymer Chemistry*, 5(1):15–20, 1967.

[191] P. Gabbott. A Practical Introduction to Differential Scanning Calorimetry. In *Principles and Applications of Thermal Analysis*, pages 1–50. Wiley, 2008.

[192] G. Allen and J.C. Bevington. *Comprehensive Polymer Science: The Synthesis, Characterization, Reactions & Applications of Polymers*. Pergamon, 1996.

[193] M.L. Williams, R.F. Landel, and J.D. Ferry. The Temperature Dependence of Relaxation Mechanisms in Amorphous Polymers and Other Glass-Forming Liquids. *Journal of the American Chemical society*, 77(14):3701–3707, 1955.

[194] J.D. Ferry. *Viscoelastic Properties of Polymers, Third Edition.* John Wiley & Sons, 1980.